6-9-2016

Sub-nanosecond UV filaments and their applications for remote spectroscopy and high-voltage discharges

Chengyong Feng

Chengyong Feng

Candidate

Physics and Astronomy

Department

This dissertation is approved, and it is acceptable in quality and form for publication:

Approved by the Dissertation Committee:

Jean-Claude Diels , Chairperson

Ladan Arissian

Sanjay Krishna

Matthias Lenzner

Sub-nanosecond UV filaments and their applications for remote spectroscopy and high-voltage discharges

by

Chengyong Feng

B.S., Optics, Beijing Jiaotong University, 2006
M.S., Optical Sci. and Engineering, University of New Mexico, 2011

DISSERTATION

Submitted in Partial Fulfillment of the
Requirements for the Degree of

Doctor of Philosophy
Optical Science and Engineering

The University of New Mexico

Albuquerque, New Mexico

May, 2016

Dedication

To my family

Acknowledgments

Tremendous help and support from many people have been received during this dissertation work. First of all, I am very grateful to my advisor Prof. Jean-Claude Diels for his guidance, encouragement and support throughout the journey. The impact that I have received from his wisdom and enthusiasm to science, as well as the open-minded way that he has supervised me are greatly appreciated. I am very thankful to other committee members Prof. Ladan Arissian, Prof. Sanjay Krishna and Dr. Matthias Lenzner for guiding me through this process.

I would like to thank the colleagues in Diels research group for their support. I want to emphasize the help from Brian Kamer and Ali Rastegari on different experiments. I am especially grateful to Dr. Xiaozhen Xu, who has introduced me to this group and shared her full knowledge on the UV filament project with me. This dissertation work could not have gone so smoothly without her fundamental works on the high-power UV source.

I am very fortunate to receive a one-year fellowship from ATTOFEL (a Marie-Curie Initial Training Network funded by the 7^{th} Framework Programme of the European Union), which has supported me doing research in Politecnico di Milano during the year of 2012. I have had very good time learning from Prof. Giuseppe Sansone, Prof. Mauro Nisoli and Dr. Francesca Calegari, as well as working with Maurizio Reduzzi. I greatly appreciate their warm hospitality.

I also want to express my gratitude to many friends. Special thanks go to Jim and Priscilla Duncan for their continuous support to my family since the beginning of my PhD life.

Finally, I would like to thank my parents and parents-in-law for believing in me and providing me mental support. Most of all, I am deeply grateful to my wife Gaoxia for her love and support. This journey becomes much more meaningful and joyful with the accompany of her and our two sons Kaixi and Lanmo, who also deserve my special thanks.

Sub-nanosecond UV filaments and their applications for remote spectroscopy and high-voltage discharges

by

Chengyong Feng

B.S., Optics, Beijing Jiaotong University, 2006
M.S., Optical Sci. and Engineering, University of New Mexico, 2011
Ph.D., Optical Science and Engineering, University of New Mexico, 2016

Abstract

Intensive investigations during the past two decades have focused on potential applications of near-infrared (NIR) femtosecond filament for remote spectroscopy. The short length (less than 1 m) and low energy (only several millijoule) of a single NIR filament limit these applications. Long-pulse UV filaments have therefore been proposed at UNM to overcome such limitations. This dissertation describes our investigation and optimization of the high-power UV source, focusing on details of the generation and characterization of the generated pulses, as well as the applications of UV filaments for remote sensing and high-voltage discharge.

On the topic of pulse generation, a 266 nm UV system delivering laser pulses below 200 ps with up to 0.4 J per pulse at 1.25 Hz repetition rate is developed. Two aspects of the laser source are closely investigated. On the one hand, the spatio-temporal profile of the laser pulses that has been overlooked for decades is systematically studied. It is shown that a curved energy front, i.e., pulses away from the beam center delayed from the center

pulse, originates from the Q-switched unstable cavity Nd:YAG oscillator and evolves during the processes of laser amplification and pulse compression. To eliminate the energy front curvature, a possible solution is proposed based on the numerical simulation. On the other hand, a long existing debate on the minimum pulse duration that can be achieved through stimulated Brillouin scattering (SBS) pulse compression is resolved by this work. It is demonstrated that the lower limit of the compressed pulse duration is not set by the phonon lifetime of the SBS medium. The energy exchange between the pump and compressed Stokes pulses is responsible for the pulse compression below phonon lifetime.

Next, using the newly developed powerful and stable UV source, the generation of UV filaments in air is studied. It is shown that, when focused by a 3 m lens, a single filament is generated inside the laboratory, while multiple filaments are observed in an open environment with a 9 m focusing lens. Detailed characterization of the filament spatial profile and the conductivity of the plasma channel created by the filament are performed.

Two applications of the UV filaments are investigated. The single UV filament is applied to spectroscopy studies, including both Raman and Laser Induced Breakdown Spectroscopy (LIBS). A UV filament is shown to be very efficient in exciting forward stimulated Raman scattering (SRS) in gases. Backward emission of SRS signal, which could be utilized for remote sensing, has not been observed. However, a side experiment carried out in water discloses a new mechanism of driving efficient backward SRS generation, which can possibly be employed in the case of gas medium. A second study with the single filament is carried out for LIBS. The dynamics of self-absorption dip in LIBS spectrum is investigated, which can be further applied for the high resolution spectroscopy.

The last application is filament-induced high-voltage discharge. A fully guided 40 cm long discharge is demonstrated with the UV filament alone, at 1/2 the self-breakdown voltage in air. Two additional lasers are tested to improve the discharge triggering by photodetaching oxygen negative ions and heating the plasma. The anticipated improvement in reducing the discharge delay or enhancing the discharge probability has not been observed.

Contents

List of Figures

List of Tables

Chapter 1

Introduction

Self-focusing is a well known nonlinear optical phenomenon that has been experimentally discovered in 1964 [1]. When an intense light beam has power above a critical value P_{cr}, it creates an index gradient along its cross-section associated with its intensity distribution. Then, the index distribution of the optical medium with positive susceptibility χ^3 behaves like a positive lens thereby focusing the beam. The direct consequence of self-focusing effect is to create damage tracks made up of small bubbles lasting 2 cm in length [1], when Q-switched nanosecond pulses are focused into transparent glass. Since then, self-focusing is considered as one of the major limiting factors in the development of high-power lasers on the engineering side. From the scientific research side, the observation of damaged tracks has triggered extensive studies in laser filaments for half a century.

Before the experimental observation of laser filaments, an intense beam might propagate without diffracting has already been proposed [2]. In 1966, Garmire *et al.* [3] have reported the observation of laser filaments of $\sim$100 μm in diameter lasting more than 10 cm in CS_2. Chiao *et al.* [4] have reported the observation of multiple filaments at laser power much higher than the critical value. The modulation instability in both amplitude and phase of the laser beam has been suggested to break the self-focused beam into many filaments [5].

Limited by the available laser power, the early studies have mainly focused on the high nonlinear index media such as liquids and solids. Therefore, the filament range under investigation is quite limited.

In 1990s, with the development high-power femtosecond Ti:Sapphire lasers, long-range laser filaments have been directly observed in air [6, 7], which has opened a new page for laser filament studies. Laser filaments in air have peculiar properties [8] such as long-range propagation, generation of continuous plasma track in the wake of it, high intensity clamping (sub-TW/cm^2 to 100 TW/cm^2 depending on the laser wavelength) and high robustness (immune from fog or small particle perturbation). Different applications such as remote sensing [9, 10], high-voltage discharge triggering [11–13], remote measurement of high static electric field [14], water condensation [15, 16], microwave guiding [17] and attosecond pulse generation [18], have all been attempted based on different properties of the laser filaments. So far, the major focus of the studies has been confined into the near-infared (NIR) femtosecond filaments. Since a single NIR filament is limited by its short length (less than 1 m) and low energy (only several millijoule) in applications such as remote sensing and lightning triggering, long-pulse UV filaments have therefore been proposed at UNM to overcome such limitations. Theoretical studies [19] have shown that a single UV filament is capable of propagating much longer distance, while also carrying two orders of magnitude more energy as compared to a single NIR filament. Experimental works are needed to confirm theoretical predictions.

Previously, two dissertation works [19,20] have been devoted to develop the high-power UV source. Since the critical power for 266 nm laser pulses in air is about 0.13 gigawatt (GW), it is desired for the UV system to deliver 1 GW peak power pulses (i.e., pulses of sub-nanosecond duration with sub-Joule energy at 266 nm) for stable UV filaments generation. Such UV system is not commercially available. Its development has been shown to be a big challenge. Therefore, these dissertations have presented limited results on the applications of UV filaments. The present work describes our further investigation and optimization of

the high-power UV source, focusing on details of the generation and characterization of the generated pulses, as well as the applications of UV filaments for remote sensing and high-voltage discharge. This dissertation will be organized as follows.

The following two Chapters focus on two aspects of the UV laser source. In Chapter 2, we study the spatio-temporal profile (i.e., spatial distributions of pulse width and delay) of laser pulses obtained from a high-energy Nd:YAG laser, which has an unstable cavity design for the oscillator. We will show that the spatio-temporal profile originates from an unstable oscillator, and evolves during the amplification process. In the end, it is found that the spatio-temporal profile commonly exists in high-energy laser pulses. Chapter 3 investigates stimulated Brillouin scattering (SBS), which is employed to generate high-energy GW peak power pulses. The major efforts will be put on the generation of sub-nanosecond pulses shorter than the phonon lifetime. From there, the long existing debate on the minimum pulse duration that can be achieved through SBS pulse compression will be resolved.

Chapter 4 is devoted to the generation and characterization of sub-nanosecond UV filaments in air. Different initial conditions for the generation of UV filaments will be explored. The next two Chapters focus on the applications of UV filaments for remote spectroscopy and high-voltage discharges. In Chapter 5, both Raman and Laser Induced Breakdown Spectroscopy (LIBS) with UV filaments are investigated. We will demonstrate the forward vibrational and rotational Raman scattering excited by UV filaments with high efficiency. Backward emission of SRS signal, which could be utilized for remote sensing, has been searched but without success. For the backward emission of SRS signal, we will show a side experiment carried out in water. The results will disclose a new mechanism of driving efficient backward SRS generation that can possibly be employed in the case of gas medium, with which the backward SRS signal has not been observed with UV filaments in air. A second study with the single filament will be carried out for LIBS. The dynamics of a self-absorption dip in LIBS spectrum will be investigated, which can be further applied

for the high resolution spectroscopy. Chapter 6 focuses on the application of UV filaments in high-voltage discharges. It will be shown that UV filaments are better suited for laser-induced discharge because of the creation of high conductivity plasma channel. In order to enhance the capability of UV filaments in triggering the high-voltage discharge, two extra laser pulses will be employed to photo-detach oxygen negative ions and heat the plasma. We will be showing that the anticipated improvement in reducing the discharge delay or enhancing the discharge probability has however not been observed. Finally, Chapter 7 concludes this dissertation work devoted to sub-nanosecond UV filament study.

In the appendices, we will describe part of the PhD works that have focused on the timescale of femtosecond to attosecond, much shorter than the sub-nanosecond addressed in the main body of this dissertation. The development of femtosecond laser and the associated laser technology of carrier-envelope-phase (CEP) stabilization will be presented in detail, while a brief mention of the application of CEP stabilized femtosecond pulses to attosecond pulse generation will also be made.

Chapter 2

High-energy Nd:YAG laser system: A revisit

2.1 Introduction

As mentioned in the previous chapter, it is desired to have a UV system that delivers laser pulses of sub-nanosecond duration with sub-Joule energy. The high-energy requirement is often satisfied by employing Q-switched nanosecond lasers. Therefore, the starting point of our project is a high-energy nanosecond laser system. For our application, the requirements, purposes and solutions for such system are summarized in Table 2.1. Based on the design considerations, a flashlamp-pumped, Q-switched Nd:YAG laser system with Master Oscillator Power Amplifier (MOPA) configuration has been employed. An unstable resonator design has been chosen because of its large output energy. We refer to the work of Xu [20] for a detailed description of the system design. In this dissertation work, we will focus on the following three parts. First, we will discuss the redesign of the pump chamber of the first four amplifiers. As compared to the old design, the new pump chamber provides slightly better energy efficiency and a more uniform spatial pulse width distribution.

Second, we will discuss in detail the spatio-temporal profile, which refers to the spatial distribution of pulse width and pulse delay between pulses emerging from different radial positions across the beam cross section. Even though similar high-energy laser systems have been developed, the spatio-temporal profile of the laser pulses has not been explicitly investigated. Therefore, a revisit to such system is necessary. Third, the harmonic generation employed for frequency conversion in the depletion regime will also be addressed.

Table 2.1: Design considerations for high-energy laser system

Requirements	**Purposes**	**Solutions**
IR laser pulses of several Joules per pulse	Sub-Joule UV pulse generation	Flashlamp-pumped, Q-switched Nd:YAG laser with Master Oscillator Power Amplifier (MOPA) configuration
Flat-top or super-Gaussian spatial profile	Uniform SBS pulse compression (intensity dependent) across the beam cross section	Employing unstable resonator
High energy extraction efficiency	Cost effective	Employing unstable resonator
Single longitudinal mode operation	Stable SBS pulse compression	Development of real-time resonance tracking method [21]

Nd:YAG is employed because of its high gain and good thermal and mechanical properties. It is by far the most commonly used solid-state laser for high energy application.

2.2 Master oscillator power amplifier system

The laser system is home-designed to deliver laser pulses either directly at 1064 nm or at 532 nm via frequency doubling. Figure 2.1 presents the schematic diagram of the laser system. It begins with a Q-switched unstable oscillator (positive-branch confocal geometry), operating at 1064 nm at a repetition rate of 1.25 Hz. The oscillator could be operated with either multi (unseeded) or single longitudinal (seeded) mode. The single longitudinal mode with high fidelity is achieved by employing injection seeding combined with a

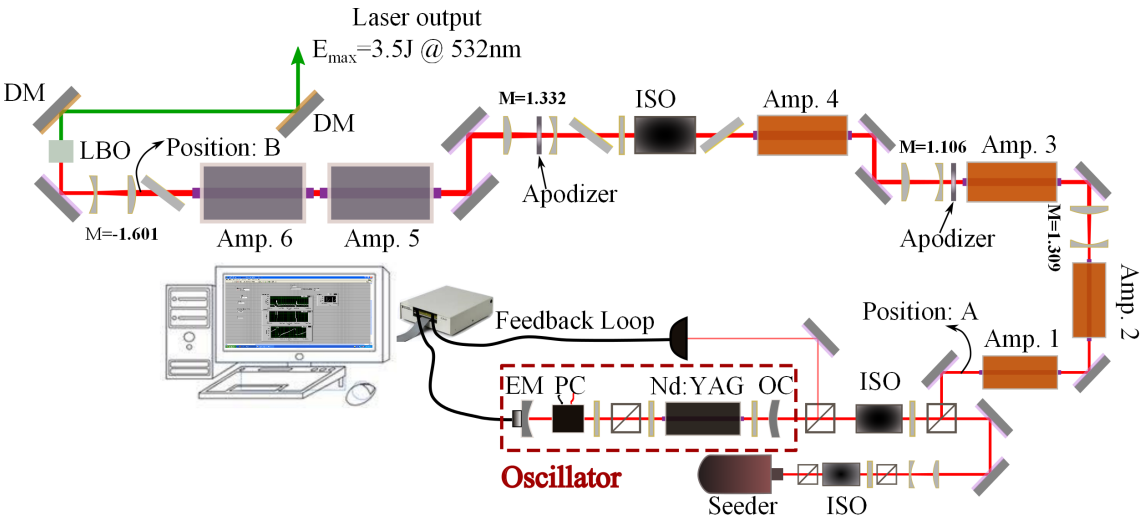

Figure 2.1: Schematic diagram of the high-energy Nd:YAG laser system. The Nd:YAG oscillator, seeded by a 60 mW CW seeder, has an unstable resonator design, which includes a concave end mirror (EM) and a convex output coupler (OC) with super-Gaussian reflectivity profile. It is Q-switched by a Pockels Cell (PC) to deliver a couple of nanoseconds pulses, which are amplified by a chain of 6 single-pass amplifiers (Amp. 1-6). The IR pulse at 1064 nm obtained after the 6^{th} amplifier is then frequency doubled through a LBO crystal with maximum conversion efficiency of 70%. For the measurement of spatio-temporal profiles, the oscillator and amplified pulses are coupled out from position A and B, respectively, to be characterized. The un-compressed green pulse after the second dichroic mirror is magnified by a telescope with M=3.31 (not shown here) and then characterized after that. ISO: Faraday isolator; DM: Dichroic (long pass) Mirror; M=1.3 denotes that the telescope has a magnification of 1.3.

real-time resonance tracking method [21]. The output energy of the oscillator is 100 mJ in injection-seeded operation and 140 mJ in unseeded operation, at the electrical pumping energy of 48 J for both cases. They are boosted to be 5 J and 7 J, respectively, after a chain of six single-pass amplifiers. It should be pointed out that, with a stable resonator design, the oscillator output energy would be much less as compared to that of an unstable resonator. Due to the low input energy fluence to the laser amplifiers, the energy extraction efficiency and thereby the output energy of the amplifiers would be reduced too. If the same amount of output energy is sought, one or two extra amplifiers would have to be employed, which would make the system to be less cost effective. Another shortcoming of utilizing a stable

resonator is that it outputs a much longer laser pulse, which is not desired in the application of SBS pulse compression, as will be discussed in the next Chapter.

The first four amplifiers employed in the system detailed in Xu's work [20] have been operated for almost ten years. During this dissertation work, it has been noticed that the laser system produces less and less output energy. After trouble shooting, it is found that the reflector of the pump chamber has degraded. Figure 2.2(a) shows the picture of the degraded pump chamber reflector. The reflecting surface is made of silver, coated with thixotropic space-grade silicon rubber. The latter acts as an adhesive and overlay protector that is resistant to photochemical degradation. Once the rubber layer has degraded (e.g. peeling off), the silver reflector is exposed directly to the flashlamp emission, and is corroded away by the combined action of the UV light and the de-ionized water. The degraded pump reflector then leads to less population inversion thereby lower efficiency for the laser amplifier.

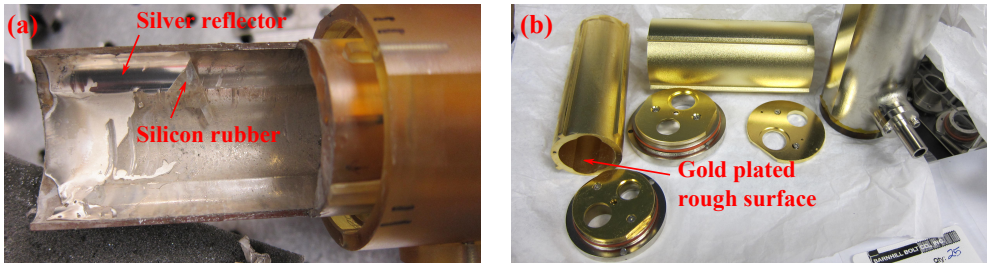

Figure 2.2: (a) Degraded pump chamber with original design; (b) Newly designed pump chamber with gold plated reflecting surface.

For our new design of the pump reflector, an aluminum block plated with gold, as shown in Fig. 2.2(b), is adopted to provide broadband reflection to the flashlamp emission. In this case, the gold should be much more resistant to any kind of degradation as compared to the silicon rubber. The rough surface is specially chosen for the reflecting surface to achieve better pump uniformity. The energy performances of the original laser (before degrading) is compared to the rebuilt laser in Fig. 2.3. The output energy is checked up to 4 J, i.e.,

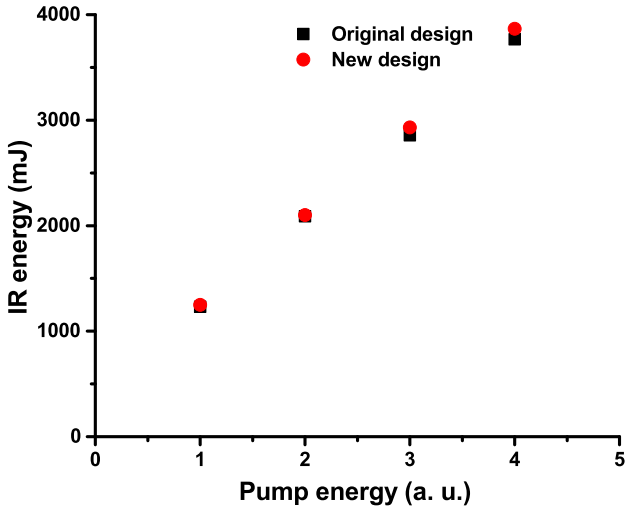

Figure 2.3: A comparison of energy performances between original and rebuilt laser systems

the working point of our whole system. It should be pointed out that the energies are taken at exactly same conditions for both the original and rebuilt systems. It is not surprising to see that both systems have similar energy performance, since the geometry of the newly designed pump chamber is exactly the same as the old one. However, as we will show later, the pump uniformity, which is manifested by the more uniform spatial pulse width distribution, has indeed been improved in the new laser system.

2.3 Spatio-temporal characterization of Nd:YAG laser pulses[1]

The spatio-temporal profile of the amplified pulses has already been noticed and experimentally measured by Xu [20] but without explicit investigation. In this section, we will

[1]Portions of this section have been published in C. Feng *et al.*, Appl. Opt. **55**, 1603-1612 (2016) [22]

identify the spatio-temporal profile to originate from pulses out of an unstable resonator. The gain saturation effect inside the amplifiers is also found to modify the spatio-temporal profile of the oscillator pulses. We will first provide a background of this study and then show both experimental and simulation results.

2.3.1 Background

As mentioned above, the high-energy laser system often employs an unstable resonator design combined with amplifiers to achieve high efficiency, high energy as well as high beam quality. Since its first description by Siegman [23], the unstable resonator has been extensively studied both theoretically and experimentally [24, 25]. While combined with a variable-reflectivity output coupler [26, 27], the unstable resonator seems to surpass its counterpart, i.e., stable resonator, since it could deliver a near diffraction-limited beam with much higher output energy. However, studies [28, 29] have shown that the intensity profile of pulsed unstable oscillators evolves with time. More specifically, the laser beam starts to build up from the optical axis with a Gaussian shape at the early time of the laser pulse. It then evolves towards a ring shape at the trailing edge, due to gain depletion in the central area of the gain medium. In a similar study reported by Anstett *et al.* [30], it is found that the laser pulse generated from a stable cavity does not exhibit such an issue. In a very recent study by Dansson *et al.* [31], the spatial distributions of pulse width and delay between two pulses at different radial positions have also been experimentally investigated, for laser pulses generated by an injection-seeded Nd:YAG laser with unstable resonator. Differences of up to 4 ns in pulse width and up to 10 ns in pulse delay between a pulse from beam center and a pulse from beam edge have been reported.

The spatio-temporal behavior of the laser pulse from an unstable resonator, i.e., the temporal evolution of the intensity profile and the spatial variation of the pulse width and delay, would certainly limit its applications where the highest peak intensity is sought. The

above mentioned works [28–31] still have two questions unanswered. First, how does the injection-seeding affect the spatio-temporal profile of the laser pulse emerging from an unstable oscillator? Second, does the result reported by Dansson *et al.* [31] emanate from the oscillator or the amplifier? It has been demonstrated in different works [32–34] that both pulse width and delay can be modified during laser pulse amplification.

In this section, we focus on the complete characterization of spatio-temporal profiles of pulses emitted from each stage of the Nd:YAG system. Our measurements show that:

- Pulses emerging from an unstable resonator have an energy front with a curvature inversely proportional to the pump strength or optical gain. By Injection-seeding, the energy front curvature is enhanced due to reduction of the effective gain. The pulse width distribution has negligible spread across the beam cross section, for all the operation conditions.
- After laser amplification, the energy front curvature increases, as a result of gain saturation. Due to the same saturation effect, the amplified pulse exhibits longer pulse duration at the beam center and shorter pulse duration at the beam edge. The spatio-temporal profile of the amplified pulse observed here matches the one reported earlier [31].
- The frequency doubled green pulses exhibit slightly shorter pulse width as expected. The energy front curvature is maintained to be similar as the IR pulses.

2.3.2 Pulse characterization setup

The pulse characterization setup, sketched in Fig. 2.4(a), is used to measure the spatio-temporal profile of the laser pulses. The input beam is attenuated by an uncoated wedge. The two surface reflections from the wedge are used as the signal and reference beam, respectively. A negative lens is used to expand the beam, while measuring the oscillator out-

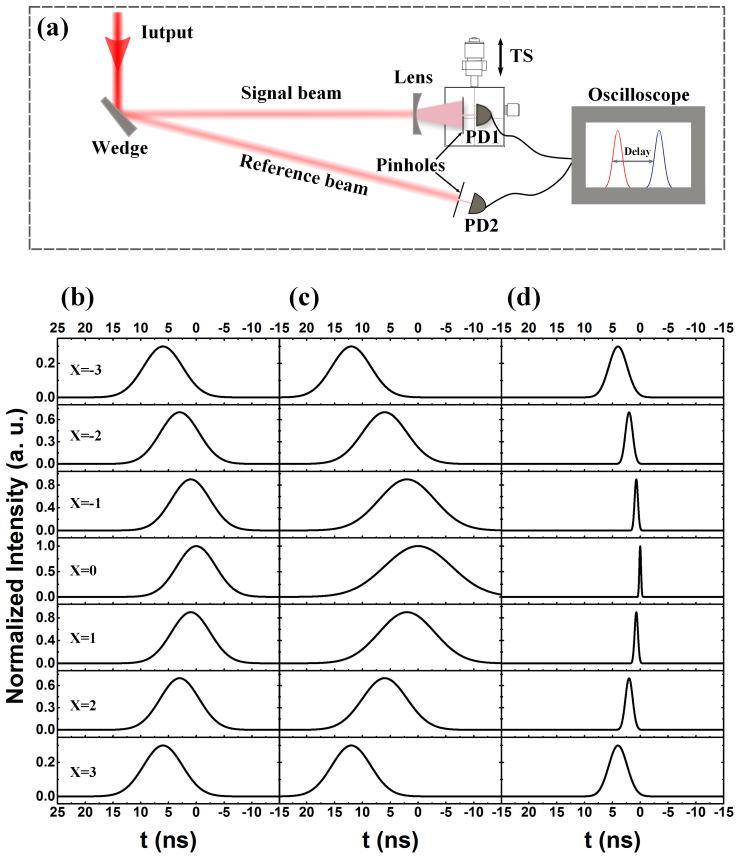

Figure 2.4: (a) Layout of the pulse detection setup; TS: Translation stage; PD: Photodetector. (b)-(d) Qualitative presentation of the spatio-temporal profiles of pulses emerging from unstable oscillator, laser amplifier and SBS compressor (will be presented in Chapter 3), respectively. X is the transverse coordinate in arbitrary unit.

put, to achieve better spatial resolution of the signal beam detection. For the measurements of the output from the laser amplifiers and SBS compressor, a collimated beam of more than 10 mm diameter is sampled directly by a 200 μm size pinhole. The signal beam transmitted through the pinhole is detected by a photodetector, either Thorlabs DET210 (350 MHz bandwidth) for the nanosecond pulse detection or Hamamatsu R1328U-52 biplanar phototube (rise time: 60 ps; spectral response: 185-650 nm) for measuring the sub-nanosecond pulse, which will be discussed in Section 3.5. Both pinhole and photodetector are translated together along the horizontal axis to spatially scan the beam diameter. The width as

well as the intensity of the signal pulse from each individual position are recorded by a digital oscilloscope (2.5 GHz bandwidth). Another set of pinhole and detector combination is employed to measure a reference pulse, sampled within the reference beam at an arbitrary position. The delay between the leading edge of a signal pulse and the reference pulse at the 50% intensity level is simultaneously measured by the oscilloscope. The energy front distribution of the signal beam could then be extracted from the delay measurements. The benefit gained from using an optical reference signal is to completely avoid the timing jitter between an electronic signal (for instance, triggering signal for the Q-switch) and the laser pulse. All the measurements are averaged over 50 laser shots, which further improves the accuracy of the delay measurements.

To illustrate the spatio-temporal profile that will be quantitatively discussed below, Figures. 2.4(b)-(d) show a qualitative presentation of the distribution and evolution of the profile. Two interesting features of the spatio-temporal profile will be focused on. First, the pulse width distribution has negligible spread across the beam cross section for the oscillator pulses [Fig. 2.4(b)], while it is spatially dependent for the amplified and SBS compressed pulses [Figs. 2.4(c) and (d)]. Second, the delay between pulses, referred as the energy front curvature, is also radial position dependent.

2.3.3 Numerical modeling

Caprara [29] and Anstett [30] have developed similar three dimensional (3-D) numerical models (i.e., 2-D in transverse direction plus 1-D in propagation direction), which have successively predicted the temporal evolution of the beam profile within a laser pulse. In this work, assuming cylindrical symmetry, a 2-D model considering only one dimension in the transverse direction is carried out to simulate the spatial variation of the pulse duration and pulse delay across the beam cross section.

Figure 2.5 describes the layout of the unstable oscillator used in the simulation. The

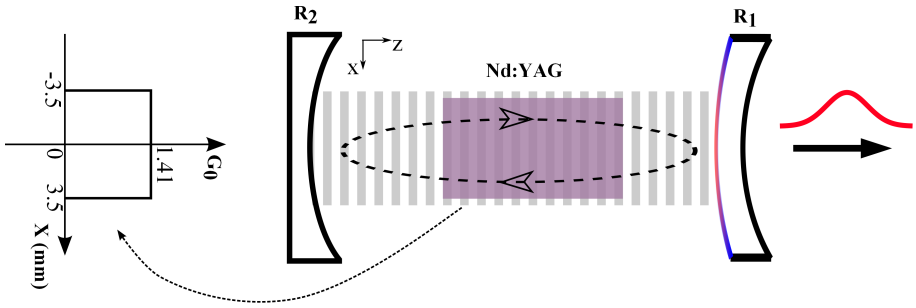

Figure 2.5: Layout of unstable Nd:YAG oscillator used in the numerical model.

cavity is formed by an output coupler with super-Gaussian reflectivity profile and a standard concave end mirror. Their field reflectivity profiles are listed in Eqs. (2.1) and (2.2), respectively:

$$r_1(x) = \sqrt{0.12}\exp\left(-\left|\frac{x}{w_1}\right|^{2.45} + i\frac{2\pi}{\lambda}\frac{x^2}{2f_1}\right) \tag{2.1}$$

$$r_2(x) = \exp\left(i\frac{2\pi}{\lambda}\frac{x^2}{2f_2}\right) \tag{2.2}$$

$$t_1(x) = \sqrt{1 - 0.12\exp\left(-2\left|\frac{x}{w_1}\right|^{2.45}\right)}\exp\left(i\frac{2\pi}{\lambda}\frac{x^2}{2f_3}\right) \tag{2.3}$$

where w_1 is the 1/e^2 super-Gaussian profile radius of 1.1 mm. f_1 and f_2 of -1.1 m and 1.7 m are the focal length of reflecting surfaces of the output coupler and end mirror, respectively. A 7 mm diameter $\times$ 115 mm length Nd:YAG rod with 0.8% doping is used as the gain medium, which is divided into seven slices in the simulation to achieve good accuracy. Each slice is assumed to have a uniform gain distribution as initial condition, which is typically valid for a gain medium with low doping concentration [25]. At the population inversion of $0.75 \cdot 10^{18}\text{cm}^{-3}$, the corresponding single-pass small signal gain is 1.41 for each slice [Fig. 2.5].

In the simulation, the transverse distributions of different components, such as electric field, free propagator, transfer functions of cavity mirrors and gain sheets with 30 mm diameter, are all digitized in the space domain with step size of less than 30 μm by one-

dimensional arrays of either complex numbers or real numbers. For instance, the initial electric field distribution at an arbitrary position along the optical axis is represented by a one-dimensional array of complex numbers. This complex array is propagated 36 steps (14 steps with gain and 22 steps without gain) inside the cavity to complete a round trip. The free propagation between two steps of 0.3 cm optical path length (L) is computed in frequency domain, by multiplying the complex field by the free propagator. The analytical expression of the latter in space domain is described in Eq. (2.4). The transformation from space domain to frequency domain and vice versa utilizes the one-dimensional fast Fourier transformation (FFT) algorithm. The effect of cavity mirrors on the complex field is modeled by multiplying the input field by the transfer functions of the reflecting surfaces, as described above. The amplification process is simulated via Frantz-Nodvik equation [35], as shown in Eq. (2.5).

$$h\left(x\right) = \sqrt{\frac{i}{L\lambda}} \exp\left(-i\frac{2\pi}{\lambda}\frac{x^2}{2L}\right) \tag{2.4}$$

$$W_{out} = W_s \ln\left\{1 + \left[\exp\left(\frac{W_{in}}{W_s}\right) - 1\right] G\right\} \tag{2.5}$$

W_{in} and W_{out} are the input and output energy fluence, respectively. W_s is the saturation fluence with a typical value of 0.67 J/cm^2 for Nd:YAG. The distribution of gain G within each gain slice is updated after each passage of the complex field. Since the gain medium is pumped by a pulsed flash-lamp, gain recovery is neglected during the whole process of pulse formation. The final output of the oscillator is computed by multiplying the intra-cavity field distribution by the transmission profile [Eq. (2.3)] of the output coupler. The transmitted beam is slightly defocused by the output coupler with a focal length f_3 of -10.5 m.

To simulate laser amplification, the above described codes for free propagation and pulse amplification are employed. The first two amplifiers are simulated and compared to the experimental results. The Nd:YAG rods of 7 mm diameter $\times$ 115 mm length and 8 mm diameter $\times$ 115 mm length for the first and second amplifier, respectively, are both divided the same way into seven slices. The corresponding time resolution is of 0.1 ns. The

population inversion within two amplifiers are set to be $0.63 \cdot 10^{18}\text{cm}^{-3}$ and $0.6 \cdot 10^{18}\text{cm}^{-3}$, corresponding to the electrical pump energy of 40 J and 50 J in the experiment, respectively. The gain distribution along the x-axis is also assumed to be uniform. The simulated output from the oscillator is used as the input for the first amplifier.

2.3.4 Spatio-temporal characteristics of pulses out of an unstable oscillator: Unseeded and Injection-seeded operations

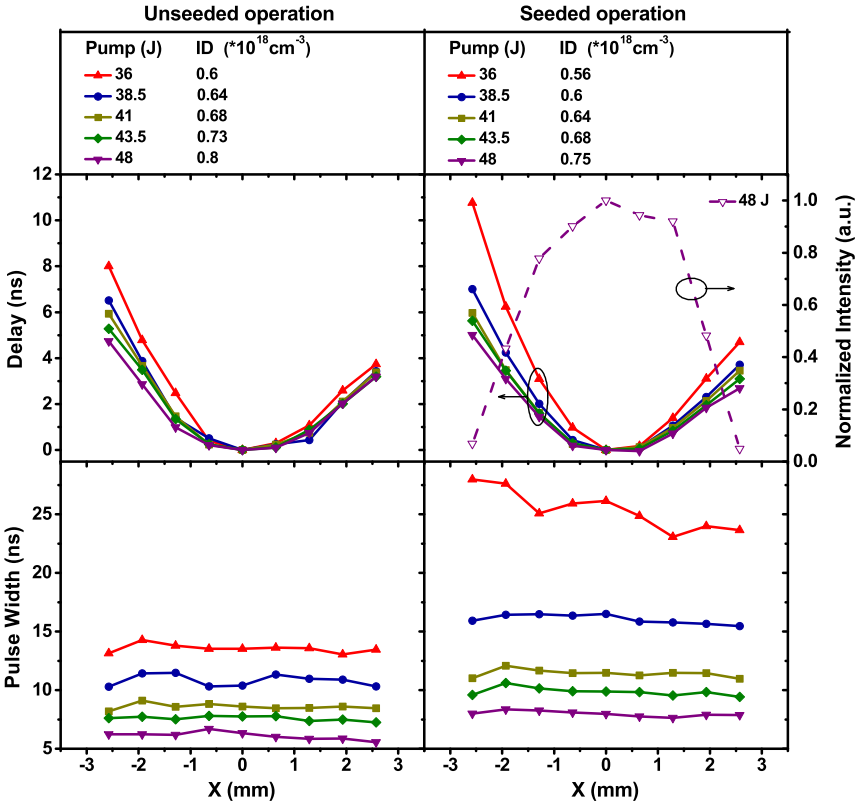

Figure 2.6: Measured spatio-temporal profiles of the oscillator pulses; Left: Unseeded operation, Right: Injection-seeded operation; ID denotes inversion density.

The spatio-temporal profiles of the oscillator pulses are experimentally characterized and presented in Fig. 2.6. The x-axis has been converted from the measurement to represent

the real size of the laser beam right after the oscillator output coupler, by deconvolving the defocusing effect of both output coupler and the negative lens used in the measurement, as well as the diffraction effect for propagation. In order to have a direct comparison with the simulation presented later, the effective inversion density is obtained by assuming a direct proportionality between electrical pumping energy and the inversion density. The conversion factors used in Fig. 2.6 are $1.667 \cdot 10^{16}$ J^{-1}cm^{-3} for unseeded operation and $1.563 \cdot 10^{16}$ J^{-1}cm^{-3} for seeded operation.

For both injection-seeded and unseeded operations, the energy front curvature is decreasing with increasing pump, and then saturates to a certain value as demonstrated in Fig. 2.6. By comparing the two operations at the same pump level, the energy front curvature is shown to be always larger for the injection-seeded operation than that of the unseeded case. The difference in energy front curvature for two operations is also getting less as the pump increases, similar to the saturation behavior described above. The asymmetric distribution observed in the pulse-front distribution is attributed to pump asymmetry, which is confirmed by the pulse intensity measurement as indicated in the same figure. At a maximum pumping energy of 48 J chosen to ensure the single longitudinal mode quality of the seeded operation, the pulse at beam edge (with $\sim$6% of the pulse intensity at beam center) is delayed by 4-5 ns, only half of that reported earlier [31], with respect to the pulse emitted at beam center. The pulse width also decreases with increased pump as expected. However, instead of varying significantly with radial position inside the beam [31], the pulse width is relatively constant across the beam at each pump input for both operations. At the lowest pump of 36 J where the laser operates just above the threshold with only 15 mJ of output energy for the seeded operation, the pulse width is more sensitive to the pump asymmetry.

In order to make a comparison with experiment, two differences are considered in the simulation in order to distinguish seeded from unseeded operation. First, an initial electric field equivalent to a fluorescence level of incoherent light (random phase) is applied for the unseeded operation, while an initial electric field with constant phase and 10 times

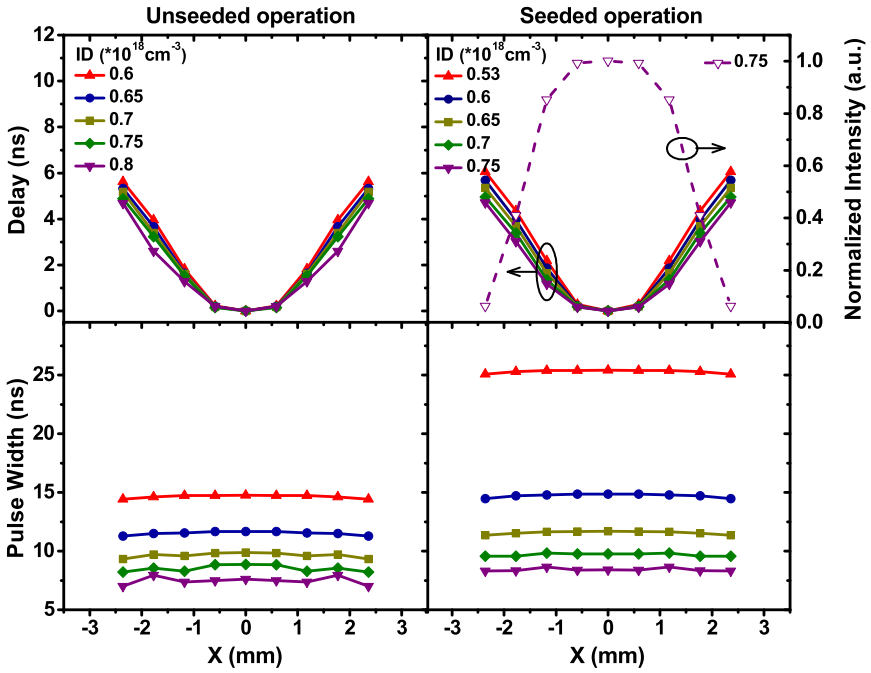

Figure 2.7: Simulated spatio-temporal profiles of the oscillator pulses; Left: Unseeded operation, Right: Injection-seeded operation; ID denotes inversion density.

stronger amplitude is employed for the injection-seeded operation. The difference in initial condition leads to a shorter pulse build-up time for the injection-seeded operation as compared to its counterpart, which matches the experimental observation. Second, the injection-seeding forces the oscillator to operate in a single longitudinal mode. The output energy of the injection-seeded operation has been experimentally observed to be lower than that of the unseeded operation, even if the two operations are both pumped at the same level [20, 36]. The energy decrease has been elaborated in two different ways. On the one hand, it is explained as owing to a smaller number of modes operating, there is less gain available for the seeded case [36]. On the other hand, it is found that the generation of seeded pulses encounter more loss in the case of slow Q-switch being used [20]. To address both possibilities, the reduced effective gain is adopted in the simulation of seeded operation. The population inversion is therefore set to be lower for the injection-seeded

case. As is shown in Fig. 2.7, the above considerations match the simulation results with the experimental observations. It should be pointed out that the inversion density used in the simulation does not match exactly the one from experiment. It has been chosen such that the simulated pulse width matches the experimentally measured one, especially in the case of lowest gain available for the seeded operation.

The temporal evolution of the spatial intensity profile [30] has been explained as gain depletion happening first on the optical axis because of the highest mirror reflectivity, and next at the beam edge. Similar concept has been used to interpret the formation of a parabolic-shaped energy front [31], where the pulse builds up first on the resonator axis and the formation of a pulse at the beam edge requires a longer build-up time. However, to fully understand the negligible spread of pulse width distribution across the beam, a further consideration of the cross coupling between the inner and outer regions of gain medium, due to the geometric magnification design, has to be introduced. Moreover, the dependence of energy front curvature on optical gain and injection-seeding still needs to be discussed. The above discovered features could be explained as follows:

- *Pulse width distribution:* Since part of the photons generated on axis would always be coupled to the outer region, the pulse formed firstly on axis would seed the generation of pulses away from the beam center. Therefore, the pulses emerging across the beam show similar pulse width in both experiment and simulation.

- *Dependence of energy front curvature on optical gain:* The dependence of pulse build-up time T_b on optical gain has been shown to follow $T_b \propto 1/\left(N_i - N_{th}\right)$ [32], where N_i and N_{th} are the initial population inversion and threshold inversion, respectively. Since N_{th} is smallest on optical axis, the center pulse with shortest T_b will always lead other pulses generated away from the center, provided that N_i is uniformly distributed along both transverse and longitudinal directions. Therefore, energy front curvature always exists, as demonstrated in both experiment and simu-

lation. The delay between the edge pulse and the center pulse could be written as

$$T_d = \frac{\kappa \left(N_{th}^e - N_{th}^c\right)}{\left(N_i - N_{th}^c\right)\left(N_i - N_{th}^e\right)}, \tag{2.6}$$

where κ is a constant, N_{th}^e and N_{th}^c represent the corresponding threshold inversion at beam edge and beam center, respectively. It is obvious that T_d decreases as the optical gain (i.e., N_i) increases, and saturates at high pumping energy. Hence, the energy front curvature will be larger for the case of low pumping energy. As the pump increases, the energy front curvature decreases and its reduction saturates, following the saturation in the reduction of T_d.

- *Dependence of energy front curvature on injection-seeding:* For the case of injection-seeded operation, the available gain at a specific pump is reduced, evidenced by the lower output energy discussed earlier. Hence, larger energy front curvature is observed. The difference is more clear at low pumping energy. Due to the saturation effect discussed above, the energy front curvature for the injection-seeded operation is very close to that of the unseeded operation at high pumping energy.

2.3.5 Spatio-temporal characteristics of amplified pulses: Gain saturation effect

The high-energy Nd:YAG laser system is completed by sending the injection-seeded oscillator pulses to a chain of 6 single-pass amplifiers to boost their energies. In order to achieve efficient energy extraction as well as high energy stability, each amplifier is running in the saturation regime by having the input energy fluence close or even above the saturation fluence of 0.67 J/cm^2. It has been demonstrated that saturated laser amplification could lead to pulse shortening [33], provided that the input pulse has a sharp leading edge. In other cases, a lengthened pulse could also be obtained if an input pulse with slowly rising edge is getting amplified [37]. As in our oscillator, the Q-switch opening time is slowed

down to enhance the mode selectivity and to ultimately reach 100% single mode operation [21]. Hence, the oscillator pulse exhibits a relatively slow leading edge. The amplified pulse is therefore expected to have longer pulse width. To demonstrate this, the IR pulses are characterized after the 6th amplifier for the cases of either only operating the first two amplifiers or running six amplifiers together.

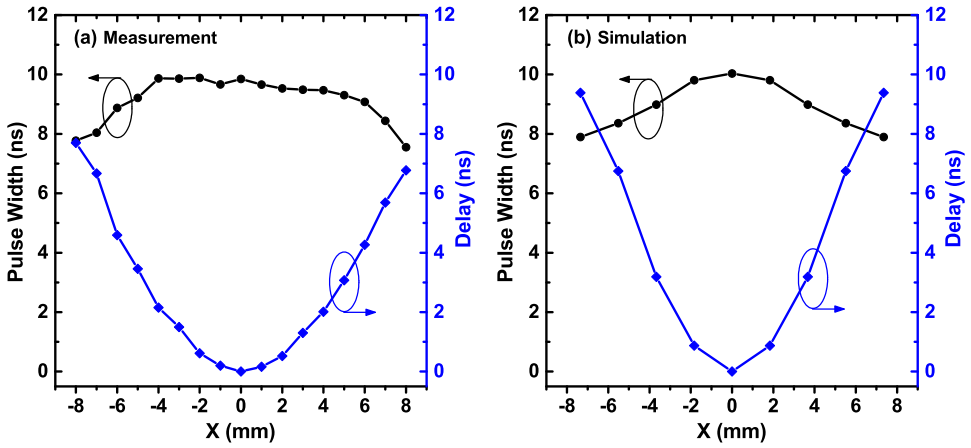

Figure 2.8: Spatio-temporal profiles of the amplified pulses obtained by operating only the first two amplifiers; (a) Measurement; (b) Simulation; The intensity of the pulse from beam edge is chosen to be $\sim$10% of that of the center pulse to match the experimental condition

Figure 2.8(a) shows the measured spatio-temporal profile of the amplified pulse with only the first two amplifiers operating. The amplified pulse emerging from the beam center exhibits a longer pulse width compared to the pulse from the beam edge. The amount of pulse delay between the center pulse and the pulse from beam edge is almost doubled, i.e., from 5 ns to 8 ns. Both observations could be understood as follows. The pulses located around the beam center typically have higher intensity, therefore experience more gain saturation. In the case of a center pulse, the strong leading edge depletes most of the available gain, which in turn sharpens itself, and moves forward. The trailing edge of the pulse being left almost unchanged. As a result, the gain saturation effect lengthens the pulse. For the pulses located away from the beam center, less gain saturation leads to shorter pulses. With less leading edge motion towards the pulse propagation direction, the delay

between the pulse from beam center and pulse from beam edge is enlarged. A simulation on the spatio-temporal profile of the amplified pulse is carried out, and its results shown in Fig. 2.8(b), for the case of operating the first two amplifiers. In order to compare with the experimental result, the x-axis of Fig. 2.8(b) has been converted from the simulated beam size after the second amplifier into the size after the 6^{th} amplifier, by considering the effects of three telescopes and the diffraction effect for propagation. To match the experimental condition, the intensity of the pulse from beam edge is chosen to be around 10% of that of the center pulse. As demonstrated in Fig. 2.8(b), the energy front curvature and pulse width are both qualitatively reproduced.

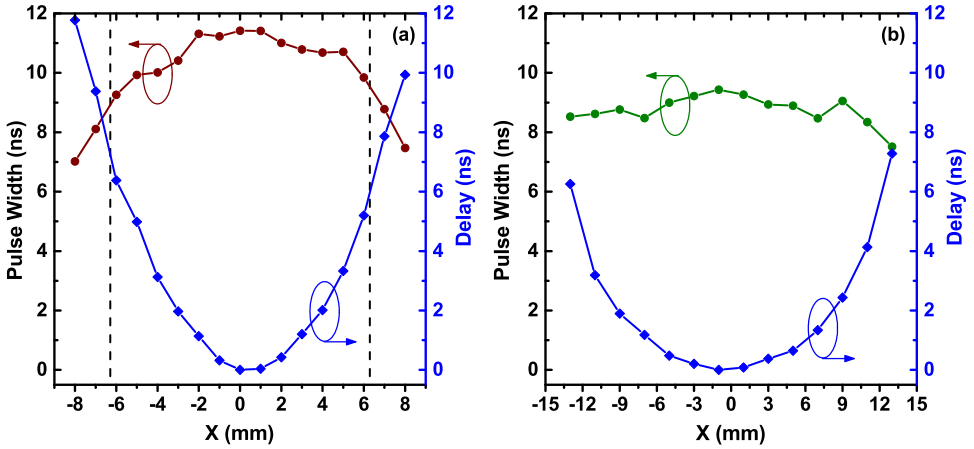

Figure 2.9: Measured spatio-temporal profiles; (a) IR pulse characterized at position B indicated in Fig. 2.1; (b) Green pulse characterized one telescope (M=3.3) after the setup shown in Fig. 2.1; The area between two dashed lines in (a) corresponds to the measured range in (b).

The amplified pulse is expected to have longer pulse width at the beam center and larger energy front curvature if more saturated amplification is experienced by the input pulse. Such a concept is demonstrated by the spatio-temporal profile of the amplified pulse for the case of running all the amplifiers, as illustrated in Fig. 2.9(a). The intensity of the pulse at the beam edge now is about 35% of that of the beam center. The maximum pulse width near the beam center reaches more than 11 ns (FWHM) at the output energy of 3.5 J.

The corresponding maximum delay is around 11 ns as well. We will show in the next Chapter that the SBS pulse compression is implemented at the wavelength of 532 nm. For a direct comparison of IR and Green pulses, the spatio-temporal profile of the latter is also characterized and presented in Fig. 2.9(b). The IR and green beams are characterized at different places, as mentioned in Fig. 2.1. The axis correspondence of the IR to the green measurement has been converted by considering different beam expander used between the two characterization positions. The area between two dashed lines shown in Fig. 2.9(a) corresponds to the diameter used for the green pulse characterization. One expected feature is that the green pulse exhibits slightly shorter pulse width compared to that of IR. However, the delay is kept almost unchanged, i.e., with a maximum delay of 6$\sim$7 ns. The green pulse is then sent to the SBS pulse compressor to generate high-energy sub-nanosecond pulse. In section 3.5, the spatio-temporal characteristics of SBS compressed pulses will be discussed.

2.4 Efforts on flattening the curved energy front

We have shown above that the curved energy front of the amplified pulses results from the combined effects of unstable resonator and gain saturation inside the amplifiers. In order to minimize the curved energy front thereby increase the focusing intensity, two ways have been tested to either eliminate the pulse delay for oscillator pulses or minimize the gain saturation effect from amplifiers.

2.4.1 Using a specially shaped high power seeder

It has been discussed in the previous Section that injection-seeding helps reducing the pulse build-up time. Therefore, it seems possible to compensate the oscillator pulse delay by using a specially shaped seeder beam, i.e., a beam that has higher intensity at the beam edge and lower intensity at the beam center, such that the edge pulse could start to build

up earlier. Based on this idea, a high power seeder beam with 500 mW CW power is employed and shaped to have a Gaussian dip at the beam center as shown in Fig. 2.10(a), by inserting another Gaussian reflectivity mirror into its path at a position between the first and second turning mirrors. The measurements taken at the two highest pumping energies of 43.5 J and 48 J, however, do not show clear effect on flattening the energy front curvature. Seeder beam with the same shape but at low power of 70 mW, which is controlled by the combination of a half waveplate inserted in between the two turning mirrors and the following coupling polarizer, has also been tested. As demonstrated in Fig. 2.10(b), the energy front curvature is always as much as the one shown in Fig. 2.6 This further emphasizes the saturation in energy front curvature, as demonstrated by the little difference in energy front curvature existing between the seeded and unseeded operations.

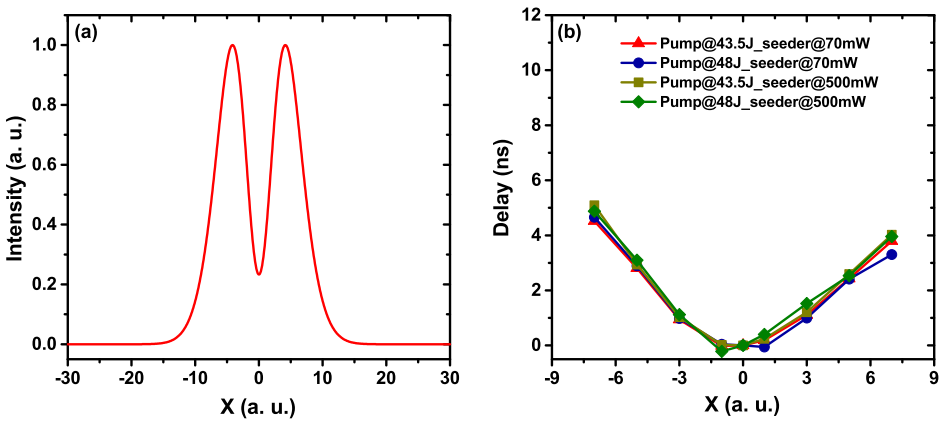

Figure 2.10: (a) Specially shaped high power seeder beam with low power density at the beam center; (b) Measured spatial delay distributions.

2.4.2 Using dye as saturable absorber to sharpen the leading edge of input pulses to amplifier

It has been mentioned earlier that the enlarged energy front curvature due to gain saturation effect inside the amplifiers only happens when the input pulses have relatively slow leading

edge. Therefore, a direct way to minimize the energy front curvature for the amplified pulses is to sharpen the leading edge of input pulses to the amplifier, which can be realized by using dye as the saturable absorber (SA). To test this idea, a specially designed dye cell to achieve laminar flow is put after the second amplifier. A picture of it is shown in Fig. 2.11 The two windows used in the cell are both air side AR-coated to minimize the reflection loss. The dye Q-switch 5 dissolved in dichloromethane is circulated through the cell by a speed adjustable pump.

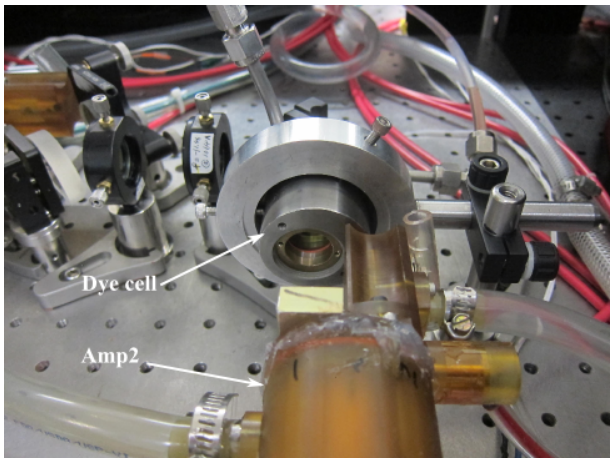

Figure 2.11: Specially designed dye cell to achieve laminar flow.

Figure 2.12 presents the measurements of spatio-temporal profiles of both IR and green pulses. It is worth noticing that those measurements are taken with the old pump chamber design that has been discussed in Section 2.2. As compared to the data demonstrated in Fig. 2.9, the new pump chamber design provides much better uniformity for the spatio-temporal profile distribution. The measurement shown in Fig. 2.12(a) is taken at the pulse energy of 3.5 J. The corresponding green energy after frequency doubling is around 2.2 J, at which point the spatio-temporal profile of the green pulses is measured and illustrated in Fig. 2.12(c). After applying the saturable absorber cell, the IR and green pulse energies have dropped 22% and 33%, respectively, when the same amount of pumping energy is used. As shown in Fig. 2.12(d), the pulse width and spatial delay of the green pulses

are both reduced. However, the maximum pulse delay is still as much as the pulse width of several nanoseconds. Moreover, to bring back the green energy to the working point of around 2 J, it requires more laser amplification that might further increase the delay. Therefore, it is concluded that saturable absorber is not efficient tool to minimize the energy front curvature.

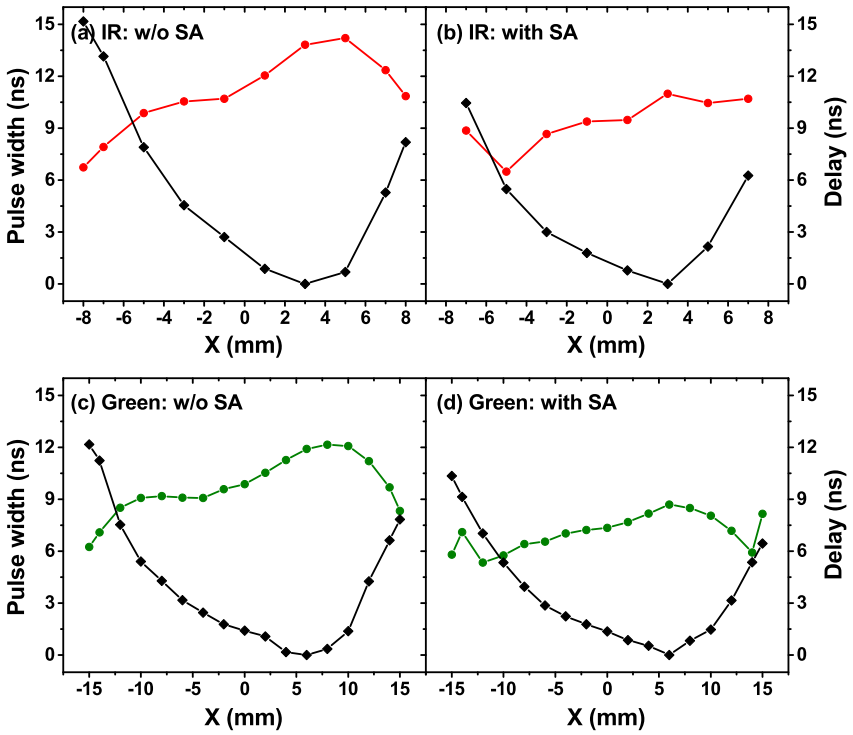

Figure 2.12: (a) and (b) Spatio-temporal profiles of IR pulses in the case of with and without using dye saturable absorber, respectively; (c) and (d) Spatio-temporal profiles of Green pulses in the case of with and without using dye saturable absorber, respectively.

2.4.3 Further possible solutions

Based on Eq. (2.6), there are two more possible solutions to alleviate the energy front curvature of the oscillator pulses. The first solution is to shape the transverse loss distribution, i.e., with lower loss at the beam edge and higher loss in the beam center. This solution is

easier to realize. However, the energy would probably be much reduced since the output is very sensitive to the internal cavity loss. Longer output pulse would also be expected. As discussed in the beginning of this Chapter, both changes are not preferred.

Another solution is to shape the distribution of initial gain or population inversion N_i, i.e., with higher N_i at the beam edge and lower N_i in the beam center, which requires much more technical complexity. In simulation, we have used the model described earlier to test this idea. Figure 2.13 presents the simulated gain and the corresponding delay distributions. It is clear that the gain shaping would help reducing the energy front curvature. In practice, the special gain distribution might be achieved by employing a highly doped gain medium [25].

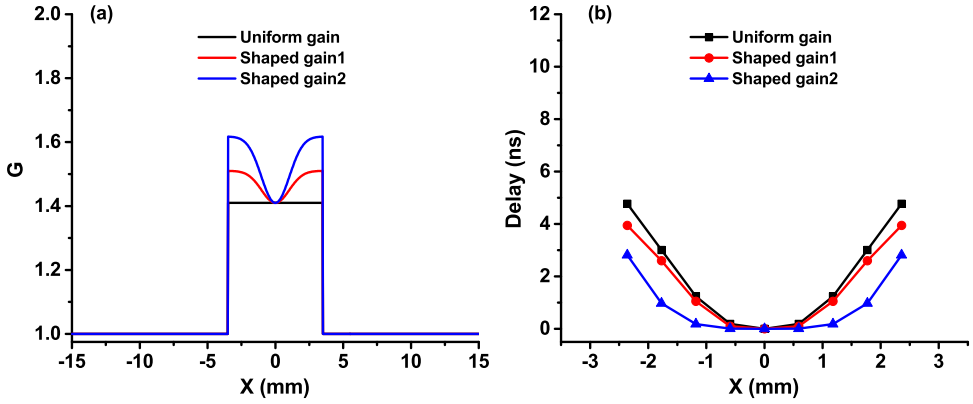

Figure 2.13: (a) Three different single slice gain distributions; The uniform gain distribution, which is the same as the one shown in the inset of Fig. 2.5, is employed for the simulation with results presented in Fig. 2.7. (b) The corresponding delay distributions.

2.5 Second harmonic generation in the depletion regime

Since its first demonstration by Franken *et al.* [38], second harmonic generation (SHG) has become the daily tool for frequency conversion in most of the optics research lab. In the

case of frequency doubling from 1064 nm to 532 nm, several nonlinear crystals, such as Potassium dideuterium phosphate (KDP and DKDP), Potassium titanyl phosphate (KTP) and Lithium triborate (LBO) are often employed. Among different choices, KTP is very popular because of its largest nonlinear coefficient d_{eff} of 3.58 pm/V[2] in the type II phase matching, which typically leads to high conversion efficiency. However, since it has relatively low damage threshold and often suffers from gray tracks, the KTP crystal is unfavored in our application of very high energy frequency doubling. For the consideration of high operation reliability, LBO (d_{eff}=0.832 pm/V, type I phase matching) has been chosen due to its high damage threshold (25 J/cm^2 @ 10 ns 1064 nm pulse). To further enhance the stability, the LBO crystal with a dimension of $W13.5 \times H13.5 \times L12.5$ mm^3 has been put into an home-designed temperature-stabilized oven, as demonstrated in Fig. 2.14. The temperature stabilization is realized by using a resistance temperature detector (RTD) as sensor and a PID controller to provide feedback to the heater (actuator).

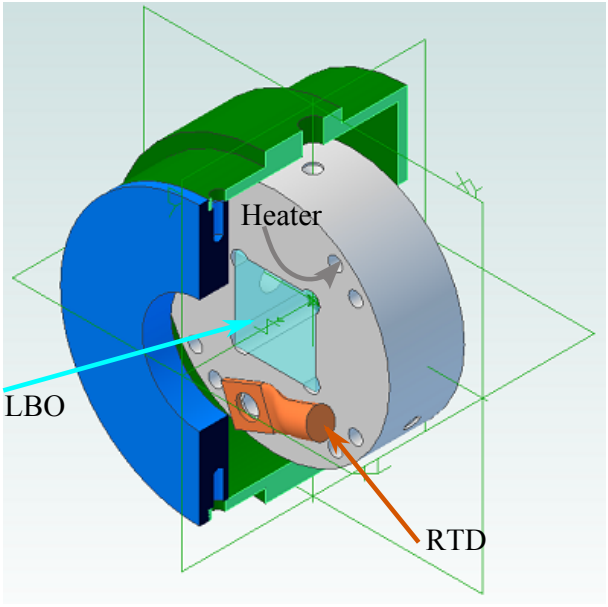

Figure 2.14: Home designed oven for LBO crystal to reach better SHG stability.

[2]Crystal data presented both here and in Section 3.6 are all quoted from SNLO [39]

In harmonic generation, it has been demonstrated that there are two regimes [40]. In the case of pump with negligible depletion, the intensities of input fundamental pulse and output second harmonic pulse have the relationship $I(2\omega) \propto I^2(\omega)$. When the conversion efficiency is high (i.e., with pump depletion), the previous relationship becomes to $I(2\omega) \propto I(\omega)$. In our case, if the IR input energy is scanned, we should be able to see this transition in two aspects. First, the dependence of green energy on the IR input energy should be nonlinear and then becomes linear as the IR energy is increased. Second, the IR/Green pulse width ratio should be the well known $\sqrt{2}$ at low conversion efficiency and then reduces to be close to one at very high conversion efficiency. The experimental results shown below will corroborate the above analysis.

2.5.1 Experimental and simulation results

In the experiment, the size of IR laser beam from the last amplifier is reduced to 10 mm (full width at $1/e^2$ maximum intensity) by using a telescope with M=-1.6. This helps to increase the input beam intensity such that high conversion efficiency could be achieved. Besides the experimental characterization, we also employ the SNLO program [39] to simulate the SHG in LBO. Both experimental and simulation results are presented in Fig. 2.15. It can be seen that the simulation matches experimental measurements very well. As shown in Fig. 2.15(a), the maximum green energy reaches 3.5 J when the input IR energy of 5 J is employed. The corresponding conversion efficiency is as high as 70%. The green energy fluctuation at the depletion regime (i.e., with green energy $>$ 500 mJ) is measured to be below 1%.

To explore the transition discussed above, the input energy to the LBO crystal is varied. At relatively low input energy that corresponds to low conversion efficiency, the green energies can be fitted very well with a parabolic function, as illustrated by the red curve. As the conversion efficiency further increases, a linear fit (green line) is found to be more

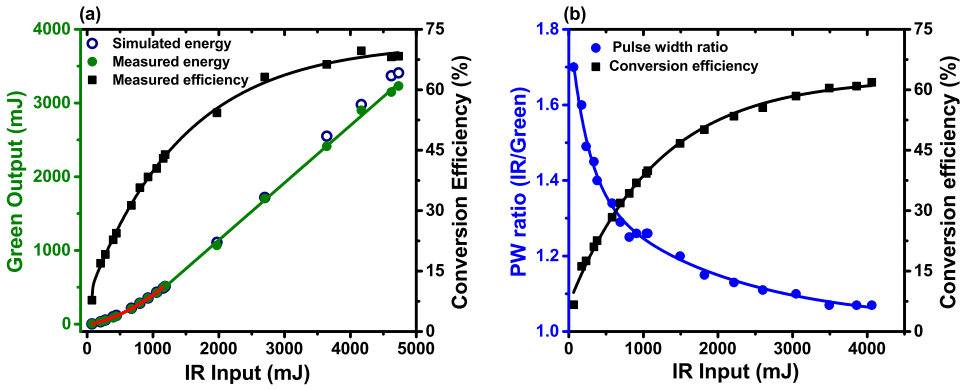

Figure 2.15: (a) Experimental and simulation results of green energy and the corresponding efficiency with different IR input energy; Two curves and a line are fits to the data. (b) Variation of IR/Green pulse width ratio and the conversion efficiency with different IR input energy; Two curves are fits to the data.

appropriate to the converted green energies. The change in IR/Green pulse width ratio has also been investigated and displayed in Fig. 2.15(b). It should be noticed that the ratio at low conversion efficiency does not correspond to $\sqrt{2}$, which is due to two reasons. First, the detector used to characterize green pulse has slightly better time resolution than that of the one used for IR pulse measurement. Second, we have shown earlier that both IR and green pulses have radial position dependent pulse width. Even though we have tried hard to find the spatial correspondence of IR and green pulses to be measured, a slight misalignment might still be existing, which would also modify the pulse width ratio. Nevertheless, we have seen that the difference between the IR and green pulse width becomes less as the conversion efficiency increases. Both transitions in energy and pulse width observed from experiment are all in agreement with the expectation.

Besides the characterizations of pulse energy and pulse width, the time integrated spatial profile of green pulse at the energy of 2 J has also been recorded and presented in Fig. 2.16. It should be noticed that apodizer apertures have been employed in the system (see Fig. 2.1) to maximize the beam filling factor inside the amplifiers while also avoiding the hard aperture diffraction. The sharp beam edge and strong edge modulation are both

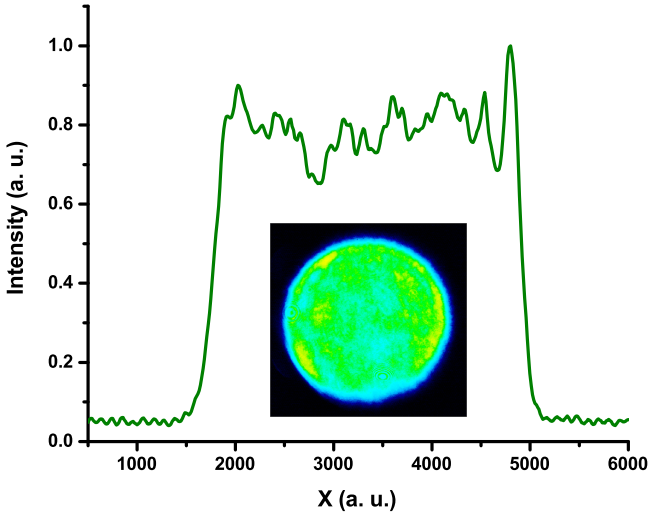

Figure 2.16: Time integrated green beam profile at the pulse energy of 2 J.

related to the aperture effect.

2.5.2 Spatio-temporal characteristics of frequency-doubled pulses

The spatio-temporal profile of frequency-doubled pulses with energy around 2 J has been demonstrated in both Fig. 2.9 and Fig. 2.12. It has been shown that the pulse width is reduced with a small amount while the delay is almost maintained after the frequency doubling. Therefore, we conclude that, in the case of SHG in the depletion regime, the frequency doubled pulses inherit the spatio-temporal characteristics of fundamental pulses.

2.6 System Summary

In this chapter, we have described our home-designed high-energy nanosecond Nd:YAG laser system. The system is running with single longitudinal mode and super-Gaussian spatial profile. The maximum energy of the frequency-doubled green pulses can reach

3.5 J with fluctuation less than 1%. The spatio-temporal profiles of the pulses obtained from each stage of the system have been investigated in detail. It has been learned that spatio-temporal behavior of high-energy pulses commonly exists. Even though the pulses with Gaussian shaped spatial profile from a stable resonator are free of pulse delay along the radial coordinate, much stronger spatio-temporal modification from amplifiers is also expected, since the energy fluence around the beam center is much higher than that of the beam edge as compared to the case of super-Gaussian beam. The ultimate solution to the issue would be shaping the laser beam from a stable resonator to have a real flat-top beam profile. The shaped beam is then sent to amplifiers to be amplified. In such a case, complex relay imaging systems are required since the shaped beam is not a free propagation mode anymore.

Chapter 3

High-energy sub-nanosecond pulse generation by SBS pulse compression in liquids

3.1 Introduction

The motivation in obtaining high-energy sub-nanosecond pulses is triggered by the UV filament study, which requires long (sub-ns to ns) UV pulses at 266 nm with gigawatt (GW) peak power. To achieve the same peak power, shorter pulses require lower pulse energy, and thus are easier to realize. However, it needs to be emphasized that the lower UV energy still means the level of sub-joule, which is not typical for any laboratory setup or even commercial product.

As discussed earlier, nanosecond pulses are routinely generated by Q-switching technique. The high energy (>1 J) output is realized by employing Master Oscillator Power Amplifier (MOPA) configuration. Sub-nanosecond pulses can also be obtained directly from a Q-switched microchip laser [41]. However, direct amplification of sub-nanosecond

pulses to the desired Joule level energy is limited by optical damage caused by self focusing. We will revisit self focusing in chapter 4, where it plays a key role in the generation of laser filament in air.

An alternative way to generate sub-nanosecond pulses is to compress Q-switched ns pulses to the sub-nanosecond regime, by exploiting nonlinear processes such as stimulated Raman scattering (SRS) or stimulated Brillouing scattering (SBS). The advantage in using SRS for pulse compression is its very short phonon lifetime, which guarantees shorter compressed pulse width. The implementation of SRS pulse compression is, however, hindered greatly by the competition between stimulated Raman and stimulated Brilloin scattering, by the competition between forward and backward SRS, as well as by the generation of high order Stokes and anti-Stokes components.

The SBS pulse compression is preferable since it is free of the drawbacks mentioned above. Since it was first reported by Hon [42], stimulated Brillouin scattering has been demonstrated to be an efficient and robust way to compress nanosecond pulses into the sub-nanosecond regime [43–50]. It continuously gains attention [49–52] because of its simplicity, high energy conversion efficiency and high temporal compression ratio.

So far, most of the studies on SBS pulse compression focused the energy range of a few mJ to 100s of mJ. In our case, the compressed pulses at either 1064 nm or 532 nm have to have $>$ 1 J energies in order to obtain sub-joule UV pulses. The direct compression at 266 nm has been attempted without success, because of the medium decomposition by the high energy photons. One of our efforts is therefore to push the energy load capacity of SBS compression to its highest level. Since obtaining shortest compressed pulse is as important as achieving highest compressed energy, another focus of our work is to reveal the key factors as well as the limitations in realizing high temporal compression ratio while still maintaining excellent reliability and reproducibility.

In this chapter, we will first provide some background information for the SBS pulse

compression. Following that, we will show the results of pulse compression in FC72 at 1064 nm and in water at 532 nm. The importance in selecting appropriate compressor configuration and SBS medium will be demonstrated therein. Then, we will present the high-energy sub-phonon lifetime compression both experimentally and theoretically. Our investigation shows different mechanism and limitation of the sub-phonon lifetime compression from compared to the previous report [53]. Since the input pulses to the SBS compressor have been shown to exhibit spatio-temporal profiles, the spatio-temporal characteristics of the SBS compressed pulses have also been investigated. Before concluding this chapter, the sub-nanosecond UV pulse generation via another second harmonic generation is reported.

3.2 SBS pulse compression: Background

3.2.1 Principle

Stimulated Brillouin scattering is a nonlinear process of interaction among three waves, i.e., two optical waves and an acoustic wave. Figure 3.1(a) is a schematic representation of the stimulated Brillouin scattering process. For an incident pump of high intensity, the Stokes wave scattered by the acoustic wave, which is initiated by the thermal excitation at the beginning, will be strong enough to beat with the pump wave. The beating between pump and stokes would reinforce the acoustic wave due to the electrostriction effect, whereas the beating between pump and the enhanced acoustic wave would reinforce the stokes wave. Towards the end, the positive feedback described by those two interactions leads to the amplification of Stokes by saturation of the pump.

Similarly, when a laser pulse is focused into the SBS medium, a counter-propagating Stokes pulse will be initiated around the beam focus. If the length of the SBS medium is long enough, the density grating, created by the interference between the pump and Stokes

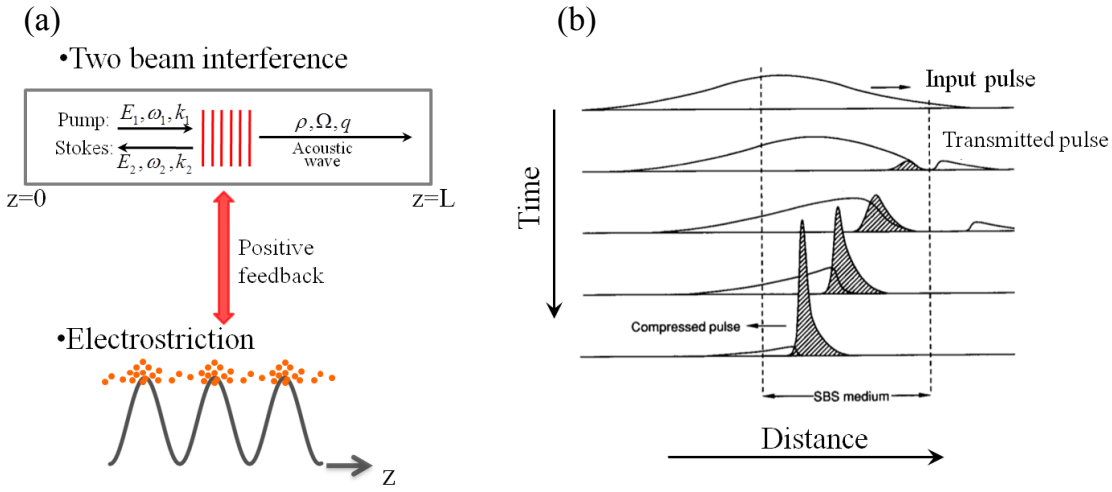

Figure 3.1: (a) Schematic representation of the stimulated Brillouin scattering process. (b) Illustration of pulse compression by stimulated Brillouin scattering [54].

pulse, will move along with the Stokes pulse at the speed of light. The moving grating then behaves like a mirror that pushes the photons from the pump pulse into the leading edge of Stokes pulse. As the interaction becomes stronger because of the positive feedback as mentioned above, the accumulation of energy into the leading edge of Stokes pulse gets more efficient, leading to a gradually shortened pulse as demonstrated in Fig. 3.1(b).

3.2.2 Configuration of SBS pulse compressor

For SBS pulse compression, there are three typical configurations, as shown in Fig. 3.2. The first two setups, i.e., single-cell setup [42, 55] and cascaded generator-amplifier setup [44, 45], are often employed, due to their simplicity in implementation. However, high pulse energy dumped into the beam focus would easily cause optical breakdown and other nonlinear competing processes such as self-focusing and stimulated Raman scattering with those two setups. The stability of pulse compression can not be guaranteed. For the cascaded two-cell setup, one could conceive to insert an filter in between the two cells to attenuate the energy sent into the generator, thus maintaining better stability. The energy efficiency

would however be dramatically reduced because of the large loss introduced by the attenuator [56].

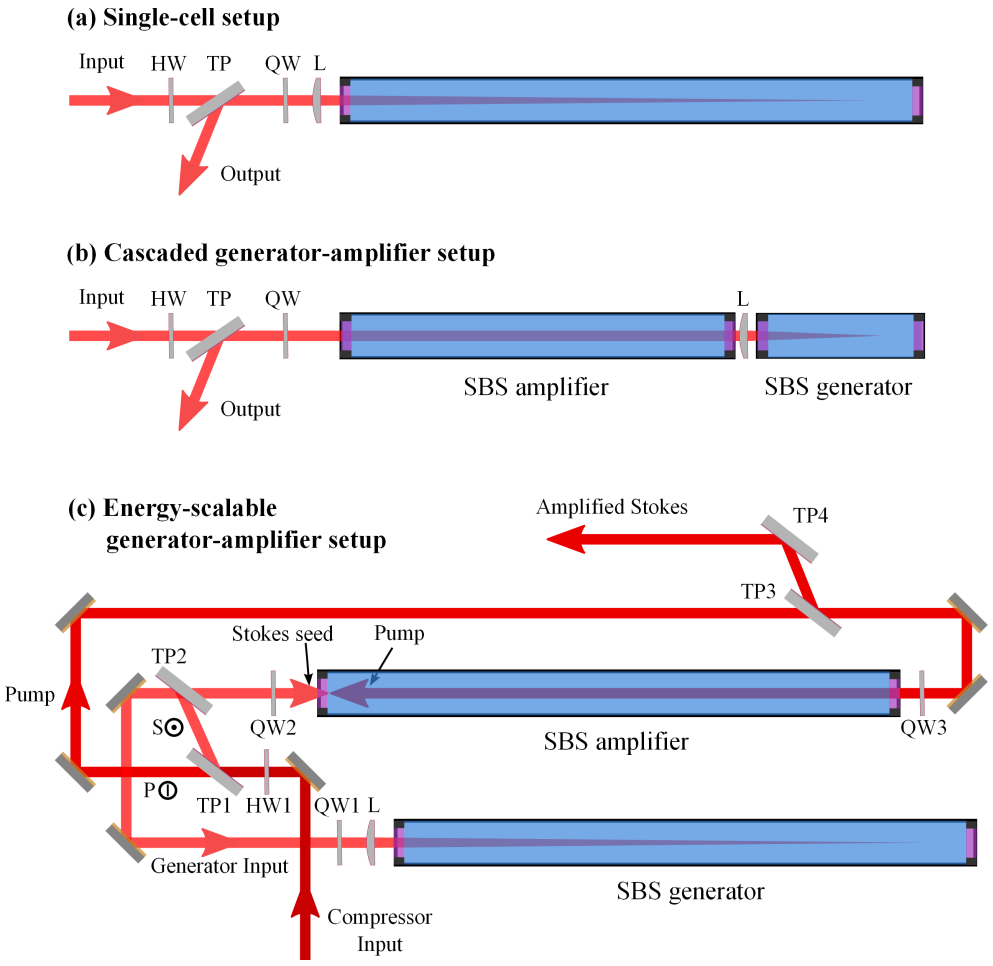

Figure 3.2: Three typical configurations implemented in SBS pulse compression; (a) Single-cell setup; (b) Cascaded generator-amplifier setup; (c) Energy-scalable generator-amplifier setup.

The best way to compress high-energy pulses with high fidelity is the energy-scalable generator-amplifier setup [54], as presented in Fig. 3.2(c). In this setup, the half wave-plate (HW1) and thin-film polarizer (TP1) are used to control the energy of the generator input pulse, which is reflected by two polarizers TP1 and TP2 thus with S polarization. The generator input is focused by a plano-convex lens (L) into the SBS generator to create a

pre-compressed Stokes seed pulse that propagates in the backward direction. After passing through the quarter wave-plate (QW1) twice, the initial S polarization of the generator input beam is rotated to be P polarization, which ensures the Stokes seed beam propagating through TP2 and reaching into the SBS amplifier. The main portion of the compressor input that passes through TP1 with P polarization is used as the SBS pump and sent into the SBS amplifier from the right hand side. The polarization of Stokes seed and pump pulses are changed to circular by QW2 and QW3, respectively. After the interaction between two counter-propagating pulses, their polarizations are modified to be S after going through the quarter wave-plate once again, which allows them to be reflected out by TP2 and TP3, respectively.

The difference between the cascaded and energy-scalable generator-amplifier setup is that the pulse energy sent into the generator in the latter setup can be finely controlled. Therefore, an optimum condition can be found to avoid all the negative effects associated with the focusing geometry as mentioned above, thus obtain very stable pre-compressed Stokes seed pulses from the SBS generator. Since the high energy pulses (i.e., the main portion of the input pulses) are sent into the SBS amplifier as collimated beams, there is no concern of optical breakdown happening there. Because of their lower gain as compared to that of SBS process, other nonlinear competing processes will not arise before the generation of SBS Stokes pulse by the pump itself, which acts as the only limiting factor for the maximum compressible energy. However, since the SBS gain ($G = g_B IL$) is proportional to the pump intensity and steady-state gain factor g_B, the energy load capacity could be simply enhanced by increasing the pump beam size or by choosing a low g_B material without introducing complication.

It should be mentioned that the merit of energy-scalable setup has not been completely displayed in its first demonstration [54]. Xu has systematically studied and optimized the performance of the energy-scalable generator-amplifier setup, which relies much on several key factors. More details about the optimization process are in references [52] and [20].

3.2.3 SBS medium

SBS pulse compression has been demonstrated in high-pressure gases [42, 44, 55, 57, 58], solid-state materials (fused-quartz and fused-silica) [59], as well as liquids [45, 46, 55, 60]. It has been proved that, only with liquid media, SBS pulse compression with high energy load capacity and high efficiency can be obtained. Among different choices, the heavy fluorocarbon (FC) liquids (FC-72, FC-75, FC-40, etc.) [47, 49, 56, 61, 62] are very popular due to their favorable properties, such as low absorption coefficient, moderate gain factor and high damage threshold, in SBS application.

Other than liquid fluorocarbon, water has also been explored in SBS applications [46, 48, 60]. The physical properties of FC72 and water are listed in Table 3.1. As compared to FC liquid, there are several advantages in using water as SBS medium. First, water is cheap and widely available even at the highest purity. Second, water shares many of the favorable properties of liquid fluorocarbon, such as short phonon lifetime and chemical stability. Moreover, its lower steady-state gain factor allows larger energy load capacity, as discussed earlier. Third, water has smaller $\partial n/\partial T$ as compared to that of FC liquid, where n is the refractive index of SBS medium and T is temperature. It should be emphasized that the effect of $\partial n/\partial T$ on SBS compression has barely been investigated before. Recently, we have shown that the beam pointing stability and beam quality can be severely distorted,

Table 3.1: Physical properties of FC72 and water associated with SBS application

Liquid	λ_P (nm)	$\Omega_B/2\pi$ Hz	g_B (cm/GW)	τ_B (ps)	T (^0C)	$\partial n/\partial T$ $(10^{-4}K^{-1})$	α $(10^{-6}cm^{-1})$
FC72	1064	1.1	6-6.5	590	25	-4.7	2.3
FC72	532	2.2	6-6.5	148	25	-4.7	<10
Water	1064	3.71	3.8-4.8	1180	25	-0.99	$(1.2-1.4)*10^5$
Water	532	7.42	3.8-4.8	295	25	-0.99	350-530

Data of FC72 cited from references [61, 63]. Data of water cited from references [64, 65]. Data of different wavelength is converted based on $\Omega_B \propto 1/\lambda_P$ and $\tau_B \propto \lambda_P^2$. λ_P, laser wavelength; $\Omega_B/2\pi$, SBS frequency shift; g_B, steady-state gain factor; τ_B, phonon lifetime; $\partial n/\partial T$, thermal induced refractive index change; and α: linear absorption coefficient.

when a low energy collimated beam is propagated through a 2.5 m glass cell filled with FC72 [52]. Both deflection and distortion are caused by the index gradient that is built up along the vertical direction because of the tiny temperature gradient. It will be shown in Section 3.3.1 that the phase aberration associated with the large $\partial n/\partial T$ also severely distorts the far field distribution of SBS compressed beam.

In the case of water, both beam pointing stability and beam quality can be preserved. More interestingly, it has been shown by Abbate *et al.* [65] that the $\partial n/\partial T$ is around zero at the water temperature of 2-4^0C. We will show our effort on operating SBS pulse compression in water at low temperature in Section 3.3.2. It should be pointed out that one drawback of using water as the SBS medium is its relatively large absorption coefficient at the wavelength above 500 nm. The direct impact is the lower energy efficiency in SBS compression when water is employed. However, as we will show below, more than 60% of overall energy efficiency can be achieved in water at 532 nm with the energy-scalable generator-amplifier setup. For the consideration of excellent reliability and reproducibility, water would be the ideal medium for the application of high-energy SBS pulse compression. It is interesting to point out that heavy water might be an even better choice, since it has advantages of zero $\partial n/\partial T$ at 11 ^0C and lower absorption coefficient at 532 nm.

3.2.4 Theoretical modeling

The SBS pulse compression process can be numerically modeled. Xu has studied on the modeling of SBS pulse compression in detail [20]. Since the absorption loss is very low for FC72, which is the major focus of Xu's work, the previous model does not include the linear loss to both pump and Stokes pulses during the process of pulse compression. Instead, a transmission factor is simply applied to the compressed Stokes pulse in order to justify for the actual energy efficiency. In the case of water, which has been mainly focused by this work, the linear loss plays a bigger role in adjusting the intensities of pump and

Stokes pulses, which are critical in defining the compressed Stokes pulse. Therefore, we have modified the previous model to consider the linear loss of both pulses, during their each step of propagation inside the SBS medium.

We have made another improvement to the previous model, which considers that the acoustic phonon at beam focus is fed by random noise. This consideration leads to appropriate pulse compression, but can not address the build-up time of the Stokes pulse correctly. To overcome this issue, the strength of the acoustic wave created at the beam focus needs to be proportional to the intensity of the pump pulse at that point. As will be presented in Section 3.5, reasonable results have bee obtained by utilizing the further developed model for the simulation of spatio-temporal profile of the SBS compressed pulses. Here, we give a brief discussion on the modeling.

$$\frac{\partial \mathcal{E}_1}{\partial t} + c/n\frac{\partial \mathcal{E}_1}{\partial z} = -i\epsilon_0 c^2 g_B \Gamma_B \rho' \mathcal{E}_2 \tag{3.1a}$$

$$\frac{\partial \mathcal{E}_2}{\partial t} - c/n\frac{\partial \mathcal{E}_2}{\partial z} = -i\epsilon_0 c^2 g_B \Gamma_B \rho'^* \mathcal{E}_1 \tag{3.1b}$$

$$\frac{\partial^2 \rho'(z,t)}{\partial t^2} + (\Gamma_B + 2i\Omega_B)\frac{\partial \rho'(z,t)}{\partial t} + i\Omega_B \Gamma_B \rho'(z,t) = -\frac{1}{2}\Omega_B \mathcal{E}_1 \mathcal{E}_2^* \tag{3.1c}$$

As mentioned above, the SBS process is an interaction among three waves, which can be described by three coupled differential equations, as listed in Eqs. 3.1. In those equations, g_B is the steady-state Brillouin gain factor, $\Gamma_B/2\pi$ is the full width at half maximum of the SBS gain spectrum, $\tau_B = 1/\Gamma_B$ is the phonon lifetime, and Ω_B is the Brillouin shift. ρ' is defined as $\rho(z,t) = -(\epsilon_0 \gamma_e q_B^2/\Omega_B)\rho'(z,t)$, where γ_e is the eletrostrictive constant of the SBS medium and q_B is the wave number of acoustic wave. c, n and ϵ_0 are the speed of light in vacuum, the refractive index of SBS medium and the vacuum permittivity, respectively. t is the time axis and z is the spatial axis along the propagation direction of the pump. The value of different parameters used in the simulation for both FC72 and water have been summarized in Table 3.1. The slowly varying envelope approximation is applied to both pump ($\mathcal{E}_1$) and Stokes ($\mathcal{E}_2$) fields. The split-step method is used to numerically solve the

coupled equations.

The model described above is similar to other simulations [43,53,66,67], without considering the transverse dimension. This model has been demonstrated to accurately reproduce the experiment result [52], if only the compression in the beam center is considered. When it is used to predict the spatio-temporal profile of SBS compressed pulses, discrepancy between the experiment and simulation is found. As we will show in Section 3.5, part of the features observed from the experiment can be reproduced. The limitation will be discussed in detail there.

3.3 High-energy SBS pulse compression in FC72 and water[3]

In this section, we will demonstrate the capability of high-energy (Joules level) SBS pulse compression in liquids, by employing the energy-scalable generator-amplifier setup. We will present the results of pulse compression in both FC72 and water. It will be shown that water as combined with the energy-scalable generator-amplifier setup is ideal for high-energy pulse compression.

3.3.1 SBS pulse compression in FC72 at 1064 nm

The high-energy pulse compression is first carried out at 1064 nm. Two cells of the energy-scalable generator-amplifier setup shown in Fig. 3.2(c) are both filled with FC72 as the SBS medium. The length of both cells has been chosen to be 2.5 m, in order to match half of the spatial length ($c\tau_p/n$) of the laser pulse[4], where τ_p represents the FWHM. It will be

[3]Portions of this section have been published in C. Feng *et al.*, Opt. Lett. **39**, 3367-3370 (2014) [51]

[4]The full spatial length of the laser pulse is considered to be $2c\tau_p/n$

demonstrated in Section 3.4 that long enough interaction length is essential for achieving shortest compressed pulse width.

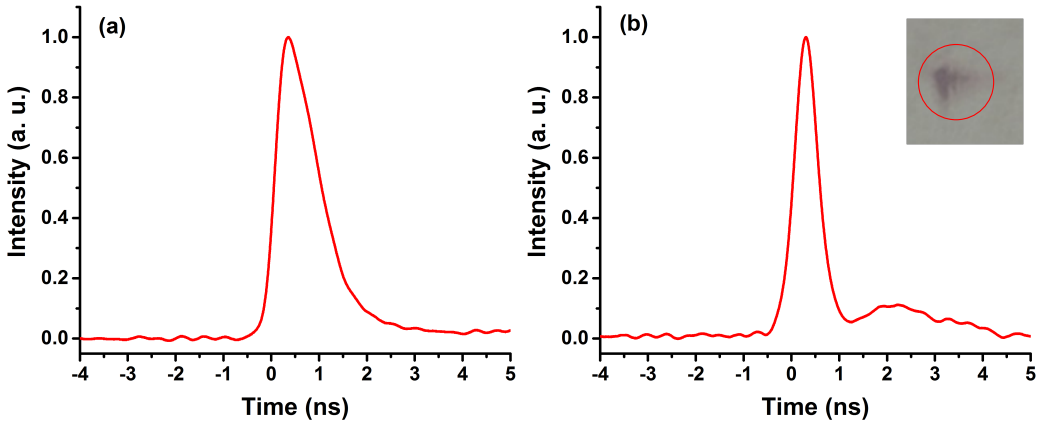

Figure 3.3: SBS compressed pulses from an energy-scalable generator-amplifier setup; (a) Stokes seed pulse; (b) Amplified Stokes pulse; Inset, far field distribution of amplified Stokes beam.

Laser pulses (1 J per pulse, 12 ns FWHM), obtained after the 6^{th} amplifier of Nd:YAG laser system, are used as the input to the SBS compressor. The laser beam is expanded to 20 mm beam diameter (full width at $1/e^2$ maximum intensity) to maximize the energy load capacity. The generator input pulse with 50 mJ energy is employed to create pre-compressed Stokes seed pulse. The remaining portion of the input with 950 mJ energy is used as the pump. An amplified Stokes pulse of 735 mJ is obtained with energy fluctuation of less than 1.3%. The corresponding overall energy efficiency is up to 73.5%. To characterize the compressed pulse, a 25 GHz InGaAs biased photodetector (model: 1417) from Newport combined with an Agilent digital oscilloscope (bandwidth: 2.5 GHz; Sampling rate: 20 Gsa/s) are used. Both Stokes seed and amplified Stokes pulse are presented in Fig. 3.3. The Stokes seed pulse has a duration of 1 ns FWHM, while the amplified Stokes pulse is about 580 ps ($\pm$13 ps) FWHM. Besides the main pulse, a secondary pulse is also shown in the amplified Stokes pulse, which will be investigated in detail in Section 3.4. The inset shown in Fig. 3.3(b) presents the far-field distribution of the amplified Stokes beam,

which exhibits obvious distortion. The phase aberration introduced by the index gradient as discussed earlier is responsible for the distortion. In the application where highest focus intensity is sought, FC72 is disqualified. Then, we are motivated to study the SBS pulse compression in water.

3.3.2 Reliable SBS pulse compression in water at 532 nm

Efforts on minimizing the $\partial n/\partial T$ effect

To overcome the issues in FC72, water is chosen for its low $\partial n/\partial T$ and the possibility of eliminating the effect of $\partial n/\partial T$ at low temperature. For the latter purpose, we have designed special glass cells for cooling down the water. Figure 3.4 shows the two versions that have been experimentally tested. In both designs, the SBS cell has an inner tube that is filled with high purity water (OmniSolv, EMD Milipore) as the SBS medium. It also has an outer mantel that is employed to circulate the cooling liquid, thus behaving like a temperature stabilizer.

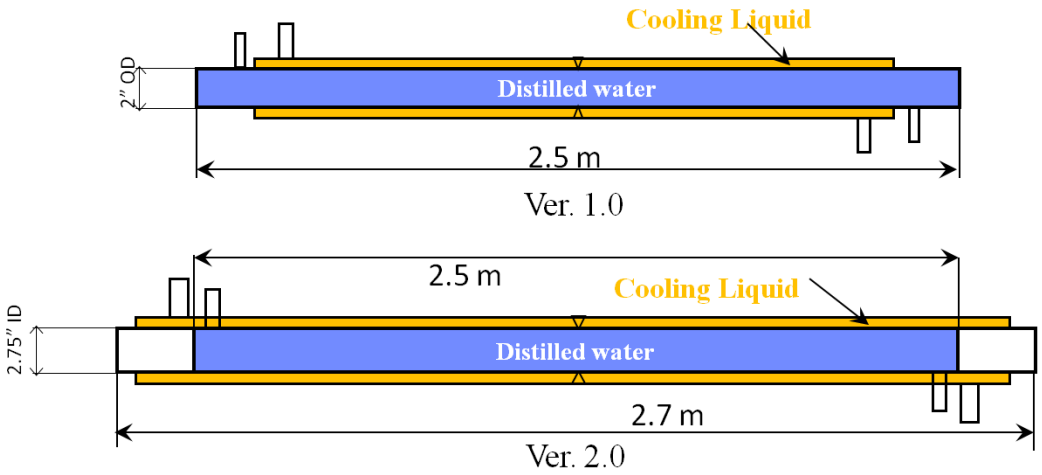

Figure 3.4: Two versions of glass tube design for the purpose of running SBS pulse compression under low water temperture.

The SBS cells are tested in a single-cell pulse compression setup at the wavelength of 532 nm. Laser pulses of 12 mJ are focused into the inner tube with a plano-convex lens of 2.2 m effective focal length in water. The spatial profiles of the generated Stokes seed beam are recorded by a CCD camera, with the results being presented in Fig. 3.5. In the case of 2.2 m focusing lens, the distortion in Stokes beam profile [Fig. 3.5(a)] has been observed immediately for the first design when the cooling temperature is slightly below the room temperature (23 ^0C). With the same cell, the beam distortion has not been observed even at the cooling temperature of 2 ^0C [Fig. 3.5(b)], if a 80 cm lens is used to focus the input beam. As a comparison, the cooling temperature can go down to 14 ^0C for the second cell design with 2.2 m focusing, until the beam distortion starts to appear.

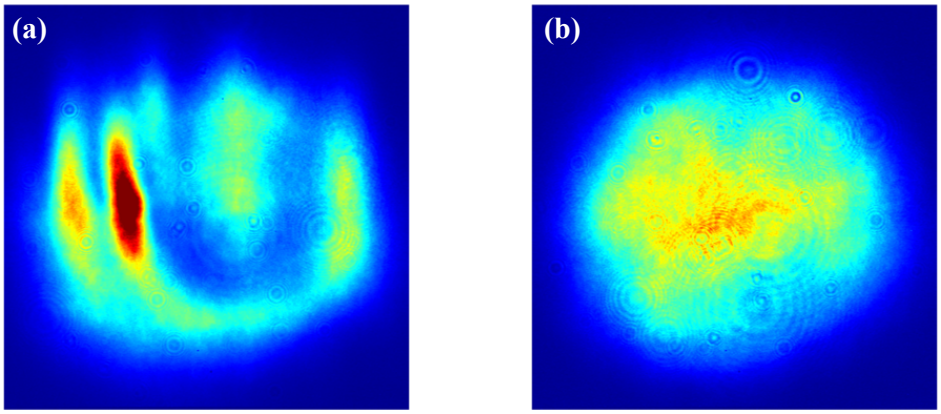

Figure 3.5: Stokes beam profiles obtained with the SBS cell of first design; (a) Input beam is focused close to the end of glass tube by using a 2.2 m focusing lens; (b) Input beam is focused around the middle of glass tube by using a 0.8 m focusing lens.

All the observations mentioned above can be explained by the convection exhibited at both ends of the glass tube, which is created by the temperature gradient along the beam propagation direction. In order to overcome this issue, much longer outer mantel has to be designed to enclose the inner tube. Another solution is to use much more expensive heavy water as the SBS medium, which has negligible $\partial n/\partial T$ around 11 ^0C. In this case, the

constraint on the cell length can be alleviated. For the experiments discussed below, the water temperature is stabilized at 21 ^0C, which is enough for obtaining compressed pulses with high stability and excellent beam quality.

Experimental results

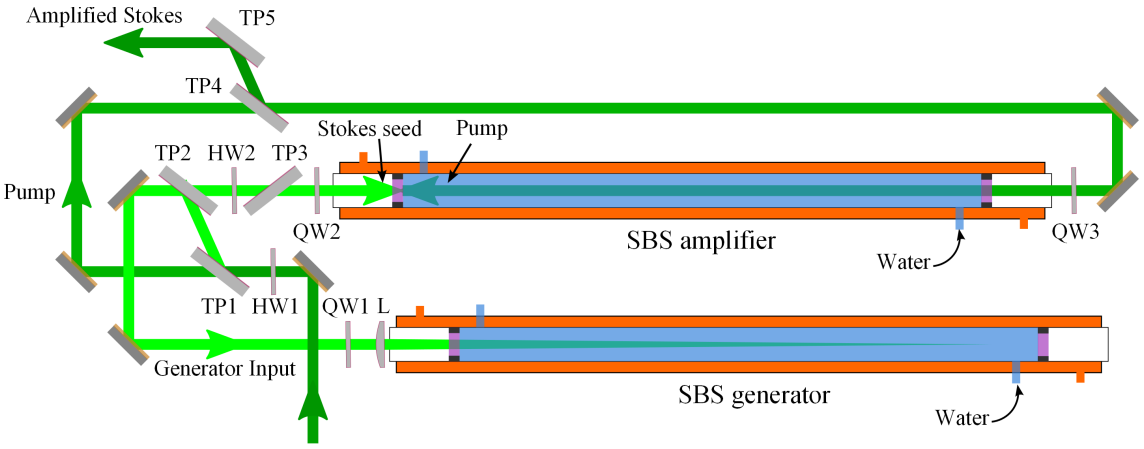

Figure 3.6: Experimental setup employed for SBS pulse compression in water; HW: Half Wave-plate; QW: Quarter Wave-plate; TP: Thin-film Polarizer; L: Lens.

The experimental setup demonstrated in Fig. 3.6 is slightly different from the one displayed earlier in Fig. 3.2(c). Double-walled glass cells are used to stabilize the water temperature at 21 ^0C. An extra half wave-plate (HW2) and a thin-film polarizer (TP3) are added to vary the Stokes seed energy sent into the SBS amplifier, for the purpose of investigating the dependence of energy extraction efficiency inside the amplifier on the Stokes seed intensity. The input laser pulse has maximum duration of 12 ns. The input beam diameter is chosen to be 30 mm (full width at $1/e^2$ maximum intensity), limited by the 2" optics used in the compressor.

Before characterizing the SBS compressor, we have measured the SBS threshold of the amplifier cell, with the experimental setup and the result shown in Figs. 3.7(a) and (b), respectively. We consider the maximum pump energy that can be sent into the amplifier to

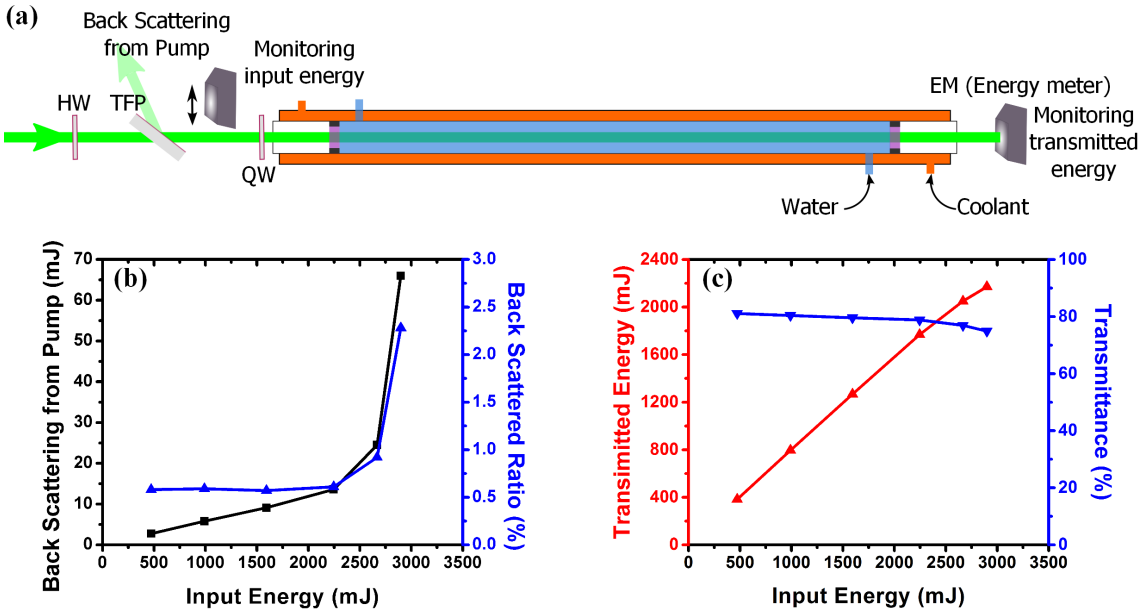

Figure 3.7: (a) Experimental setup for the SBS threshold and transmittance measurements; (b) SBS threshold measurement; (c) Transmittance measurement.

be 2.2 J, above which point the back scattered signal from the pump increases exponentially. With the same setup, we have also measured the transmittance to be around 85%, with the corresponding linear loss coefficient to be $6.5 \cdot 10^{-4}\text{cm}^{-1}$. The measured loss coefficient is slightly larger than the number quoted in Table 3.1 because of the extra scattering losses from different surfaces.

To assess the performance of the setup, we start by characterizing the seed pulse from the generator. As illustrated in Fig. 3.8(a), the energy reflectivity of the generator saturates at about 73%, for an input energy above 90 mJ. We measure the relative energy fluctuation in the generated seed pulse to be around 2%, which matches the amount of fluctuation in the input beam [Fig. 3.8(a) inset]. This observation implies that the SBS process in the generator is extremely stable. The stability is further demonstrated by the small fluctuation in pulse width sampled at beam center[Fig. 3.8(b)], when the input energy exceeds 90 mJ. The relative standard deviation (RSD) of pulse width, measured for 50 laser shots, is $<$5%.

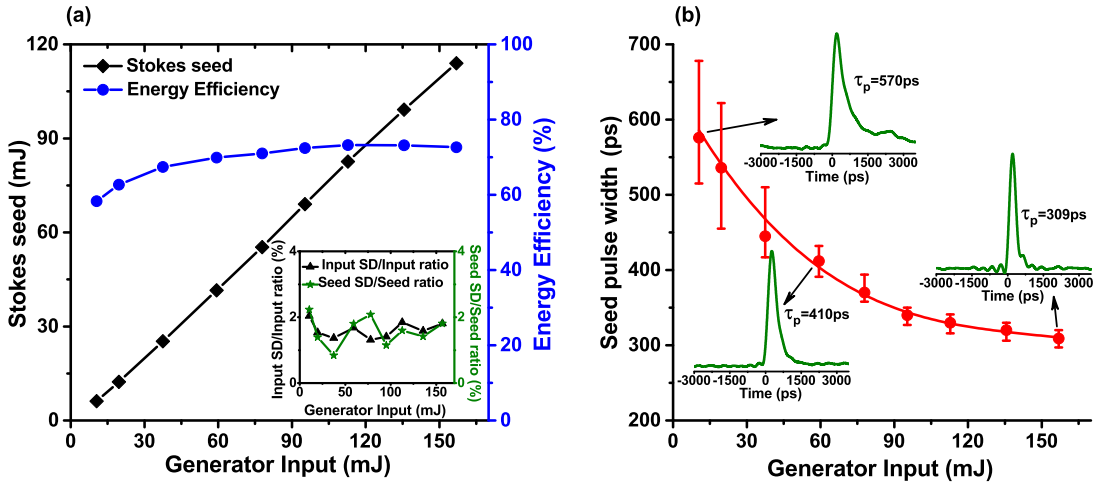

Figure 3.8: (a) Output energy of Stokes seed (solid diamond) and the corresponding energy efficiency (solid circle) with different generator input energy; Inset: Ratio between input standard deviation (SD) and input energy (solid triangle); Ratio between seed standard deviation and Stokes seed energy (solid star); (b) Pulse width evolution of Stokes seed with respect to generator input energy. Solid circles denote measurements of seed pulse width and the solid curve is a fit to the measurements. Error bar shows the maximum deviation of pulse width from the mean value. Three insets show typical compressed pulse shapes for corresponding input energy.

We achieve a minimum compressed pulse width of 309 ps at the highest input energy of 160 mJ. The pulse detection setup used here is the combination of a Hamamatsu R1328U-52 biplanar phototube (rise time: 60 ps; spectral response: 185-650 nm; detection area: 10 mm diameter) and an Agilent DSO90254A digital oscilloscope (Bandwidth: 2.5 GHz; Sampling rate: 20 Gsa/s). Due to the limited time resolution of the latter, pulses shorter than 400 ps can not be accurately characterized, as demonstrated by the wiggles in the pulse leading/trailing edge. For the consideration of very stable SBS pulse compression, an input energy of 120 mJ, which produces seed pulses of 90 mJ and 325 ps from the generator, is chosen for subsequent compression experiments.

The seed pulse enters the amplifier cell and interacts with the pump pulse, which is chosen to have 2.2 J energy per pulse, the threshold value as claimed above. To determine

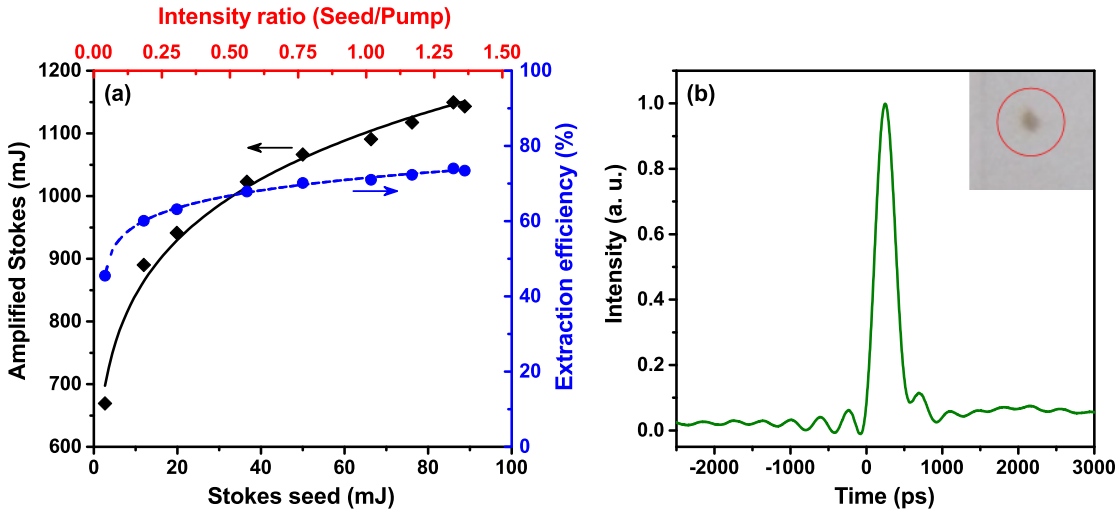

Figure 3.9: (a) Amplified Stokes energy and extraction efficiency for the SBS amplification process. Solid diamonds denote measured output energy; Solid circles denote extraction efficiency. The solid and dashed curves are a fit to the data. The energy of the input pump pulse is fixed at 2.2 J. (b) The typical 300 ps amplified Stokes pulse sampled at the beam center with an output energy of ∼1.2 J. The inset shows the far field distribution of Amplified stokes beam at maximum energy.

the minimum seed energy required to extract a pump energy of 2.2 J, we vary the input seed energy by HW2 plus TP3 and monitor the output (amplified Stokes pulse). As shown in Fig. 3.9(a), the maximum extracted energy is close to 1.2 J, with only 2% energy fluctuations (not shown in the figure). The total losses L (sum of water absorption and loss from optics) of the amplification process is measured by subtracting from the total input energies (pump E_p and seed E_s) the sum of the transmitted (depleted) pump E_d and the amplified Stokes pulse E_{AS}. The SBS energy extraction efficiency, plotted in Fig. 3.9(a), is defined as η_{ex}=$E_{AS}/(E_p + E_s - L)$. The maximum of 75% extraction efficiency is comparable to the value found in the literature [54]. Both extracted energy and extraction efficiency start to saturate at a seed energy of 90 mJ. At this point, the peak intensity of the seed pulse (due to compression in the generator cell) matches that of the uncompressed pump pulse, leading to most efficient non-linear interactions [52].

The typical amplified Stokes pulse sampled at the beam center with pulse duration of 300 ps at maximum output energy is shown in Fig. 3.9(b). The pulse width fluctuation of the amplified Stokes pulse is similar to that of the Stokes seed pulse. The possible origin of the pulse width fluctuation has been explained in a previous work [67]. As a comparison with the pulse compression in FC72, the far field distribution of amplified stokes beam at full energy is also displayed in the inset of Fig. 3.9(b). It is obvious that the focusing ability of the compressed pulse obtained here is much better.

To summarize this section, we have demonstrated high-energy SBS pulse compression in water, by employing the energy-scalable generator-amplifier setup. The maximum compressible energy of the current setup is up to 2.4 J, which can be further increased by utilizing larger optics. A maximum of 40 fold compression, from 12 ns to 300 ps (close to the phonon lifetime of 295 ns of water at 532 nm) has been achieved near the beam center. In the next section, we will present our further study on high-energy pulse compression below the phonon lifetime.

3.4 High-energy sub-phonon lifetime SBS pulse compression[5]

3.4.1 Background

In SBS pulse compression, the shortest compressed pulses are always desired for achieving the highest peak power. However, the minimum pulse duration that can be achieved via SBS pulse compression is still under debate. The phonon lifetime of SBS medium has been considered as the lower limit of compressed pulse duration by some of the studies [46, 48, 54]. For some other works [42, 44, 45, 57, 58], pulse compression below the

[5]Portions of this section have been summarized in C. Feng *et al.*, "High-energy sub-phonon lifetime pulse compression based on stimulated Brillouin scattering in liquids" (To be submitted) [68]

phonon lifetime has been experimentally observed, but without physical explanation. In most cases, short and clean (i.e., without exhibiting long tail or trailing edge modulation) compressed pulses have only been obtained by employing either double-stage compression or a cascaded generator-amplifier setup. The idea of double-stage compression is to pre-compress the input pulse in a single-cell setup, then have another compression of the pre-compressed pulse either in the same or a second single-cell setup.

For pulse compression in a single-cell setup, Gorbunov *et al.* [57] have successfully achieved sub-phonon lifetime pulse compression in simulation of square input pulses, but experimentally failed in demonstrating with Gaussian-shaped input pulses. It is found that the compression ratio is sensitive to the focusing angle of the pump beam. To scale up the compressible energy, it has been concluded that the focusing angle has to be increased by shortening the focal length. Our investigation presented below draws the opposite conclusion that long focal length is essential for obtaining the compressed pulse duration below the phonon lifetime.

Recently, two more papers [49, 53] have reported sub-phonon lifetime SBS pulse compression with Gaussian input pulses. Velchev *et al.* [53] have tried to address the limiting factors on sub-phonon lifetime compression. They have concluded that, for pulses much longer than the phonon lifetime, the minimum compressed pulse width is limited by the lifetime of acoustic phonon. As we will demonstrate later, no matter what is the length of the input pulse, sub-phonon lifetime compression is readily achievable in a single-cell setup as long as the interaction length is long enough to match half of the pulse length. In [49], sub-phonon lifetime compression has been experimentally demonstrated with a cascaded generator-amplifier setup. In order to compress the pulses below phonon lifetime, the focal length inside the generator has to be increased from 300 mm to 1000 mm, which is against the design principle of such setup. With long focal length, high-energy pulse compression with acceptable stability becomes impossible.

3.4.2 Analysis

Generally, laser pulses with Gaussian temporal shape are employed for SBS pulse compression. In a single-cell setup, the interaction length has been commonly chosen as $c\tau_p/2n$, in which case the Stokes pulse is considered to be initiated from the first half maximum intensity point on the pulse leading edge and the pulse compression finishes at the second half maximum intensity point. The remaining pump pulse keeps propagating into the cell and interacting with the acoustic phonon that is fixed near the window. In this case, the density grating behaves like a static mirror, which simply converts the long tail of the pump pulse into a long tail for the Stokes pulse [42].

It is obvious that the above situation only applies for one specific input energy. As the input energy increases, the portion within the pump pulse involved in the pulse compression shifts towards the pump pulse leading edge. The remaining part of the pump pulse now has higher intensity, which makes it hard for the fixed acoustic phonon to completely convert the remaining pump into Stokes. The consequence is that part of the remaining pump will propagate to the beam focus region to form one or a sequence of Stokes pulses that are well separated in time [69]. In either case, i.e., the presence of long trail or multiple Stokes pulses, the main Stokes pulse has not been well compressed, simply because the pump pulse has not been fully employed for the pulse compression. A longer interaction length of $c\tau_p/n$ to fully cover the pump length for SBS interaction is expected to overcome this issue and lead to shorter compressed pulses.

It is widely accepted that the SBS compressed pulses exhibit a sharp leading edge and a relatively slow trailing edge. An even shorter compressed pulse would be obtained if the trailing edge could also be sharpened. An early study reported by Damzen *et al.* [43] has actually pointed out the way by having energy exchange between the trailing edge of the pump pulse and the Stokes pulse, under the strong interaction condition. Even though it has been believed as a negative effect for pulse compression because of the presence of multiple

pulses, we will demonstrate that, by controlling the pump intensity, the energy exchange mechanism helps obtaining very clean compressed pulses with sharp trailing edge. The compressed pulse duration can be below the phonon lifetime readily from a single-cell compression setup.

3.4.3 Sub-phonon lifetime compression in a single-cell setup: experiments

To confirm the above analysis, we have performed pulse compression experiments in a single-cell with 2.5 m length. Pulse compression in FC72 at 1064 nm and in water at 532 nm are tested, demonstrating that sub-phonon lifetime compression can be achieved in different SBS medium at different wavelength. Since the pump beam has spatial intensity distribution and the compression ratio is strongly intensity dependent, the results presented below represent the best pulse compression around the beam center unless specified otherwise.

Sub-phonon lifetime compression in FC72 at 1064 nm

In the case of FC72, two lenses with focal length of 100 cm and 200 cm have been used to approximately match $c\tau_p/2n$ and $c\tau_p/n$ of 9 ns input pulses, respectively. The input beam size is fixed at 20 mm diameter (full width at 1/e^2 maximum intensity). The compressed pulses are characterized by a 25 GHz InGaAs biased photodetector (model: 1417) from Newport combined with an Agilent digital oscilloscope (bandwidth: 2.5 GHz; Sampling rate: 20 Gsa/s).

The dependence of the compressed pulse duration on both focal length and pump energy are demonstrated in Fig. 3.10(a). The dash line representing the phonon lifetime of FC72 at 1064 nm is calculated from $1/2\pi\delta\upsilon_B$ to be 590 ps, with Brillouin bandwidth $\delta\upsilon_B$ of

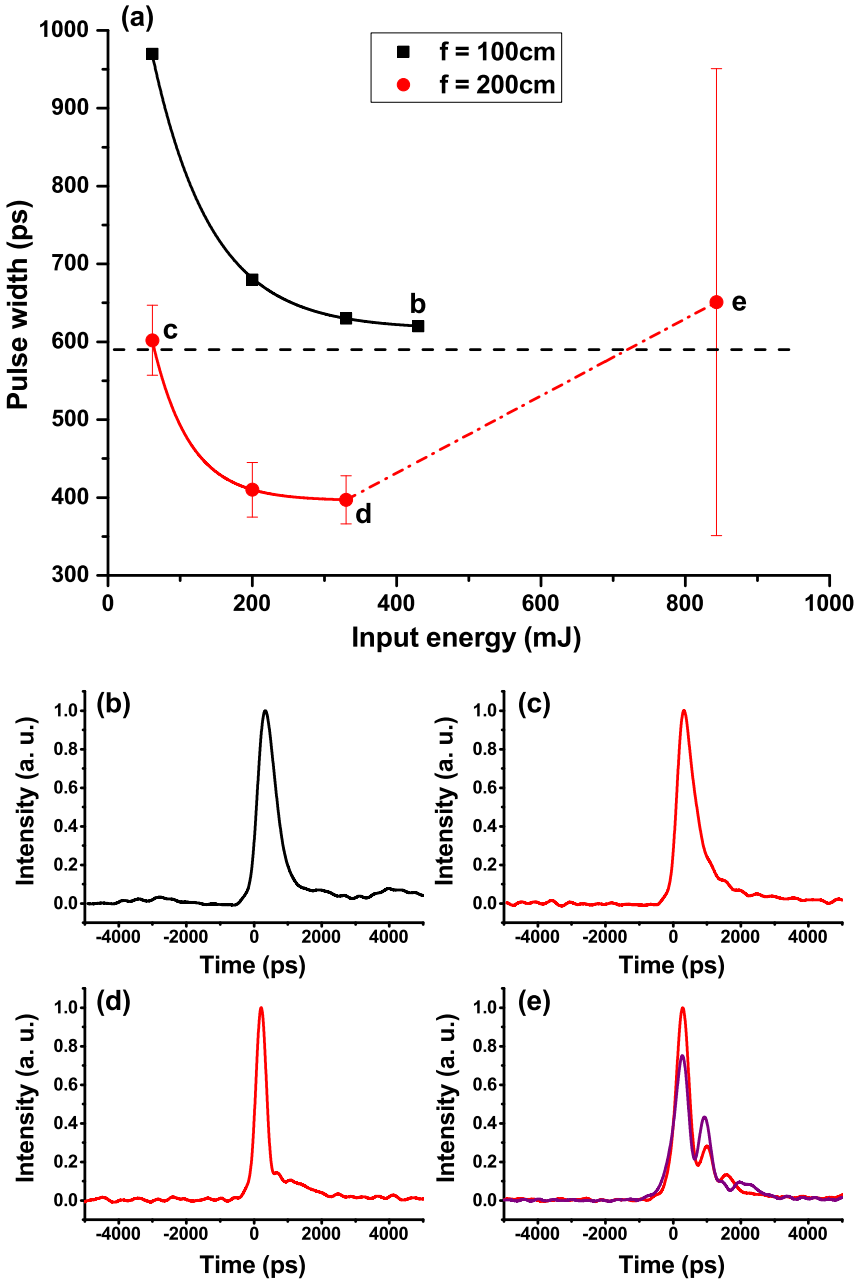

Figure 3.10: (a) Experimentally measured dependence of compressed pulse duration on the input energy, with the focal length of 100 cm and 200 cm being, respectively, used; (b)-(d) Compressed pulse shapes with different initial conditions.

270 MHz from [61]. The difference in pulse compression with two focal length lenses is clearly shown. The compressed pulse duration has been limited to the phonon lifetime when the focal length only matches to $c\tau_p/2n$. This observation is similar to the result reported in [53]. However, with a long focal length that matches to $c\tau_p/n$ being used, sub-phonon lifetime compression has readily been achieved, even with relatively low pump energy. This observation disproves the conclusion drawn from the previous work [53] that the compressed pulse width is limited to the phonon lifetime if the pump duration is much longer than the phonon lifetime.

It is helpful to understand the sub-phonon lifetime compression by checking the compressed pulses obtained with different initial conditions, as shown in Figs. 3.10(b)-(e). The shortest compressed pulse obtained with 100 cm focal length at the pump energy of more than 400 mJ exhibits the typical feature of SBS compressed pulse, i.e., with sharp leading edge and relatively slow trailing edge. However, to achieve similar compressed pulse duration, it requires much less input energy in the case of a 200 cm interaction length being used. The compressed pulse [Fig. 3.2(c)] is also free of modulation as compared to the one [Fig. 3.2(b)] obtained with 100 cm focal length.

As the input energy increases, the trailing edge becomes sharper that further shortens the compressed the pulse below the phonon lifetiem. Figure 3.2(d) represents the shortest pulse of less than 400 ps at the compressible energy of more than 300 mJ. At very high input energy, the pulse compression becomes very unstable, which is manifested by the large error bar. Strong modulation on the Stokes pulse, as demonstrated by the two typical pulses in Fig. 3.2(e), has been observed.

Sub-phonon lifetime compression in water at 532 nm

Instead of repeating the above experiments in water at 532 nm, we choose to fix the focal length at 220 cm and investigate the dependence of pulse compression on input pulse du-

ration. The results obtained from this experiment can be used to compare with the results reported in [53]. To characterize the short pulses (<295 ps) with relatively good accuracy, a Hamamatsu R1328U-52 biplanar phototube (rise time: 60 ps; spectral response: 185-650 nm; detection area: 10 mm diameter) and a Tektronix DPO 70804 digital phosphor oscilloscope (Bandwidth: 8 GHz; Sampling rate: 25 Gsa/s) are used.

The pulse compression is assessed by characterizing the dependence of compressed pulse duration and energy efficiency on the input energy, as presented in Fig. 3.11. Laser pulses with pulse duration of 7 ns and 9 ns are employed for the compression. It can be seen that the compression ratio is larger for shorter input pulses, which is in agreement with the simulation results reported in [53]. Our simulation, as will be presented below, also confirms this observation.

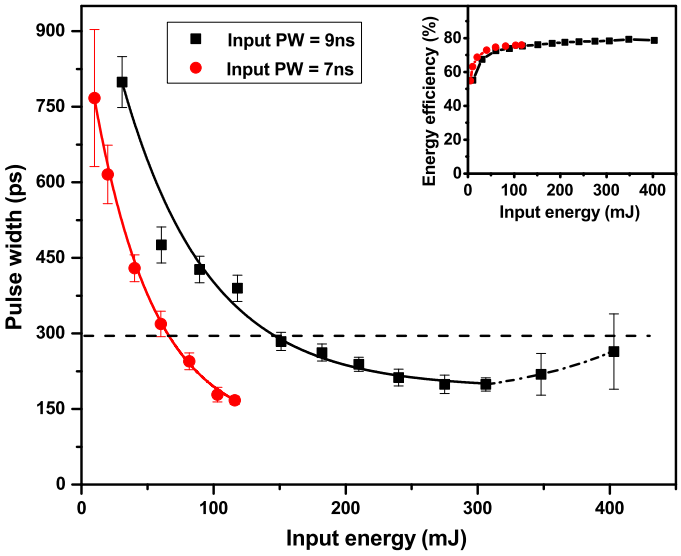

Figure 3.11: Experimentally measured dependence of compressed pulse duration on the input pulse energy at a fixed focal length of 220 cm, with input pulse duration of 7 ns and 9 ns, respectively; The inset shows the corresponding energy efficiency for the two input pulse duration cases.

When 7 ns input pulses are used, sub-phonon lifetime pulse compression has been

achieved with the input energy above 60 mJ. As it has been mentioned in Chapter 2, the Nd:YAG laser pulse width is proportional to the output energy, because of the gain saturation effect inside the laser amplifiers. Pulses with 7 ns duration at 532 nm can be obtained with the maximum output energy of 120 mJ, at which input energy the compressed pulse width is as short as 150 ps. The energy efficiency, as shown in the inset of Fig. 3.13, reaches more than 75%. Therefore, the compressed pulses of 150 ps with 90 mJ per pulse have been obtained. The saturation in pulse compression would be expected if higher input energy was used.

For 9 ns input pulses, sub-phonon lifetime pulse compression has been achieved when the input pulse energy goes beyond 150 mJ. The compressed pulses of 240 mJ with minimum duration of 190 ps are obtained at the input energy of 300 mJ. As the input energy further increases, both increased pulse width and larger fluctuation are observed. It is worth noticing that SRS is found to appear randomly at the input energy of more than 350 mJ, which is considered as one of the reasons to cause pulse fluctuation. The compressed pulse shapes at different input energies have also been reviewed for the case of 9 ns input pulses. Similar behavior, as reported in Figs. 3.10(c)-(e), has been observed.

3.4.4 Sub-phonon lifetime compression in a single-cell setup: numerical simulations

To understand the mechanism behind sub-phonon lifetime compression, simulations on single-cell pulse compression have been carried out, using the optimized model described in Section 3.2.4. The results presented below represent the pulse compression in water, which is preferred for high-energy application.

In order to compare with the experimental results as discussed above, the input pulse parameters to the simulation are chosen to match those from experiment. Specifically, the pulse has Gaussian temporal shape with duration of 9 ns (FWHM), and the beam size is

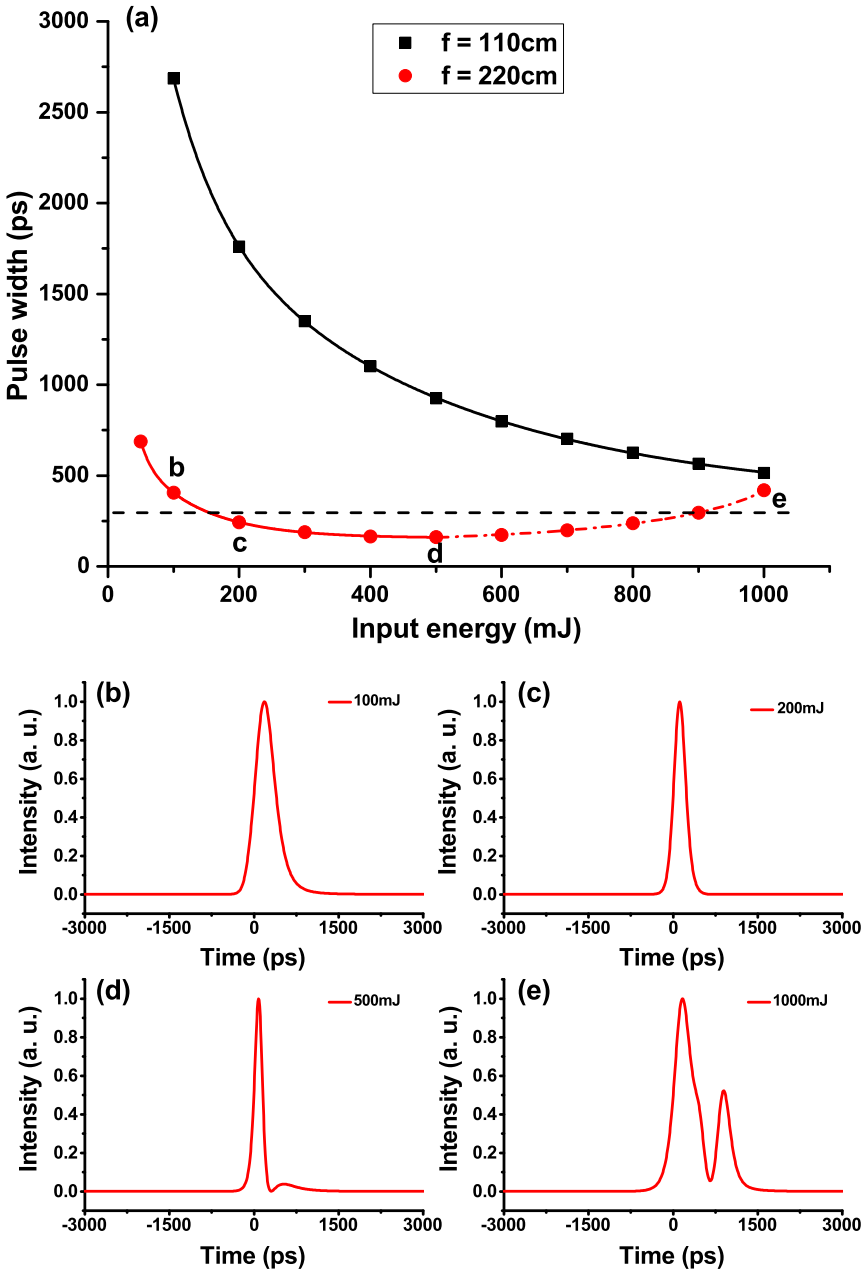

Figure 3.12: (a) Simulated dependence of compressed pulse duration on the input energy, with the focal length of 110 cm and 220 cm being, respectively, used; (b)-(d) Compressed pulse shapes with different initial conditions.

30 mm at full width of $1/e^2$ maximum intensity. We first check the effect of interaction length on the pulse compression. Two different interaction length of 110 cm and 220 cm have been chosen to match $c\tau_p/2n$ and $c\tau_p/n$, respectively.

Figure 3.12(a) illustrates the dependence of compressed pulse duration on the input energy, which is quite similar as the one observed from pulse compression in FC72. When an interaction length of 110 cm is used, the compressed pulse width with input energy up to 1000 mJ is always longer than the 295 ps phonon lifetime of water at 532 nm, which is represented by the horizontal dashed line shown in the same figure. This further confirms that a short interaction length applies limitation on the duration of the compressed pulses.

In the case of 220 cm interaction length, sub-phonon liftime pulse compression can be achieved above certain pump energy. The compressed pulse shapes at four different input energies are displayed in Figs. 3.12(b)-(e). The transition behavior in pulse shape is qualitatively in agreement with that reported in Figs. 3.10(c)-(e). Specially, the shortest pulse obtained at the input energy of 500 mJ exhibits a small pulse resurgence. It qualitatively matches the pulse shape shown in Fig. 3.10(d), in which the sharp trailing edge is followed by a slow decaying tail. It is found that the change in both pulse shape and duration during the transition is more related to the change of pulse trailing edge, which is sharpened by transferring its energy back to the pump. As the input energy further increases, the second pulse becomes stronger, and more importantly, the trailing edge of the first pulse is also found to get less sharp, which thus leads to a longer pulse.

In the early study, Damzen *et al.* [43] have well explained the mechanism of energy exchange between the pump and Stokes pulse, and considered the energy exchange as a negative effect in creating multiple pulses. However, by finely tuning the pump intensity (i.e., either adjust the pump energy or the beam size while satisfying the interaction length requirement), the energy exchange mechanism can be well employed for achieving sub-phonon lifetime compression.

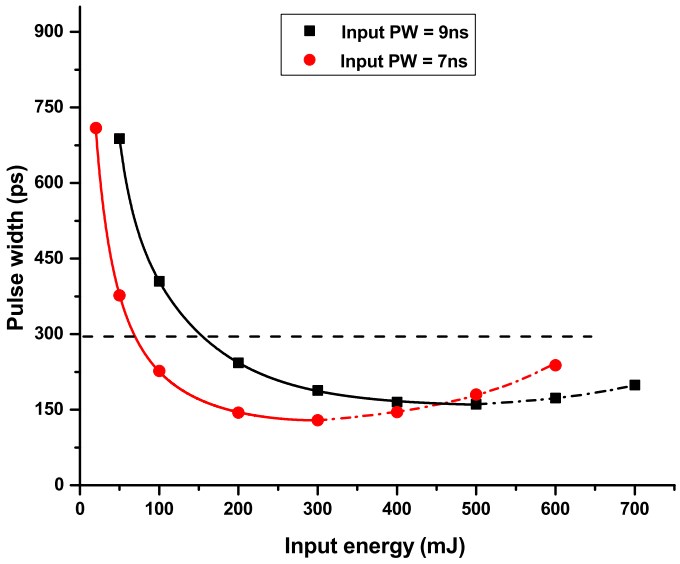

Figure 3.13: Simulated dependence of compressed pulse duration on the input energy at a fixed focal length of 220 cm, with input pulse duration of 7 ns and 9 ns being, respectively, used.

Another interest in simulation is to tune the input pulse width while fixing the interaction length. Figure 3.13 presents the results with the interaction length fixed at 220 cm. Again, the simulations reproduce the experimental results as demonstrated in Fig. 3.13 very well. It is necessary to point out that, as the compressed pulse gets shorter, it gets easier to trigger the generation of SRS, which would ruin the pulse compression stability. Therefore, the energy carried by shorter compressed pulses has to be reduced, because of the intensity limitation imposed by other nonlinear effects.

Based on both experimental and simulation results presented above, we draw a recipe for preparing sub-phonon lifetime SBS pulse compression in a single-cell setup. First of all, one needs to choose an interaction length of $c\tau_p/n$ to balance the compression ratio and linear absorption loss. Next, the optimum pump intensity to achieve shortest compressed pulse can be found by scanning either pump energy or beam size. It is important to note that the pump energy to achieve optimum pulse compression can be scaled up by increas-

ing the beam size thereby keeping the pump intensity constant. Last, shorter input pulses are desired to obtain shorter compressed pulses, if high-energy output is not the primary interest.

3.4.5 Sub-phonon lifetime compression in generator-amplifier setup: experiments

Our goal is to obtain compressed pulses with Joule level energy. Therefore, the energy-scalable generator-amplifier setup sketched in Fig. 3.6 has been employed again to scale up the energy of the pre-compressed pulses from a single-cell setup (genertor). In this case, the total input energy is kept at 2 J to the SBS compressor, and the input energy to the generator is scanned.

Even though SBS pulse compression in amplifier is much more straightforward as compared to the case of generator pulse compression, since it only involves collimated beams, the nonlinear competing effect such as SRS is still the most concern for the case of very high energy compression. The generation of SRS inside the amplifier is found when the input energy to SBS generator is beyond 250 mJ, even though no SRS generation has been noticed from the generator. Due to such reason, the maximum input energy to the generator has been limited to 240 mJ for the following experiment.

Here, we show the results of spatial distribution of the compressed pulse width, as well as compressed pulse shapes that are quantified by the pulse detection setup presented in Fig. 2.4(a). Further detailed discussion on the spatio-temporal profiles of the SBS compressed pulses will be presented in Section 3.5.

Figures 3.14(a), (c) and (e) display the spatial pulse width distributions of both Stokes seed (black solid square) and Amplified Stokes pulses (red solid circle), at the generator input energy of 120 mJ, 180 mJ and 240 mJ, respectively. The pulse compression effi-

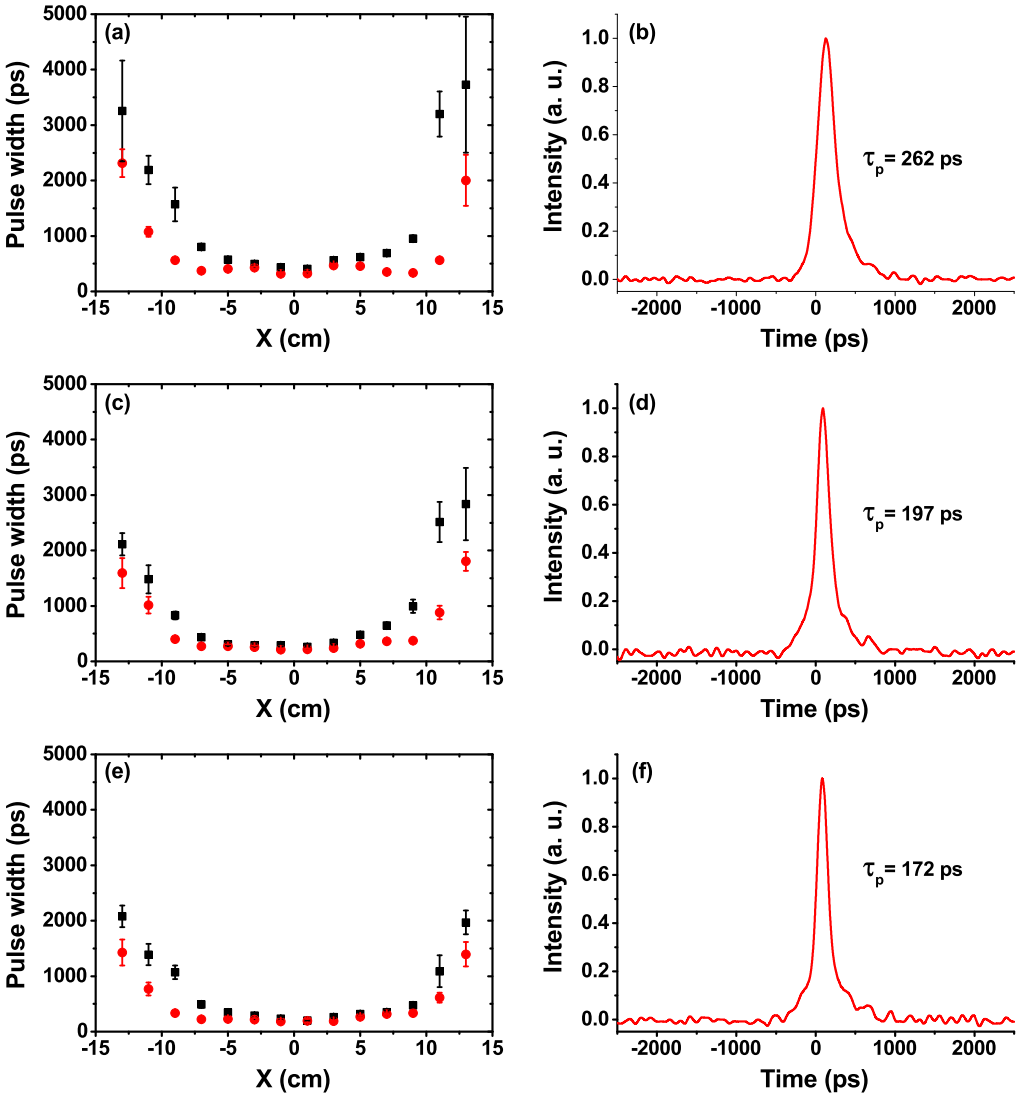

Figure 3.14: (a), (c) and (e) Experimentally measured spatial pulse width distributions of both Stokes seed (Black solid square) and Amplified Stokes pulses (Red solid circle) at three generator input energies of 120 mJ, 180 mJ and 240 mJ, respectively; (b), (d) and (f) Typical amplified Stokes pulse shapes representing the best compression around beam center at three corresponding generator input energies.

ciency (i.e., both compression ratio and stability) is found to be gradually enhanced for both Stokes seed and Amplified pulses across the beam cross section as the input energy to SBS generator is increased.

The typical Amplified Stokes pulse shapes representing the best compression around beam center are also demonstrated in Figs. 3.14(b), (d) and (f), with correspondence to the three generator input energies, respectively. The shortest pulse obtained at the generator input energy of 240 mJ reaches 170 ps and is still free of modulation. The latter is considered as a limit to the maximum generator input energy being used. The minimum relative standard deviation (RSD) of pulse width fluctuation is found to be below 5%. With higher generator input energy, the random generation of SRS causes larger fluctuation of compressed pulses.

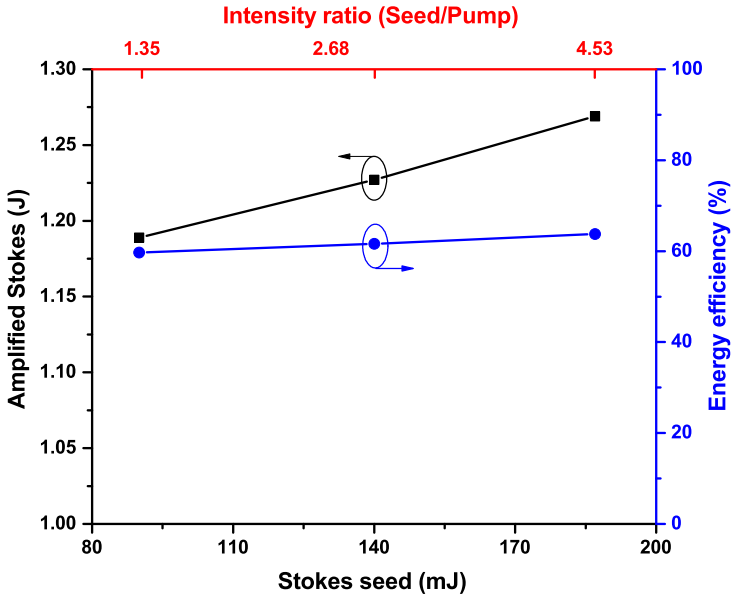

Figure 3.15: Experimentally measured pulse energy of the Amplified Stokes pulse and the corresponding energy efficiency.

The ultimate output energy together with the overall energy efficiency of the SBS compressor are also characterized for three different generator input energies, and illustrated in Fig. 3.15. The maximum energy obtained is close to 1.3 J with the energy stability of less than 1.5% (not shown here). The corresponding overall efficiency is up to 64%. It has been demonstrated in [52] that the energy efficiency starts to saturate once the intensity ratio between Stokes seed and pump pulse exceeds one. The current observation is consistent with

the previous conclusion.

3.5 Spatio-temporal characteristics of SBS compressed pulses

In this section, we focus on exploring the spatio-temporal profiles of the SBS compressed pulses. The spatio-temporal profile of the input green pulse with 2 J energy to the compressor has been shown in Fig. 2.9(b). We use the case of 120 mJ generator input energy

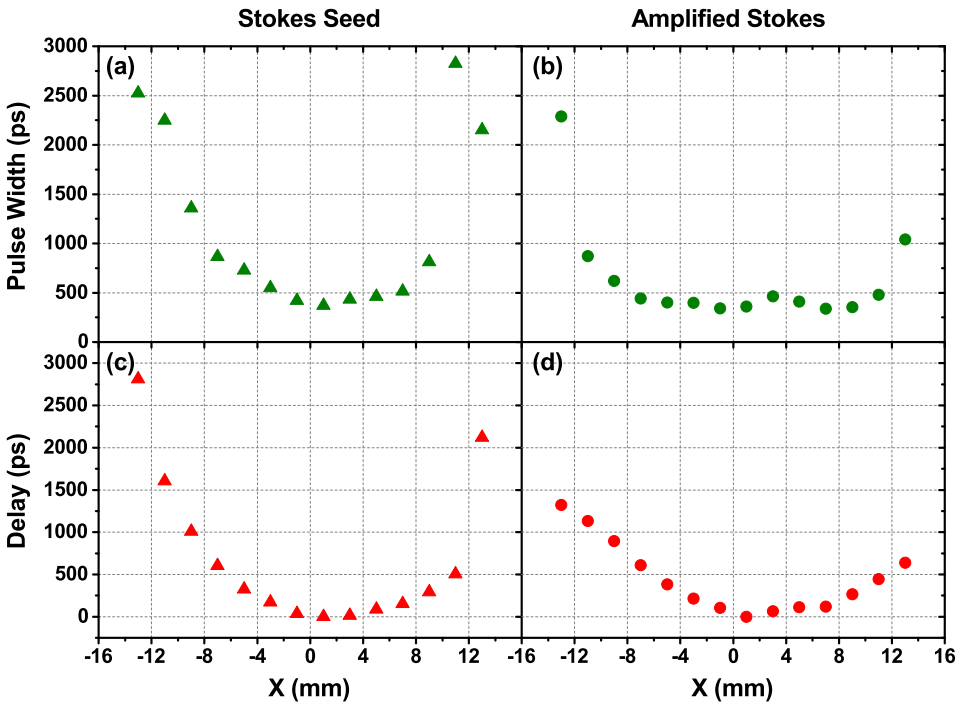

Figure 3.16: Measured spatio-temporal profiles of the SBS compressed pulses; Left: Stokes seed from SBS generator; Right: Amplified Stokes pulse from SBS amplifier; Both Stokes seed and Amplified Stokes are characterized at position C indicated in Fig. 2.1. The pump beam is blocked at a position between TP1 and TP4 [Fig. 2.1] while measuring the spatio-temporal profile of Stokes seed.

as an example to perform the comparison between experiment and simulation.

The spatio-temporal profiles of both Stokes seed and amplified Stokes pulses are experimentally characterized and displayed in Fig. 3.16. Since the SBS pulse compression is a nonlinear process that is intensity dependent, the compressed pulses exhibit shorter pulse width around the beam center and longer pulse width close to the beam edge [Fig. 3.16(a)], because of the intensity distribution of input beam [48, 51]. Very interestingly, the maximum pulse delay existing for the Stokes seed pulse is also compressed from 6$\sim$7 ns [Fig. 2.9(b)] down to 2$\sim$3 ns [Fig. 3.16(c)], which is comparable to the maximum pulse width. The pulse width and pulse delay are further compressed after the SBS amplification process, as demonstrated in Figs. 3.16(b) and (d).

Besides the experimental characterization, we also carry out the simulation by using the numerical model described in Section 3.2.4. The simulation is made under a geometrical optics approximation, in which the pulse propagation, generation and amplification of a Brillouin component is computed along non-interacting rays. The origin of each ray is taken from a Gaussian or super-Gaussian intensity profile on a collimated beam. At each point of the original profile, the experimentally measured pulse temporal profile is used, with the pulse width and pulse delay shown in Fig. 2.9(b).

Figure 3.17 illustrates the simulated spatio-temporal profiles of the compressed pulses. The pulse width distribution of the Stokes seed [Fig. 3.17(a)], has a parabolic shape that qualitatively reproduces that observed in the experiment. Quantitatively however, the simulation shows larger pulse delays on the edge of the Stokes beam [Fig. 3.17(c)] as compared to those of the input pulse. This discrepancy with the experimental observation is a result of ignoring the coupling between inner and outer regions near the beam focus, around which place the Stokes seed is initiated. In the SBS generator, a background field at the Stokes frequency of 10^{-6} of the pump field seeds the Brillouin backscattering. This initial Stokes field is smaller for the rays of the beam edges, resulting in a larger delay of the Brillouin stimulated backscattering. The approach exploited in the current simulation fails to

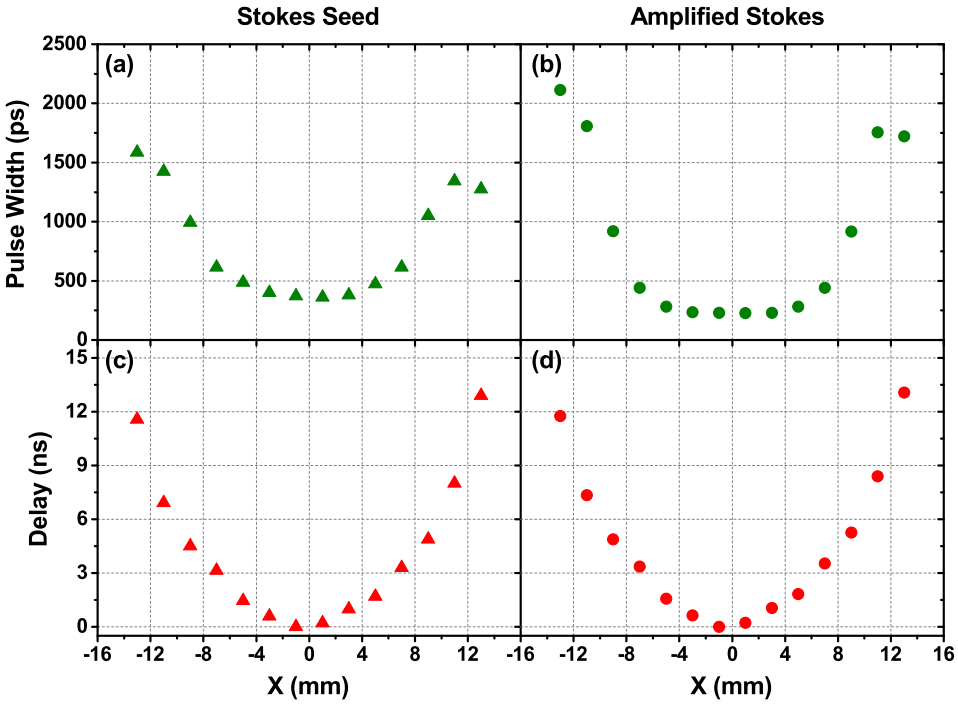

Figure 3.17: Simulated spatio-temporal profiles of the SBS compressed pulses; Left: Stokes seed from SBS generator; Right: Amplified Stokes pulse from SBS amplifier.

account for the contribution of the more intense central ray to the seeding of the marginal rays, which should be the key factor to shorten the pulse delay observed in the experiment. In addition, the spherical aberration from the focusing lens might also play a role in the reduction of pulse delay.

The simulated pulse width distribution of the amplified Stokes [Fig. 3.17(b)] shows similar feature as the experimental observation, where the pulses located around the beam center are further compressed. The lengthened pulse width at the beam edge is attributed to the incomplete interaction because of the low intensity, as well as the inappropriate delay between the Stokes seed and pump pulse. The simulated pulse delay distribution for the amplified Stokes [Fig. 3.17(d)] almost reproduces that of the simulated Stokes seed. It is worth noticing that the Stokes seed and pump are both collimated beams inside the

SBS amplifier. Therefore, no extra delay, as the one observed from the SBS generator simulation, has been introduced to the amplified Stokes in the current simulation. However, the simulation still does not catch the delay compression, as observed for the amplified Stokes in the experiment, due to the same reason that we are not considering interaction in the transverse direction.

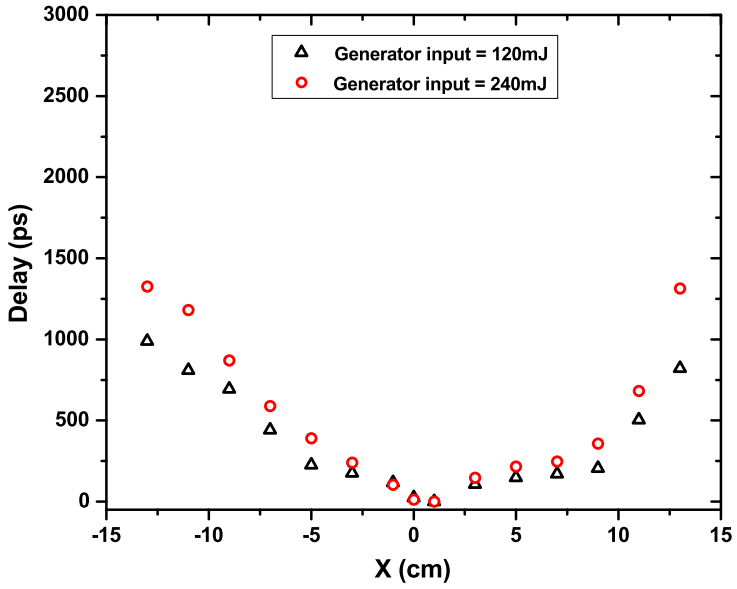

Figure 3.18: Experimentally measured spatial delay distributions of the amplified Stokes pulses for the cases of 120 mJ and 240 mJ generator input energies being applied

Based on the above discussion, the delay between the edge pulse and center pulse would be increased if higher input energy to the generator was used. This prediction has been confirmed by the experimentally measured spatial delay distributions of the amplified Stokes pulses. As demonstrated in Fig. 3.18, the spatial delay is larger, when 240 mJ pulses are used for the SBS generator, in compared to the case of 120 mJ generator input energy being applied.

3.6 High-energy sub-nanosecond UV pulse generation

After having achieved high-energy as well as reliable generation of sub-nanosecond laser pulses at 532 nm, it is straightforward to obtain sub-nanosecond UV pulses via another second harmonic generation. Among different nonlinear crystals, BBO and KDP are the most appropriate ones to convert 532 nm laser beam into 266 nm. BBO crystal has relatively large nonlinear coefficient d_{eff} of 1.75 pm/V for the type I phase matching. Therefore, it is often used for the frequency doubling of either CW or low energy pulsed laser to achieve high conversion efficiency. For the case of high energy application, two photon absorption has often been observed at relatively high UV intensity to reduce the conversion efficiency. This issue could in principle be resolved by using a crystal with large aperture size. However, the very large size BBO crystal with good quality is still not available. In our case, two photon absorption has been observed even a BBO crystal with a dimension of $W16 \times H16 \times L7$ mm^3 being used. Another shortcoming of using BBO crystal is its very small acceptance angle of 0.37 mrad· cm, which makes it to be very sensitive to the alignment and the divergence of input laser beam.

The KDP crystal can be grown with much larger aperture size. It also has acceptance angle in the Type I phase matching of almost 7 times larger than that of the BBO crystal. It is therefore a better choice for our application, even though its nonlinear coefficient d_{eff} of 0.463 pm/V is relatively small. To achieve optimum conversion, the crystal length is first predicted by using the SNLO program. The input parameters (i.e., beam size and super-Gaussian order) to the simulation are taken from experiment. An average input pulse width of 500 ps is used since the spatial pulse width distribution can not be simulated by the program. Based on the above considerations, a crystal length of 10 mm is found to be the optimum. The aperture size of 50×50 mm^2 is chosen to accommodate the green beam size of 30 mm (full width at 1/e^2 maximum intensity).

It has been demonstrated in Section 3.4.3 that both compression ratio and output energy

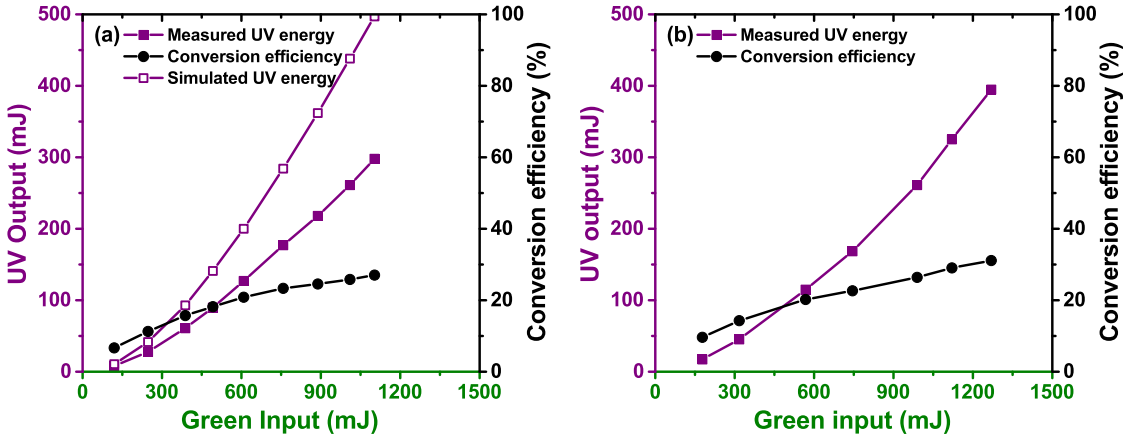

Figure 3.19: (a) Experiment and simulation of SHG from 532 to 266 nm, for the case of 120 mJ SBS generator input energy being used; (b) Experiment of SHG from 532 to 266 nm, for the case of 240 mJ SBS generator input energy being used.

of SBS compressor are proportional to the generator input energy. Here, we compare the generation of sub-nanosecond UV pules while operating the compressor at two different initial conditions. Figure 3.19(a) shows both the experiment and simulation of SHG from 532 to 266 nm, for the case of 120 mJ SBS generator input energy being used. The maximum UV energy of 300 mJ, with a corresponding conversion efficiency of 27%, has been achieved at the maximum green input energy of more than 1.1 J. The simulation is carried out to compare with the experiment. A large discrepancy is found between the experiment and simulation, which predicts a maximum UV energy of 500 mJ. The discrepancy between experiment and simulation could be due to two factors. On the one hand, the assumption of average input pulse width introduces error in predicting the conversion efficiency from the simulation. On the other hand, two-photon absorption is not considered by the simulation, but it definitely plays a role in reducing the efficiency in practice. For the case of 240 mJ SBS generator input energy being used, the compressed green pulse has shorter duration therefore higher intensity, which leads to more efficient generation of UV pulse. The maximum UV energy obtained in this case is up to 400 mJ, with a corresponding efficiency of more than 31%.

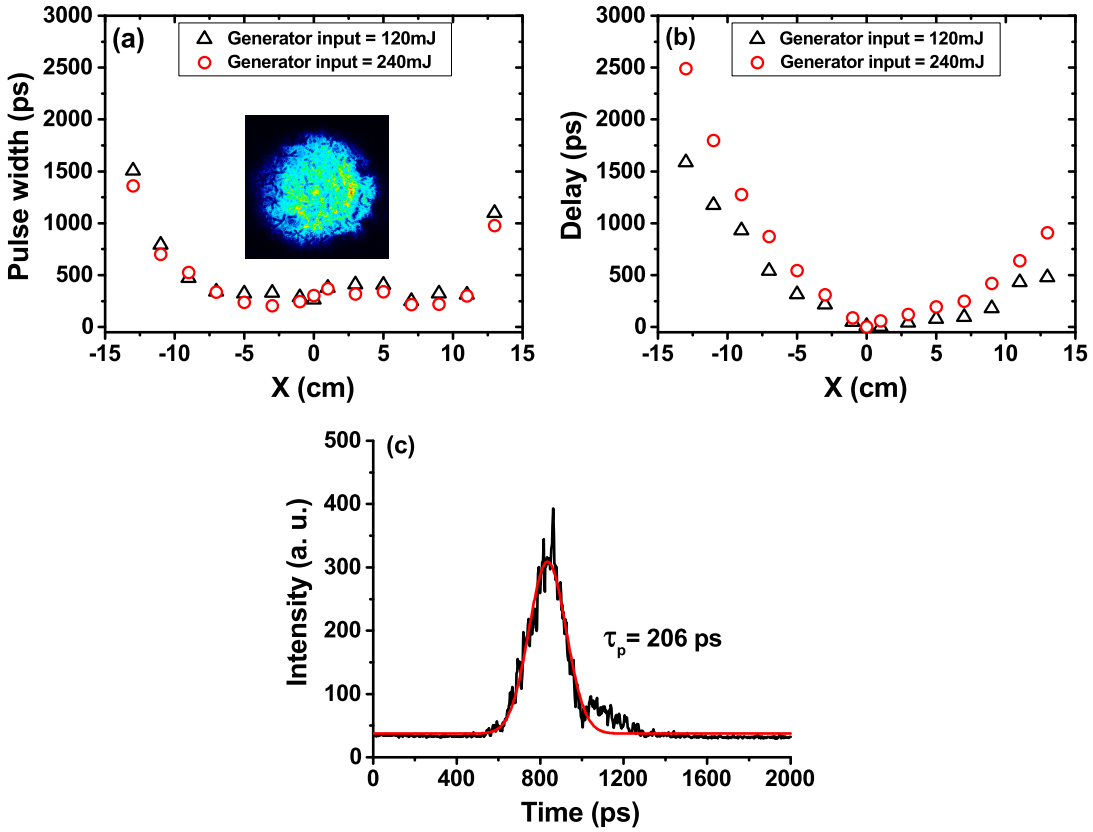

Figure 3.20: (a) Spatial pulse width distributions of UV pulses; Inset shows the typical spatial profile of UV beam at maximum energy of around 1.2 J; (b) Spatial delay distributions of UV pulses; (c) UV pulse recorded by a streak camera with 10 ps resolution.

Besides the characterization of energy performance, the spatio-temporal profiles of UV pulses have also been investigated and displayed in Fig. 3.20. By comparing two cases of operating SBS compressor with different generator input energy, the generated UV pulses are found to have shorter pulse duration but larger delay when higher generator input energy is employed. The different delay distributions have already been identified from the SBS compressed pulses, as shown in Fig. 3.18. It has to be pointed out that the temporal resolution of the pulse detection setup is very close to the pulse duration to be measured. Therefore,the measured pulse is always longer than the actual pulse. To confirm the minimum pulse duration, we have utilized a streak camera that has 10 ps resolution. In the

case of 120 mJ generator input energy, the minimum duration of 200 ps for the UV pulse has been measured by the streak camera, as presented in Fig. 3.20(c). The minimu pulse duration should be below 170 ps, i.e., the minimum duration shown in Fig. 3.14(f), when 240 mJ generator input energy is applied.

Since larger delay exhibited in the UV pulses would lower the beam intensity and further complicate the spatio-temporal profiles In the following chapters where the high power UV pulses are utilized, the SBS pulse compressor is always operated with the total energy of 2 J and generator input energy of 120 mJ. Finally, the spatial profile of the UV beam at maximum output energy of 1.2 J is presented in the inset of Fig. 3.20(a). The time integrated intensity profile exhibits a super-Gaussian distribution. The contamination (low intensity dots and circles) presented inside the beam has been confirmed to be introduced by the 266 nm interference filter, which is used to block the remaining green beam.

3.7 Conclusion

In this chapter, the generation of high-energy sub-nanosecond pulses via stimulated Brillouin scattering has been systematically investigated. water has been demonstrated better SBS medium in achieving high-energy and stable SBS pulse compression. Our main focus of this work has been devoted to resolve the the long existing debate on the minimum pulse duration that can be achieved via SBS pulse compression. It has been shown that sub-phonon lifetime compression can readily be achieved in a single-cell setup. The energy exchange between pump and Stokes pulse is confirmed to be responsible for sub-phonon lifetime pulse compression

The main issue exhibited in SBS compressed pulses is the delay distribution, which has been inherited from the Nd:YAG laser with some modification. It is worth mentioning that the pulse compression ratio does not depend on the spatial delay distributions of the

input pulses. Therefore, the UV laser performance would be dramatically enhanced if the spatial delay can be eliminated for the input pulses to SBS compressor. The following diagram shown in Fig. 3.21 describes an ideal system that is capable of delivering Joule level sub-200 ps SBS compressed pulses free of spatial delay distribution.

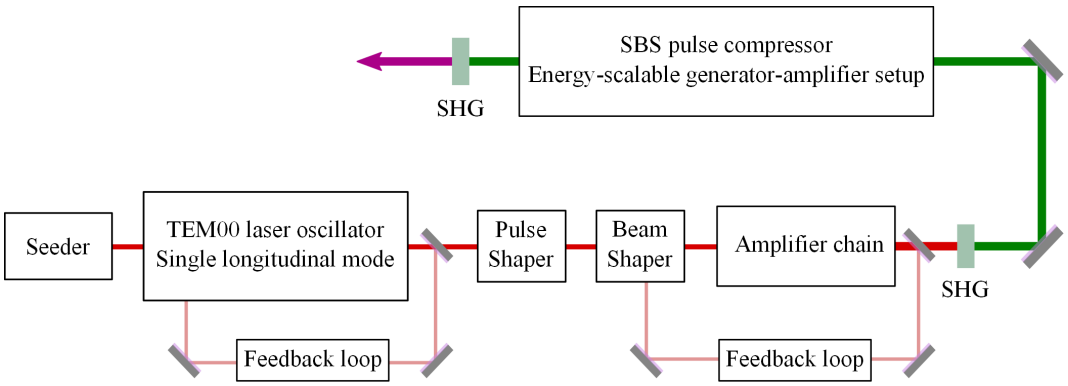

Figure 3.21: Diagram of a new laser system design that is free of spatial delay distribution.

The new system design starts with an injection-seeded Q-switched stable oscillator, which delivers single longitudinal and single transverse mode laser pulses. A pulse shaper is employed to shorten the pulses. With short pulses, the modification of spatio-temporal profile inside amplifiers would be minimized. The length of the SBS cells could also be shortened. A beam shaper such as liquid crystal spatial light modulator (LCSLM) is utilized to finely control the beam intensity sent into the amplifiers. A feedback loop could be used to control the output intensity and the spatio-temporal profile by feeding an input beam with appropriate intensity distribution. Then, the output from the amplifier chain could be frequency doubled and further compressed in the SBS compressor.

Chapter 4

Generation and characterization of sub-nanosecond UV filaments in air

4.1 Introduction

Since their first observations with both near IR [6] and UV [7] femtosecond to several picosecond pulses, laser filaments in air have been extensively investigated because of their wide applications (see review articles [8, 70] and the references therein). To elaborate the filament formation and propagation, different models have been proposed. For example, the moving focus model of Brodeur *et al.* [71] considers the laser pulse to be a stack of time slices that would either self-focus at different positions or diffract, depending on the power they carry. Another model proposed by Dubietis [72] emphasizes on the transverse beam profile shaping by multiphoton ionization that leads to axicon type self-focusing. For those two models, the preparation phase in air plays a very important role. The third model that depicts the filament to be a self-induced waveguide [8] is widely cited for its simplicity. It interprets the filament resulting from a balance between self-focusing due to the spatial Kerr effect and plasma de-focusing that is associated with the multiphoton ionization. In

our case, when the special tool of aerodynamic window [73] is used, the preparation phase of the filament formation is completely eliminated. With this initial condition, the filament is created from a focal spot in vacuum without preparation phase in air. The fact that filaments are observed under theses conditions validates the waveguiding model, but does not invalidate the other models, in the case of filaments prepared in air.

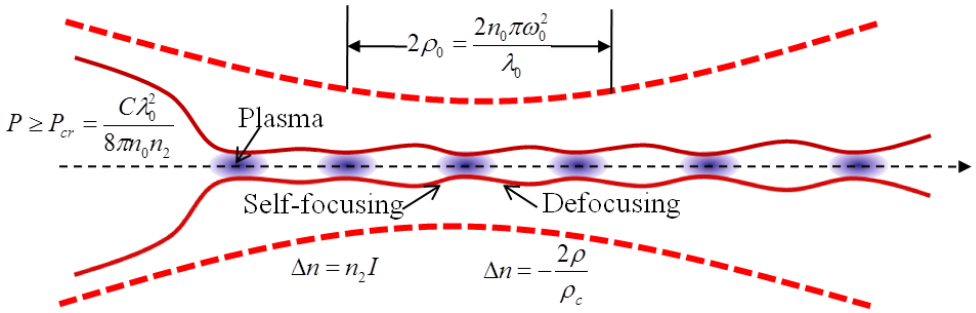

Figure 4.1: Filament initiation and propagation described by the self-guiding model. The positive refractive index change ($n_2 I$) resulted from spatial Kerr effect leads to self-focusing. The plasma generated via multiphoton ionization introduces negative refractive index change ($-2\rho/\rho_c$) to cease the collapse and then diffract the laser beam.

Figure 4.1 shows the schematic representation of filament generation and its propagation that are described by the self-guiding model. When a laser beam with low power is focused in air, it propagates linearly with its characteristic length being twice the Rayleigh range ($2n_o\pi\omega_o^2/\lambda_o$). In nonlinear regime, the laser beam would undergo self-focusing if its power exceeds a critical value P_{cr} ($P_{cr} = 3.77\lambda_o^2/8\pi n_o n_2$ for a Gaussian spatial beam [74]). For example, the critical power in air at atmospheric pressure for laser pulse at 266 nm is 0.13 GW. It is necessary to mention that the concept of critical power applies well to the quasi-continuous-wave (e.g. the sub-nanosecon UV pulse employed here), but can not be viewed as a sharp line between the linear and nonlinear propagation of ultrashort pulses, as recently pointed out by Polynkin and Kolesik [75].

As laser intensity increases dramatically due to the self-collapse, the multiphoton ionization kicks in. The generated plasma via ionization then stops the self-focusing action

and even diffracts the laser beam because of the negative index change. As sketched in Fig. 4.1, a balance between the self-focusing and defocusing leads to the formation of a high intensity beam (i.e., approximately 0.5 TW/cm^2 for UV filament and 50 TW/cm^2 for NIR filament[6]) with its propagation length to be much longer than the Rayleigh range. It should be noticed that the filament itself only harvests a fraction of the input laser pulse energy. The remaining portion maintaining low intensity is usually called *reservoir* that surrounds and co-propagates with the filament. Such reservoir does not exist with the use of an aerodynamic window.

During the filament propagation, the laser pulse looses its power via different processes, such as multiphoton absorption, plasma absorption, new wavelength generation and so on. The filament finally ceases when the laser power is not enough to balance the diffraction. For the case of 800 nm filament, the strong conical emission (new wavelength generation) usually consumes quite a lot laser power and makes the single filament limited by only less than 1 m length [73]. In the application of filament triggered lightning, it has been predicted that filament length of more than 10 m is required. Moreover, the femtosecond filament only carries μJ (UV) to few mJ (NIR) energy, which limits its applications where high energy deposition is desired.

To increase both the filament length and energy, the UNM group has proposed the long pulse UV filament [77, 78]. Later, the long pulse UV filament has been both theoretically investigated and experimentally demonstrated [79]. Since the sub-nanosecond UV source used in the previous work is very unstable due to absence of single longitudinal mode operation (no active feedback in seeded operation) and the poor pulse compression in a single-cell setup, the probability of filament generation has been very low. The characterization on the filament has also been very limited. In this chapter, we report the experimental observation of UV filament generation in air, by employing our newly developed high power UV source. Different initial conditions for the filament generation have been investigated.

[6]Recent estimate of peak intensity is much higher at $I \geq 1.4 \times 10^{14} Wcm^{-2}$ [76].

Besides UV filament, the possibility of generating sub-nanosecond green filaments in air has also been experimentally tested, with the results presented in the end of this chapter.

4.2 Experimental setup

Figure 4.2 presents the experimental setup for UV filament generation and detection. The UV pulses that have been fully characterized in the previous Chapter with energy of 300 mJ per pulse are employed for the generation of UV filaments. A plano-convex lens is employed to focus the UV pulses to localize the filament generation. It has been demonstrated with the NIR filament that the filament properties [80], such as the filament length, plasma density [81] and so on, depend on the focusing conditions. Lenses with a focal length ranging from 0.6 m up to 9 m have been chosen to initiate the UV filament. In the case of 9 m lens being used, the characterization of UV filaments has been performed on the roof of the CHTM building, where the discharge experiment is carried out.

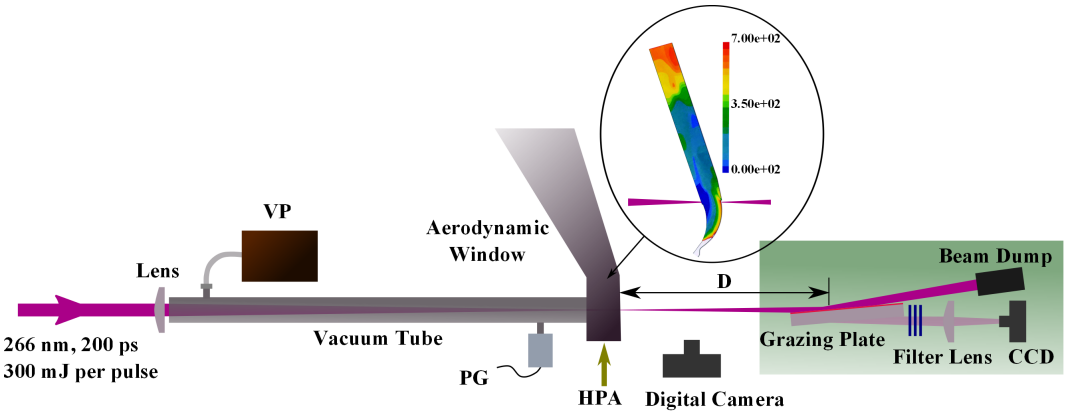

Figure 4.2: Experiment setup for UV filament generation and detection. Inset shows the simulated pressure profile of aerodynamic window when high pressure air of $8\ Kg/cm^2$ is input.The grazing plate is HR coated for 355 nm at 0^o incidence. With 89^o of incidence angle, the transmittance of 266 nm input beam with S polarization is only 0.5×10^{-6}. VP: Vacuum Pump; PG: Pressure Gauge; HPA: High Pressure Air.

Besides the focal length, another initial condition, i.e., focusing the beam either in air or in vacuum, can also be varied by employing our special tool of aerodynamic window. As demonstrated in the inset of Fig. 4.2, a differential pressure in the aerodynamic window that effectively separates low pressure vacuum chamber (experimentally measured to be 10 Torr) from atmospheric pressure (around 630 Torr in Albuquerque) on the outside is created by a supersonic air flow. Since any self-focusing or higher order nonlinearity is absent in the vacuum chamber prior to the filament formation, the onset of filament (boundary condition) can be very well defined. By using the aerodynamic window, it has been demonstrated that the spectral component of NIR filament is strongly dependent on the preparation medium [82]. For the UV filament, its size dependence on the preparation phase will be reported.

In filament characterization, we use a digital camera to image the plasma channel. To measure the filament spatial profile, linear attenuation is a prerequisite. Otherwise, the high intensity filament can damage any diagnostic optics. One solution is to use a plate of fused silica at grazing incidence. This was employed by other groups and was also used to observe the first UV filaments [79]. Unfortunately, the small fraction of the beam that is transmitted through the plate (6% for $\theta_i = 89^o$) is still above the critical power for self-focusing in fused silica. The wavefront distortion and self-phase modulation can be minimized by using a thin plate ($\leq$1 mm). Then, it is however impossible to have the required flatness of $\lambda/10$ over the 10 cm diameter required for grazing incidence.

The solution that we bring is to use a rigid mirror of 6" diameter and 1" thickness with proper coating. In the case of 266 nm with grazing incidence, the mirror with 355 nm high reflectivity (HR) coating at 0^o incidence could reach an attenuation of 10^6 [73]. The theoretical transmission curves have been verified for eight different wavelengths, at a grazing incidence of 88.5^o. This method of attenuating the beam is limited to linearly s-polarized beams. Extra care has to be taken to convert the filamenting beam from p-polarization to s-polarization by using a half waveplate. After the attenuator, a CCD camera is used to

capture the spatial profile of the filament. By replacing the camera with a spectrometer, the spectral components of UV filament could also be investigated.

4.3 UV filament generation with different initial conditions

4.3.1 Using different focal length lenses in filament generation

We first investigate filament generation by focusing the UV beam in air. Four different focal length (i.e., 0.6 m, 1.5 m, 3 m and 9 m) lenses have been employed to explore the dependence of focusing condition. In this case, the aerodynamic window is not in use.

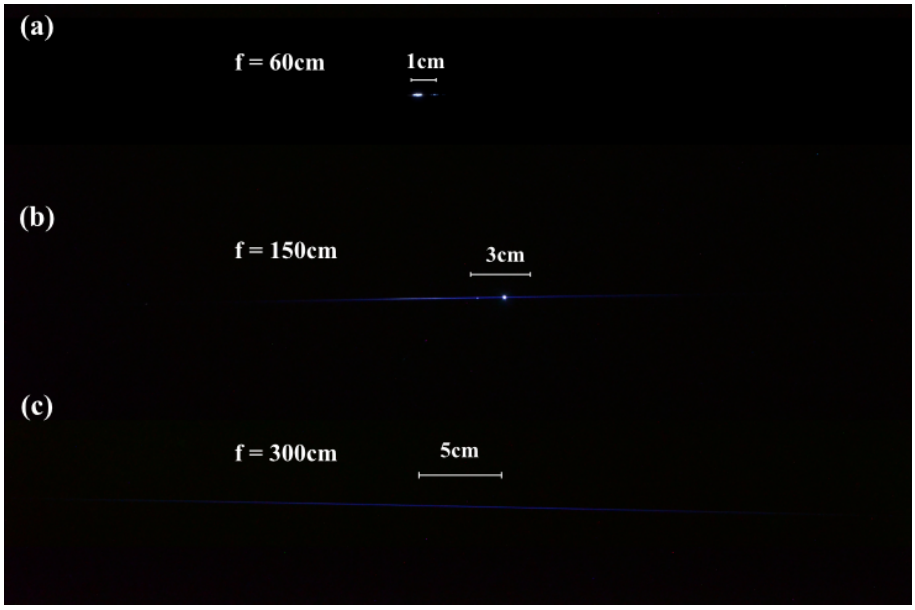

Figure 4.3: Direct image of plasma channels generated with three focusing lenses of (a) 0.6 m, (b) 1.5 m and (c) 3 m, respectively. The laser beam is propagating from left to right.

The plasma columns generated with 0.6 m, 1.5 m and 3 m focusing lenses are imaged by

the digital camera and presented in Figs. 4.3(a)-(c), respectively. The UV beam propagates from left to the right hand side. The bluish color captured by the camera is the plasma emission. In order to have enough brightness, the image is integrated over 35 laser shots. It can be seen that the generation of UV plasma filament depends on the focusing condition. When lens of 1.5 m focal length is used, the avalanche ionization featured by a bright plasma bead has been observed once or twice every 35 shots. The probability in observing plasma bead is getting much higher to almost every shot when a 60 cm focusing lens is employed. However, when long focusing lens is used, a smooth plasma channel is created, as demonstrated by the case of 3 m focusing. In case of NIR plasma filament, the above mentioned focal length dependence has not been observed. As will be discussed in detail in Section 4.4, the generation of plasma beads is associated with the spatio-temporal profile of the input UV pulses that has been quantitatively characterized in the previous chapter. For the case of 9 m focusing lens, we have not observed plasma beads neither. Since the long plasma channel is used for triggering and guiding the discharge, a more quantitative characterization of the conductivity has been performed and will be discussed in detail in Chapter 6.

Knowing the focusing condition that is appropriate for filament generation, we move to characterize the UV filament profiles with three focusing lenses (i.e., 1.5 m, 3 m and 9 m). We first take some reference beam profiles that can be used to compare with the filament generated with high power UV beam.

The spatial profile of low power beam being focused by a 3 m lens is first recorded at 2.1 m after the geometric focus, and presented in Fig. 4.4(a). No filament or any intensity modulation is observed, as expected. Next, the spatial profile at full power of the UV beam, focused by the same 3 m lens, is captured at 1.3 m *before* the geometric focus. As demonstrated in Fig. 4.4(b), the filament has not yet started from that point. This measurement can confirm the observation of a filament recorded 1.3 m after the geometric focus, as will be shown below. It should be noticed that all the profiles are captured some distance away

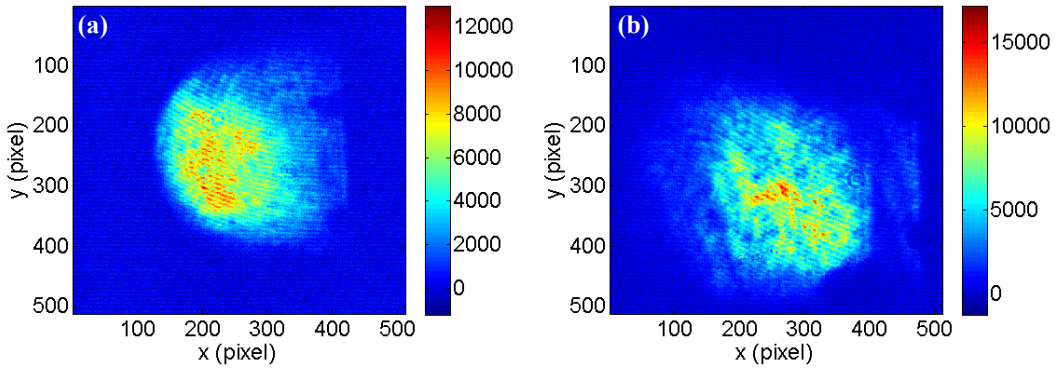

Figure 4.4: (a) Low power UV beam profile recorded at 2.1 m after the geometric focus while focused by a 3 m lens. (b) Full power UV beam profile recorded at 1.3 m before the geometric focus while focused by a 3 m lens.

from the geometric focus. Otherwise, the HR coating for the grazing plate will be easily damaged because of the high UV energy.

Figures 4.5(a)-(c) show the typical profiles of filament, initiated with different focal length lenses. In the case of the shorter focal length lens (i.e., 1.5 m and 3 m) being used, the generated filaments stay in the single filament regime [Figs. 4.5(a) and (b)]. In the case of a 9 m lens, the spatial profile has been recorded by a digital camera. It is clear that multiple filaments (high intensity dots) have been generated. As will be shown in Chapter 6, the multiple filaments last for more than 3 m. The difference in filament generation is attributed to two factors. On the one hand, the UV beam has been propagated about 30 m to where the multiple filaments being observed. Since the initial high power UV beam has super-Gaussian spatial profile that is not a free propagation mode, its intensity distribution evolves and becomes quite different after the propagation. It has been demonstrated that the critical power is different for laser beam with different spatial profile [74]. It is therefore reasonable to observe the difference in filament generation because of the different initial conditions. On the other hand, the UV beam experiences more turbulence when it propagates on the roof in an open environment. Intensity modulation of the UV beam acquired from the

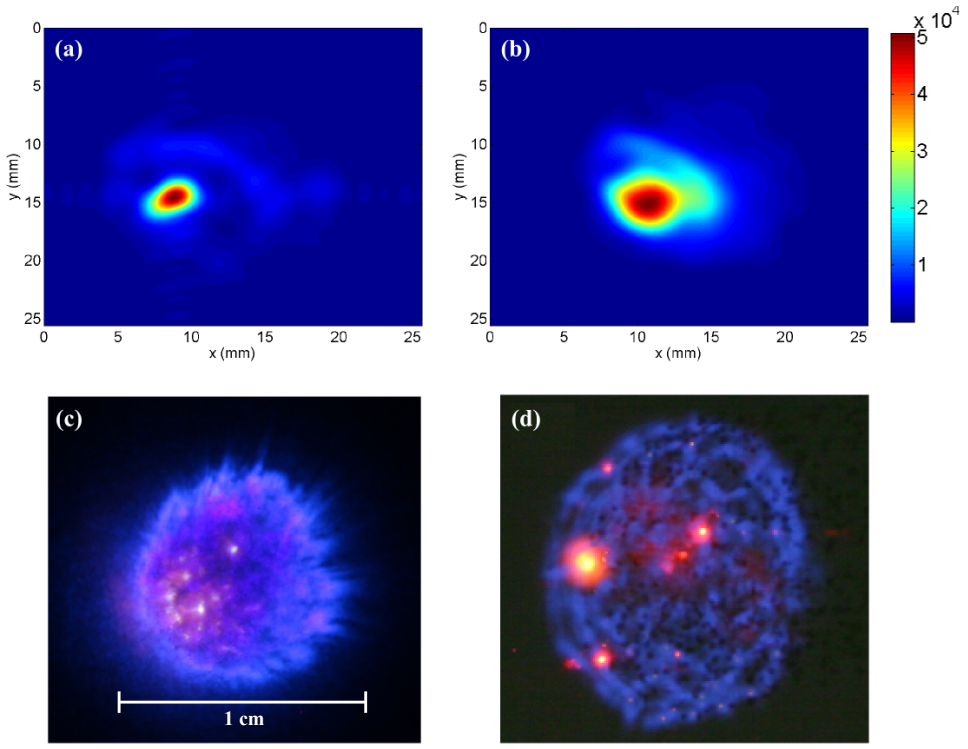

Figure 4.5: (a) UV filament profile recorded at 1.05 m after the geometric focus while focused by a 1.5 m lens. (b) UV filament profile recorded at 2.1 m after the geometric focus while focused by a 3 m lens. (c) UV filament profile recorded at 1 m after the geometric focus while focused by a 9 m lens. (d) NIR filament profile cited from reference [83].

turbulence is expected to favor the generation of multiple filaments.

To have a comparison, the multiple NIR filaments generated with similar focusing condition (f=10 m) has been demonstrated in Fig. 4.5(d) [83], which is similar to the UV filament observed here. In the case of NIR filament, the spectrum is typically broadened, via nonlinear processes such as self phase modulation and four wave mixing, to cover the range from visible to near IR. The spectral broadening therefore contributes to the observation of colorful spots. For the UV filament, the above mentioned nonlinear processes are not presented because of the lower clamping intensity (0.5 TW/cm^2 as compared to 50 TW/cm^2 in the NIR). The longer pulse duration of the UV filament favors the generation of discrete

new wavelength by stimulated Raman scattering with relatively high efficiency, as will be discussed in detail in the next Chapter.

4.3.2 Filament generation by focusing UV beam in vacuum or air

After having observed filament by focusing the UV beam in air, we bring in the aerodynamic window such that the initial preparation phase could be controlled for the filament generation. The 3 m lens has been chosen in this case to focus the UV beam 2 mm before the exit of the aerodynamic window. The detection setup has been translated along the beam propagation direction to characterize the filament profiles. When the grazing plate is placed after the aerodynamic window within 1.3 m, we have observed coating damage, which therefore limits the measurement to be at least 1.3 m away from the window exit. As shown in Fig. 4.6, the filament with similar beam size keeps propagating a long distance

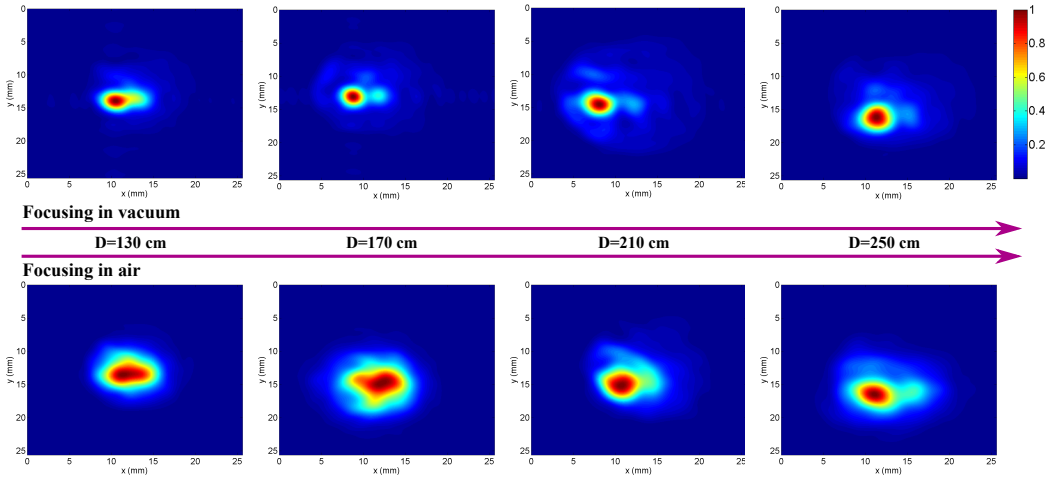

Figure 4.6: UV filaments generated with 3 m focusing lens. The filament profiles are sampled at 4 longitudinal positions with D=130 cm, D=170 cm, D=210 cm and D=250 cm, respectively. The maximum distance is limited by the available laboratory space. Top row: filaments generated by focusing the high power UV beam in vacuum; Bottom row: filaments generated by focusing the high power UV beam in air without operating the vacumm chamber.

that is much longer than the Rayleigh range. By comparing the filaments generated with two different initial conditions, the filament generated by focusing UV beam in air has a larger size as compared to the other case, which matches the previous observation [19]. Since there is almost no loss by focusing the UV beam in vacuum, the smaller filament size in this condition is attributed to be the higher initial power that the UV beam/filament could carry. It should be pointed out that the filament size (1-2 mm FWHM) characterized here is quite different from that (300-400μm) of the filament being observed by Chalus [19]. We attribute the difference being possibly resulted from the different spatio-temporal profile of the UV pulses.

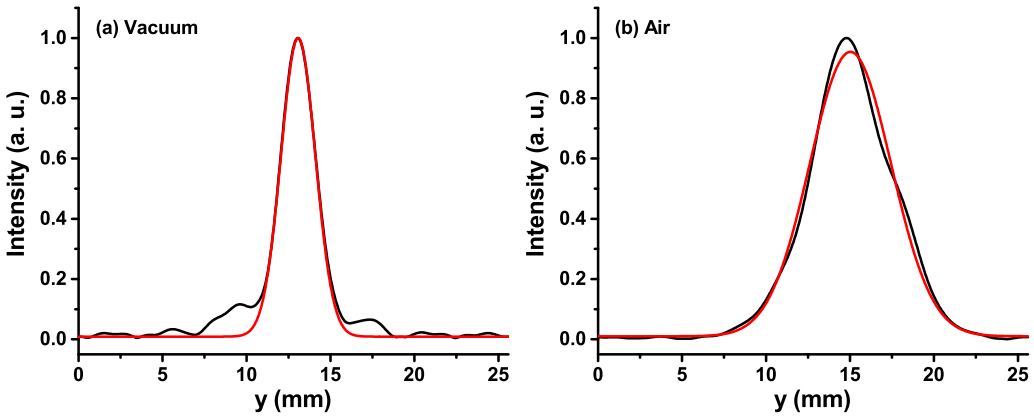

Figure 4.7: 1-D intensity profile along Y axis for filament taken at D=1.7 m. (a) UV beam being focused in vacuum. (b) UV beam being focused in air. Black curve is the experimental measurement, while red curve is Gaussian fit to the experimental data.

The one dimensional (1-D) intensity profile of the filaments sampled at D=1.7 m have been extracted from the 2-D profiles presented above and demonstrated in Fig. 4.7. A Gaussian fit has been made for the experimentally measured profile with good accuracy, especially for the case of filament generation with UV beam being focused in vacuum. In the previous theoretical study, it has been shown that the eigenfunction solution of the simulation has only very little difference from the Gaussian distribution [19]. Therefore, it is reasonable to have a good match between the experimentally measured profile with the

fitted Gaussian profile.

4.3.3 Effort on generating filament with UV vortex phase mask

The multiple filaments reported in Fig. 4.5 are always presented at random transverse positions. With well organized multiple filaments in the transverse plane, a plasma cylinder or air waveguide (with lower refractive index at the outer side of a cylinder because of air rarefaction) could be formed. Those specially shaped waveguides could be applied into the microwave guiding [17] or optical wave guiding [84]. With a similar idea, we have proposed using UV vortex filament to trap the NIR filament [85].

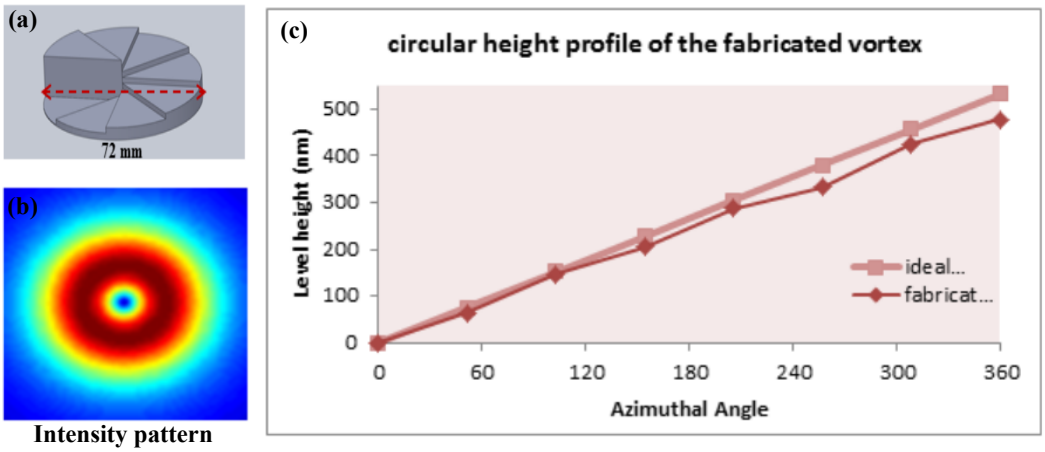

Figure 4.8: (a) Structure of the UV vortex phase mask. (b) The designed intensity pattern of the vortex beam. (c) The comparison of circular height profile of the designed and fabricated phase mask.

Experimentally, we employ a UV vortex phase mask provided by Professor Eric Johnson from Clemson University. Figures 4.8(a)-(c) show the phase mask structure, the simulated UV intensity pattern after the mask and the comparison of height profile for the designed and characterized mask, which are all adapted from [86]. As shown in Fig. 4.8(c), the characterized structure height has up to 10% difference from the designed value at the

Azimuthal angle of 360 degree, which is the main reason for the failure in observing vortex beam, as demonstrated in Fig. 4.9.

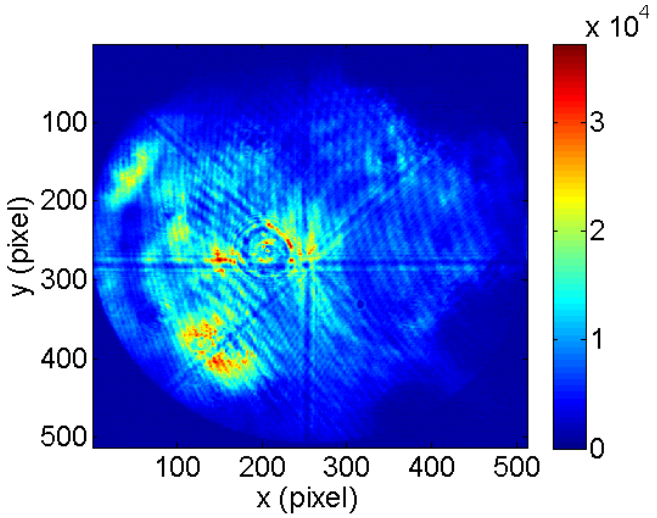

Figure 4.9: UV intensity profile after passing through vortex phase mask.

4.4 Experimental test of green filament generation in air

Other than the UV filament, we have also tested the possibility of generating green (532 nm) filament in air. In this case, part of the SBS compressor output (600 mJ) is directly focused in air with a 3 m lens. Figure 4.10 presents the picture of beam trace recorded by a digital camera. A train of plasma beads generated via avalanche ionization have been observed. The positions where the beads located are around the geometric focus but totally random for each laser shot. It is worth emphasizing that the self-focusing is balanced by the plasma defocusing via multiphoton ionization in the filament. With the plasma beads, the laser beam would be either dramatically attenuated or completely blocked if the plasma frequency is higher than the optical frequency of the laser pulse. It is therefore impossible to have filament generation in such case.

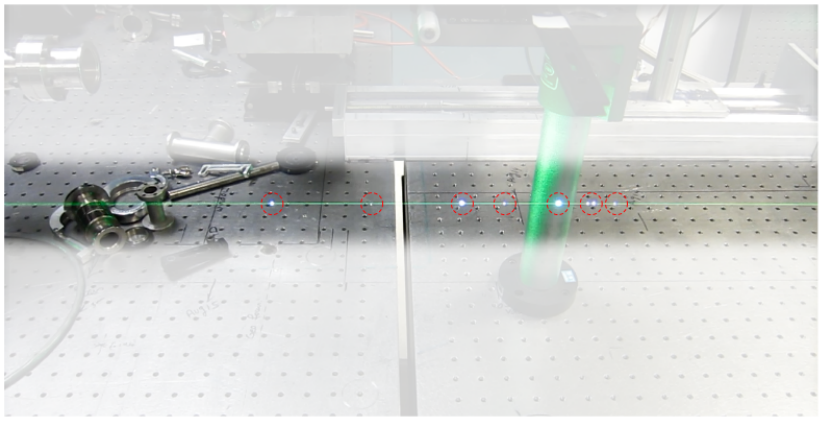

Figure 4.10: Photograph of the green beam trace with plasma beads (marked out by red circles) generated by avalanche ionization when high intensity sub-nanosecond green laser pulse is focused in air with 3 m lens.

The generation of plasma beads can be well explained by the established theory. It is known that the inverse Bremstrahlung (heating of the average electron temperature in an optical ïňĄeld) leads to avalanche when the electron temperature (in eV) reaches the ionization potential (I_p=12.5 eV for oxygen molecule). The time to reach avalanche can be expressed as [78, 87]

$$\Delta t = \frac{\epsilon_0 c m_e \omega^2}{2 I \nu_{eff} e^2} I_p \tag{4.1}$$

where I and ω are the laser intensity and frequency, respectively; m_e is the electron mass and ν_{eff} represents the effective rate of momentum transfer between an electron and a heavy particle. Therefore, the upper limit of the laser pulse duration set by inverse Bremstrahlung is inversely proportional to the wavelength squared times the intensity of the light.

In the case of 248 nm, the longest pulse duration allowed to form filament is about 4 ns [78]. By considering the filament intensity scaling law (i.e., the clamping intensity increases as the wavelength gets longer) and the wavelength difference, the longest pulse duration for 266 and 532 nm lasers are estimated to be 1 ns and 10 ps, respectively. It is obvious that the pulse duration of our available sub-nanosecond green pulses is beyond the

upper limit. Hence avalanche ionization is observed even with long focusing condition. To explain the experimental observation for the case of 266 nm, we need to recall the spatio-temporal profile of the UV pulses that has been presented in Section 3.6. The UV pulses located around the beam center have the duration of less than 1 ns therefore would create a smooth plasma channel. There are however pulses of more than 1 ns located at the outer region of the beam and delayed from the center pulses. Those long pulses can act as heater to raise up the temperature of the electrons that have been created earlier via inverse Bremstrahlung. Being focused with a shorter focal length lens, the intensity of the heater beam is higher thereby with stronger inverse Bremstrahlung effect, which can lead to avalanche ionization manifested by the plasma beads.

It is worth mentioning that the above scenario has been experimentally demonstrated with two lasers [88], where the first femtosecond laser creates a smooth filament plasma channel and a second delayed nanosecond laser with enough intensity introduces plasma beads on top of the existing plasma channel. The issue experienced with the UV filament generation could be eliminated, by employing the UV source that has been proposed in the end of Chapter 3.

Chapter 5

Application of filaments for Remote spectroscopy

Laser filaments have peculiar properties such as long propagation distance, generation of a continuous plasma channel which includes molecules and ions in excited state, as well as strong white light emission in the case of femtosecond NIR filament. Those characteristics make the filament suitable for various techniques of remote sensing. Several possibilities have been demonstrated so far with the NIR filaments . First, absorption spectroscopy of the atmosphere has been performed by range gating the backscattering from the white light supercontinuum, which has severed as a remote broadband spectroscopic source [9,89–91]. Second, as a versatile real-time analysis tool, filaments are being applied for Laser Induced Breakdown Spectroscopy (LIBS) and remote sensing capability of up to 200 hundred meters has been demonstrated [92]. Very recently, intensive studies [93–107] have shown strong emissions from NIR filaments in both forward and backward directions, which opened another possibility for remote sensing application. One last technique based on stimulated Raman spectroscopy has also been recently employed in a proof-of-principle experiment for gas sensing when combined with Mid-IR filaments [108]. Since the required backward Stokes pump can only be generated with pressurized gases of mixed N_2 and Ar,

it is still far away from utilizing the proposed scheme for real remote sensing application.

So, can we apply the UV filaments into remote sensing by employing the same techniques as mentioned above? To answer this, we need to recall the difference between UV and NIR filaments. First of all, the UV filament does not create supercontinuum generation as already discussed in the previous chapter, which excludes the possibility of utilizing absorption spectroscopy technique. Second, the strong emission from molecular ions (e.g., N_2^+) observed from NIR filaments always involve population inversion, which is still under debate of either from electron recollision [107] or multiphoton resonance pumping [109]. Since UV filament can not satisfy either of the requirements, we have not experimentally observed the typical N_2^+ emission at 428 nm from UV filaments.

However, with very narrow bandwidth ($<$ 1 GHz) combined with high energy, UV filament is the idea source to excite stimulated Raman scattering (SRS), which could be employed for identifying different species that have distinct Raman modes. The UV filaments are also advantageous in performing laser induced breakdown spectroscopy (LIBS). With broadband supercontinuum generation, NIR filaments can introduce spectral contamination to the emission spectrum (an effect that can be mitigated through temporal gating). It is much less problematic for the UV filaments with very narrow bandwidth. Due to its much higher energy, the UV filaments also create stronger plumes and their associated emissions. In this chapter, we report on our investigations on both Raman spectroscopy and LIBS with UV filaments.

5.1 Application of filaments for stimulated Raman spectroscopy

In this section, we first show SRS excited by UV filaments in the forward direction. It is found that the SRS efficiency is gas pressure and pump polarization dependent. Next,

we investigate the backward emission from UV filaments. So far, we have only observed backward stimulated Brillouin scattering, which can be employed for sensing application, but requires a detection setup of high spectral resolution. In the last part of this section, we report on impulsive stimulated Raman scattering excited by NIR filaments and probed with weak UV pulses. The latter study is essential in enhancing desired Raman signals from pollutants under investigation.

5.1.1 Stimulated Raman and Brillouin scattering excited by UV filaments

Experimental setup

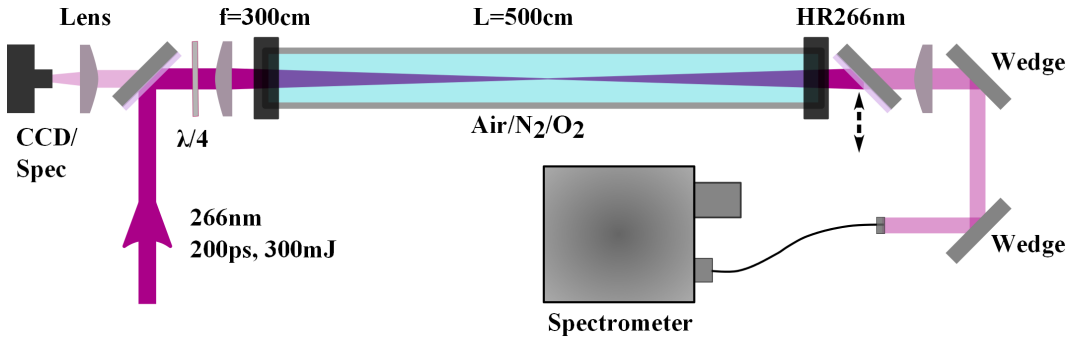

Figure 5.1: Experiment setup for the excitation and detection of stimulated scattering from UV filaments.

To investigate the stimulated scattering excited by UV filaments, we have utilized the experimental setup illustrated in Fig. 5.1. UV filaments are generated by focusing the full power UV beam with a 3 m focal length lens into a 5 m long gas cell, i.e., a transparent plastic tube that is employed to fill different gases with controllable pressure. A quarter-wave plate ($\lambda/4$) is used to control the polarization of the initial laser pulse. In the forward direction, a 266 nm 45^0 high reflectivity mirror is employed sometimes to attenuate the pump beam. Since the high reflectivity (>90%) covers the spectral range from 240 nm to

290 nm, the first Stokes and first anti-Stokes lines are both much attenuated when the mirror is used. Another two uncoated wedges are always employed to attenuate the whole output. The spectral components are then analyzed by either an Ocean Optics fiber coupled spectrometer (HR2000CG-UV-NIR) with 1 nm spectral resolution or a DEMON spectrometer (Lasertechnik Berlin, Germany) with 5 pm or 0.5 cm^{-1} resolution around 266 nm. The DEMON spectrometer is a double-echelle type monochromator with an Andor ICCD camera, that can be gated via its photocathode. For the backward direction, a CCD camera and a spectrometer are used to record the backward emission.

Forward stimulated vibrational Raman scattering

We first report on the forward stimulated vibrational Raman scattering excited by UV filaments with linear polarization in different gases (air, N_2 and O_2). The vibrational lines of N_2 and O_2 with the excitation line of 266.05 nm are listed in Table 5.1.

Table 5.1: Vibrational Raman lines of N_2 and O_2

N_2 ($\Delta\nu = 2330cm^{-1}$)			O_2 ($\Delta\nu = 1556.26cm^{-1}$)		
order	Anti-Stokes (nm)	Stokes (nm)	Stokes (nm)	Anti-Stokes (nm)	order
1^{st}	250.52	283.63	277.54	255.47	1^{st}
2^{nd}	236.70	303.70	290.07	245.70	2^{nd}
3^{rd}	224.33	326.83	303.78	236.65	3^{rd}
4^{th}	213.19	353.77	318.86	228.25	4^{th}
5^{th}	203.10	385.55	335.51	220.42	5^{th}
6^{th}	193.92	423.60	353.99	213.11	6^{th}
7^{th}	185.54	469.99	374.63	206.27	7^{th}

Figure 5.2 presents the Raman signal from air at different pressures. At atmospheric pressure (12 psi or 630 torr in Albuquerque), up to 2^{nd} order Stokes and anti-Stokes lines have been observed, as demonstrated in Fig. 5.2(a). Since the Raman signal is relatively weak, the HR mirror is not used in this case, which explains the saturation of the laser line. It is known that the Raman gain is proportional to the density of molecules [64], which can be controlled by tuning the gas pressure. As shown in Figs. 5.2(b) and (c), higher order

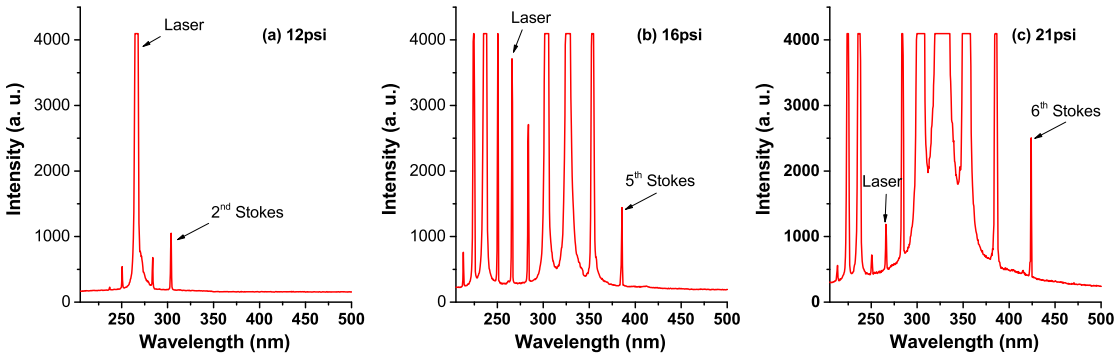

Figure 5.2: Forward stimulated vibrational Raman scattering excited by UV filaments from air with different pressures; (a) 12 psi; (b) 16 psi; (c) 21 psi. The observed spectra only contain the vibrational lines from N_2.

Stokes and anti-Stokes lines have been obtained as the air pressure increases from 12 psi to 21 psi. The intensity of vibrational lines near the laser line as well as the laser line itself have been attenuated by the 266 nm HR mirror. In order to capture the highest order Stokes line, the lower order Stokes lines are kept saturated.

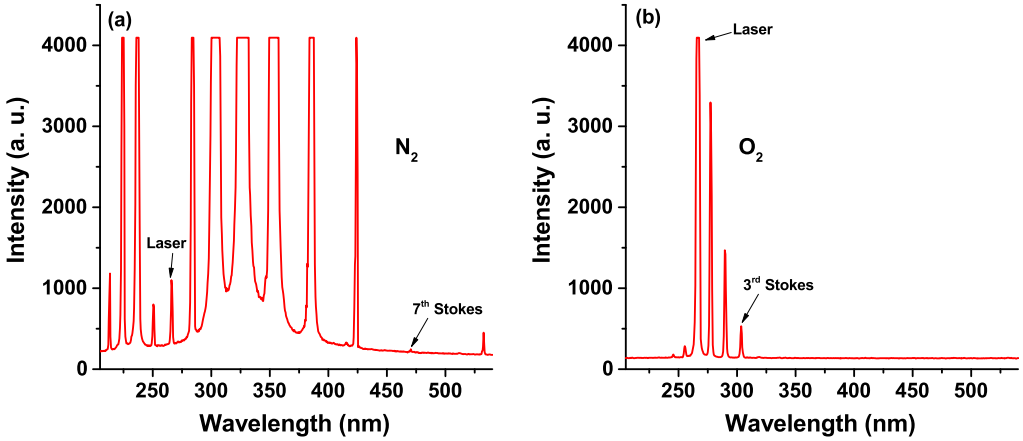

Figure 5.3: Vibrational Raman spectrum of pure (a) N_2 and (b) O_2 at the pressure of 21 psi.

By comparing the observed lines with the ones listed in Table 5.1, it is found that only vibrational lines from N_2 have been obtained. Since the air still has 20% of O_2, the ques-

tion is why the Raman lines from O_2 have not been observed. To understand the reason, the vibrational Raman spectrum from pure N_2 and O_2 at 21 psi have been acquired, as demonstrated in Fig. 5.3. In the case of N_2, up to 7^{th} order Stokes line has been observed. The energy of the Raman signal has been measured and converted to be up to 30 mJ by considering the attenuation of 266 nm HR mirror. The corresponding energy efficiency is as high as 10%. In the case of O_2, the 266 nm HR mirror is not used in order to obtain the much weaker Raman signal, as shown in Fig. 5.3(b). The first order Stokes line from N_2 that is attenuated by more than 90% is still much stronger than the unattenuated first order Stokes line from O_2. This indicates that the O_2 vibrational Raman signal has been buried under the much stronger signal from N_2 when air is under investigation.

Forward stimulated rotational Raman scattering

Besides the vibrational lines, the rotational spectrum can also be used to distinguish different species. The results shown above have demonstrated that the vibrational lines overwhelm the Raman spectrum, which makes it very difficult to observe the rotational lines. However, it is found that the intensity ratio between the vibrational line and rotational line can be controlled by the pump polarization. As demonstrated in Fig. 5.4(a) the rotational lines around 266 nm from N_2 can be enhanced with circularly polarized pump. In the meanwhile, the vibrational lines are suppressed. For the case of O_2, the rotational lines are however found to be insensitive to the pump polarization, as illustrated by Fig. 5.4(b). The difference mentioned above can be attributed to the different orbital structures of N_2 and O_2, which are presented as the insets in Fig. 5.4.

With circularly polarized pump light, we further analyze the rotational lines of N_2 associated with the main 266 nm laser line and the first vibrational Stokes line. Figure 5.5(a) shows the stimulated rotational Raman spectrum around the laser line, which covers several nanometers range. Since the high resolution spectrometer has limited spectral window for each measurement, successive spectra taken at different central wavelength and represented

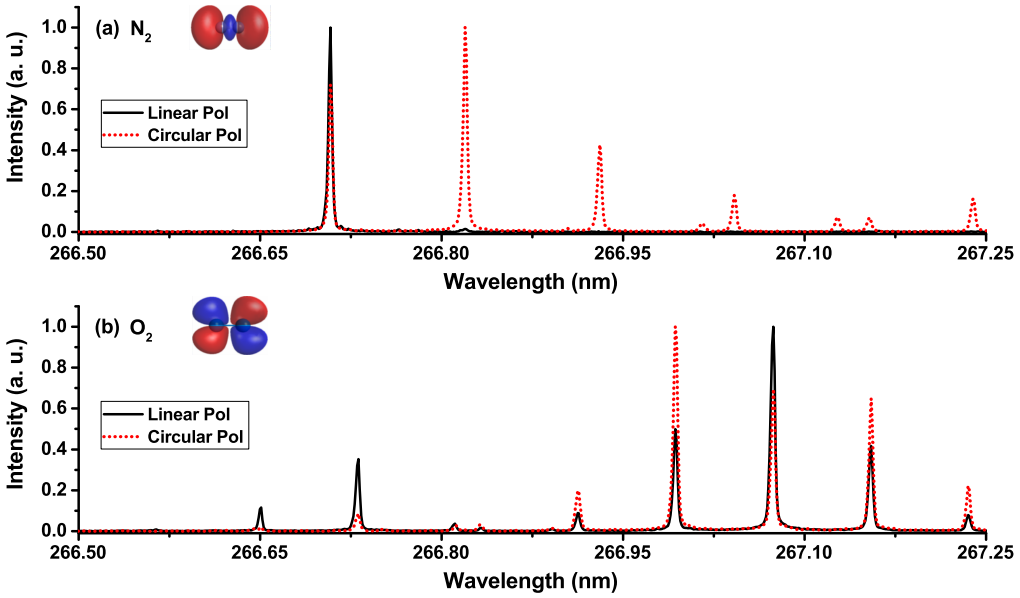

Figure 5.4: Polarization dependence of rotational Raman spectrum of pure (a) N_2 and (b) O_2 at the pressure of 21 psi. The insets show the Dyson orbital structures of N_2 and O_2 that are cited from reference [110].

with different color lines have to be stitched together. The gain factor for each measurement has also been labeled by the magnification number to indicate the relative intensity among different parts of the Raman spectrum.

To study the details, we first zoom in to the region around the laser line, as demonstrated in Fig. 5.5(b). We also convert the horizontal axis to wavenumber shift as is conventionally used for Raman analysis. It has been reported [111] that the wavenumber shift of the rotational Raman lines with respect to the pump line are given by

$$\Delta\bar{\nu} = B\,(4j+6)\,\left(cm^{-1}\right) \tag{5.1}$$

where B is the rotational constant in unit of cm^{-1} and j is the rotational angular momentum quantum number. The pure rotational Raman scattering follows the angular momentum selection rule with $\Delta j = \pm 2$ for two successive dipole transitions. Then, it is found that the spacing between two successive lines corresponding to either two odd-j or two even-j

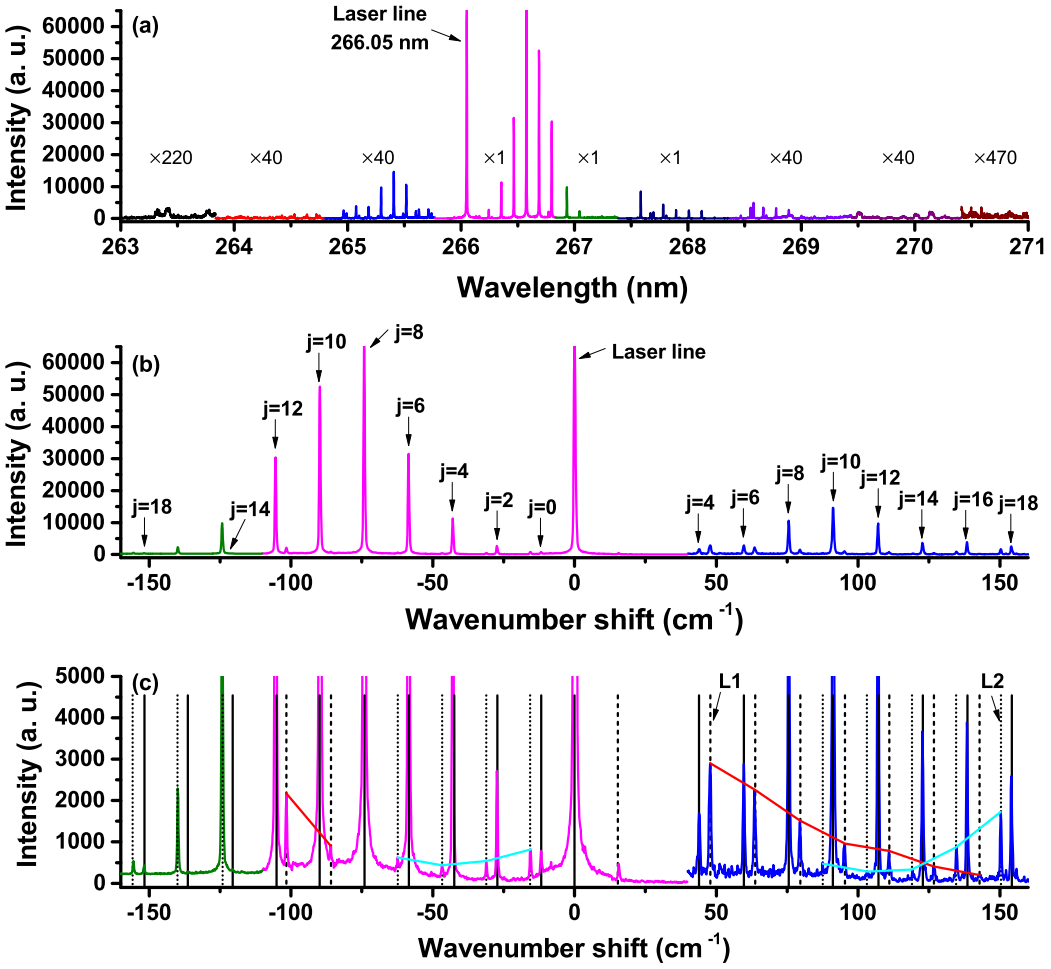

Figure 5.5: Stimulated rotational Raman spectrum of pure N_2 around the laser line at 266.05 nm with circular polarization; (a) Full spectrum; (b) A zoomed in spectrum around the laser line; (c) Identification of three different sets of rotational lines; Solid lines: Rotational lines derived from the laser line; Dashed lines: Each line is an accumulation of the 2^{nd} order rotational Raman lines derived from the 1^{st} order rotational Raman lines with Stokes shift; Dotted lines: Each line is an accumulation of the 2^{nd} order rotational Raman lines derived from the 1^{st} order rotational Raman lines with anti-Stokes shift. Magnification number shown in (a) indicates the gain used for each spectrum measurement.

numbers is 8B. The spacing between two successive lines corresponding to one odd-j and one even-j numbers is 4B. It should be noticed that the spacing between the first line and the laser line is 6B.

It has been shown for N_2 that the intensities alternate by a factor of 2 between the even-j and odd-j terms of the Raman spectrum due to the influence of the *nuclear spins* [111]. From our measurement, the intensity alternation has however not been observed. The rotational lines corresponding to odd-j numbers are missing. Actually, similar experimental observation of only rotational lines corresponding to even-j numbers from neutral N_2 has been reported in [102]. It therefore indicates that the excitation of rotational lines might depend on other factors that need to be identified.

Supposing the widest spacing between two successive lines is 8B, we can extract the mean value of the B constant from the measured spectrum to be 1.96 cm^{-1}, which matches fairly well with the quoted value of 1.998 cm^{-1} from reference [112]. It is worth mentioning that the spectral resolution of the spectrometer is 0.5 cm^{-1}, which we believe is responsible for the discrepancy in B values. By using the derived B value, the first rotational Stokes Raman line with j=0 ($\Delta\bar{\nu} = 6B$) and other Stokes lines corresponding to even-j numbers (up to j=56) can readily be identified. For the anti-Stokes side (with positive wavenumber shift), the first two lines (j=0,2) have not been observed mainly because of their weak intensity (i.e., weaker than the first two Stokes lines). Other rotational anti-Stokes Raman lines that correspond to the even-j numbers have also been labeled as shown in Fig. 5.5(b).

It can be seen in Fig. 5.5(b) that there are still some unidentified peaks. To have better visibility with those small peaks, we have modified the vertical axis of Fig. 5.5(b) to get Fig. 5.5(c). All the rotational lines labeled in Fig. 5.5(b) have been relabeled with black solid line in Fig. 5.5(c). After examining other peaks that have enough signal to noise ratio (SNR), an interesting phenomenon has been found with all those unlabeled peaks having the spacing of either 2B or 6B to its nearest two lines that have been previously labeled. This indicates that those unlabeled peaks could be the 2^{nd} order rotational Raman lines, which have been shifted from the 1^{st} order rotational Raman lines (labeled by solid lines) by 6B and have the same spacing of 8B. Depending on the shifting direction (i.e., shifting either to the left or to the right), we have labeled two sets of Raman spectra with either

dashed (Stokes) or dotted (anti-Stokes) lines.

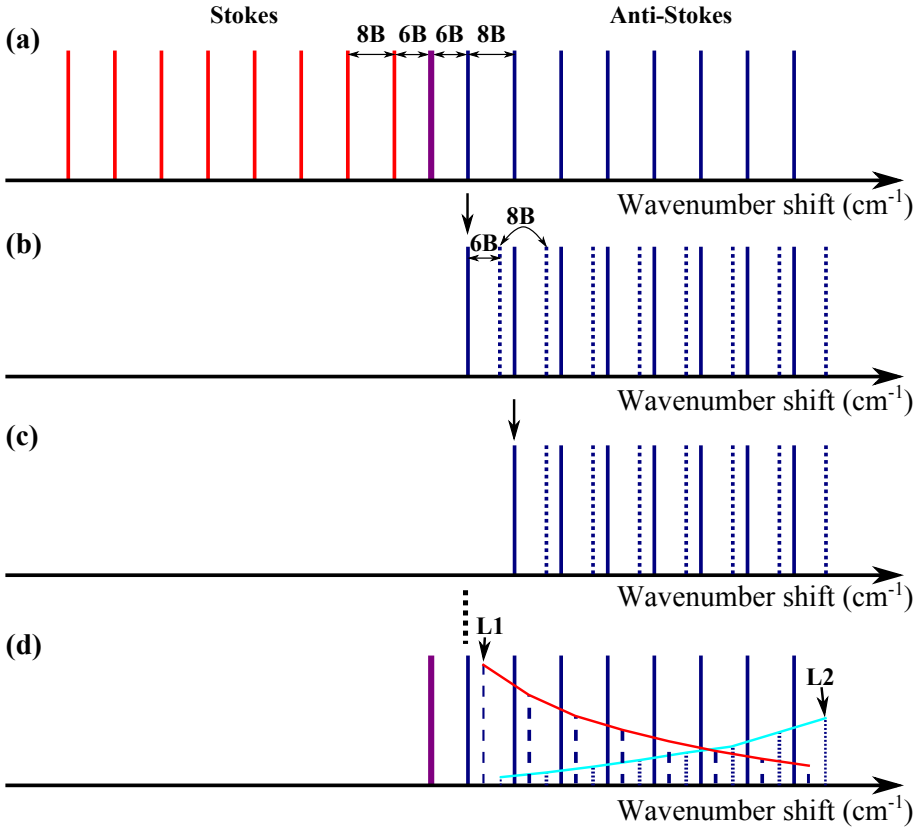

Figure 5.6: A sketch to explain the generation of 2^{nd} order stimulated rotational Raman lines (a) Generation of 1^{st} order stimulated rotational Raman lines from the laser line; (b) Generation of 2^{nd} order stimulated anti-Stokes rotational Raman lines from the first 1^{st} order anti-Stokes rotational Raman line; (c) Generation of 2^{nd} order stimulated anti-Stokes rotational Raman lines from the second 1^{st} order anti-Stokes rotational Raman line; (d) Summation of all the 2^{nd} order stimulated anti-Stokes rotational Raman lines from each of the 1^{st} order anti-Stokes rotational Raman line;

Now, we try to confirm the above assumption by taking two lines L1 and L2 as examples [Fig. 5.5(c)]. Figure 5.6 shows a sketch to explain the generation of 2^{nd} order stimulated rotational Raman lines step by step. First, both 1^{st} order Stokes and 1^{st} order anti-Stokes rotational lines are created from the laser line as demonstrated in Fig. 5.6(a). The spacing between the laser line and the first Stokes (anti-Stokes) Raman line is 6B. The comb spacing

for the rest of lines is 8B. To simplify the explanation, we ignore the amplitude distribution of all the lines and only choose the 1^{st} order anti-Stokes lines for the further generation of 2^{nd} order anti-Stokes Raman lines. The conclusion will however not be scarified by the above assumption.

As sketched in Fig. 5.6(b), the first 1^{st} order anti-Stokes rotational Raman line can create its own anti-Stokes comb, where the first 2^{nd} order line is shifted 6B away from that line. Other 2^{nd} order lines are again with equal comb spacing of 8B. It is interesting that the newly generated comb (dotted lines) is just shifted from the original comb (solid lines) by 6B. Similarly, the second 1^{st} order anti-Stokes rotational Raman line can also create its own 2^{nd} order anti-Stokes comb as shown in Fig. 5.6(c). The same process can be repeated until the last 1^{st} order anti-Stokes line. Then, by adding all the combs together, the 2^{nd} order anti-Stokes comb has its highest amplitude for the last line L2 at its right side.

Similarly, a 2^{nd} order Stokes comb with its highest amplitude for the line L1 can also be generated. Since it is always more efficient in the generation of Stokes comb, the amplitude of the Stokes comb should be larger than that of the anti-Stokes comb. Using the same concept, another two 2^{nd} order combs can also be found to the Stokes side of the laser line. Indeed, the above analysis matches very well with the experimental observation, which corroborates our assumption. It should be mentioned that we have also taken other rotational spectra associated with higher order vibrational Stokes and anti-Stokes lines. We will not show them here again since similar features as demonstrated above have been observed.

Backward stimulated Brillouin scattering

Besides the forward emission, we have also investigated the backward emission, which is always desired for remote application. So far, the only detected stimulated backward signal has been identified as the backward stimulated Brillouin scattering from atmospheric pressure air. The spatial profile of the backward emission presented in Fig. 5.7 has only

been recorded when the pump energy is above a certain value, which is the feature of a stimulated process. The spectrum of the backward emission confirms it to be SBS signal. There are different studies that utilize the Brillouin shift as the tool for sensing application. It however requires very high spectral resolution detection setup. In our case, the spectral shift of SBS signal from the the pump laser wavelength is still too small to be identified, even with the high resolution spectrometer. The much weaker signal from spices with low concentration sets another difficulty in remote sensing application. This issue can hardly be resolved with SBS, but can be overcome by the impulsive stimulated Raman scattering.

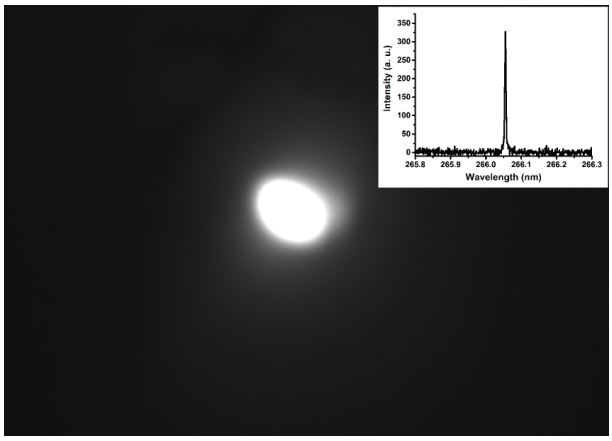

Figure 5.7: Spatial profile of the backward stimulated Brillouin scattering excited by the UV filaments from atmospheric pressure air. The spectrum shown in the inset confirms that the backward signal is SBS.

5.1.2 Impulsive stimulated Raman scattering excited by NIR filaments and probed with weak UV pulses

In sensing application, the particular pollutant under investigation usually has very small concentration. The strong Raman signal from Nitrogen and Oxygen would possibly overshadow the spectral components that are of interest. One technique that is under investi-

gation is the possibility of selective excitation of the molecules with a properly formatted sequence of femtosecond pulses (comprised in a 800 nm filament). Only the molecular vibration or rotation in synchronism with the sequence of pulses will be excited, and will produce a more intense Raman signal. The improved signal to noise ratio in Raman detection will enable the detection of species that are in low concentration.

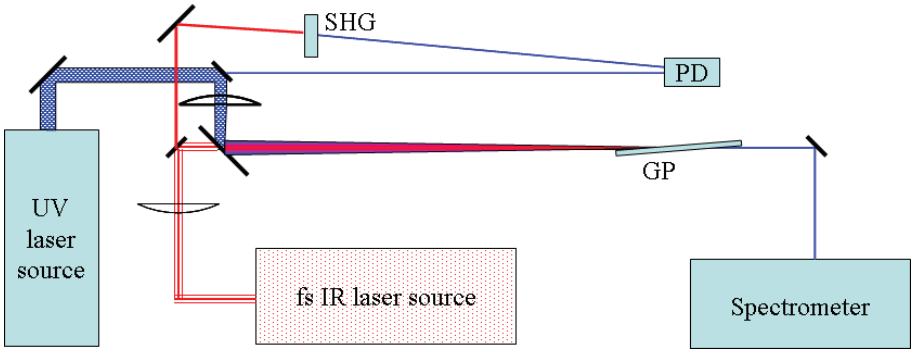

Figure 5.8: Experimental setup for impulsive stimulated Raman scattering. The UV and NIR beams are combined after passing through 3 m focal distance lenses. GP is a set of grazing incidence plates for attenuation. SHG is a LBO second harmonic generating crystal for frequency doubling the 800 nm pulses.

For preliminary study, we employ the 50 fs NIR filament with linear polarization (not a formatted sequence of femtosecond pulses yet) as the excitation source, which impulsively creates the rotational wave packets of N_2 at atmospheric pressure. Then, a temporally synchronized weak UV pulse is co-propagated with the NIR filament to probe the rotational states, which in turn creates Raman lines. The experimental setup is shown in Fig. 5.8. The UV energy used is only 20 mJ for this demonstration. The two beams are combined by a dichroic beam splitter. Several grazing incidence plates are used to attenuate the beam, before it is sent to a monochromator that has several angstrom resolution. The two lasers are synchronized electronically. There is however a ns jitter inherent to the Q-switch seeding process [21]. The timing between pulses is monitored by a fast UV vacuum photodiode, which is detecting the UV beam and the second harmonic of the NIR pulse.

Figure 5.9(a) shows the rotational spectrum recorded in the forward direction. Since

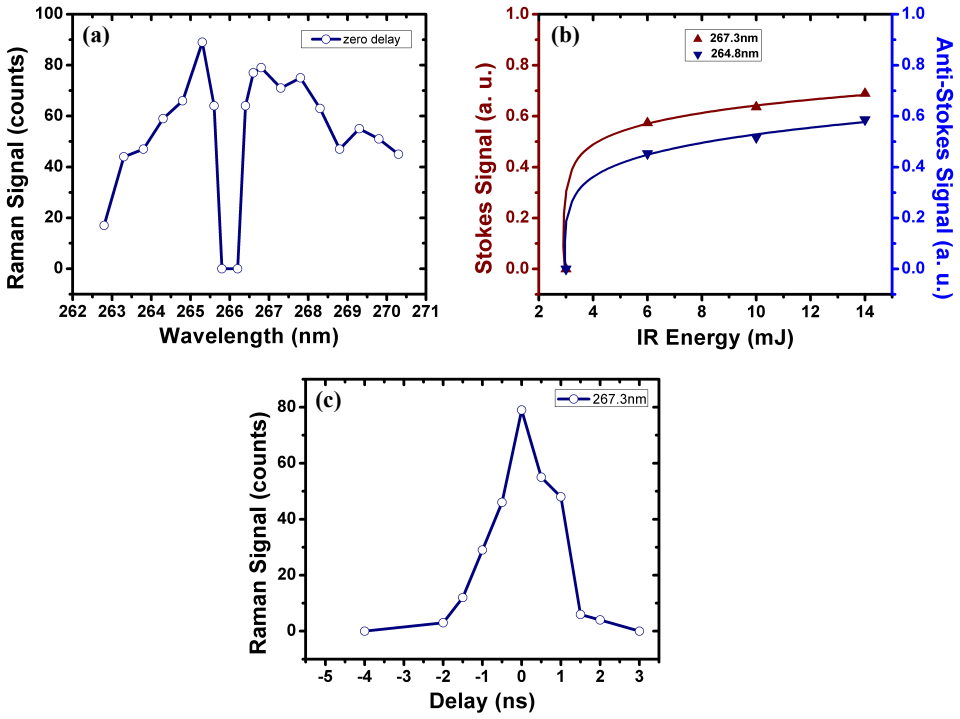

Figure 5.9: (a) Impulsive rotational Raman spectrum of nitrogen. (b) Dependence of the Stokes and anti-Stokes signals on the infra-red intensity. (c) Dependence of the signal on the relative delay between NIR and UV.

the excitation has been performed at atmospheric pressure, the Raman signal has been randomly probed by the weak UV pulse due to the fairly low Raman gain. The probed Raman signal (i.e., the shifted UV spectrum) is therefore represented by counts, instead of the intensity. Note that the UV radiation is spectrum sufficiently narrow so that there is no measurable scattering from the 266 nm laser at the two data points on either side of the laser line. The energy scan in figure 5.9(b) shows a clear threshold for this nonlinear process. We have not observed a dependence on the UV energy when it is scanned at the level of 10s of mJ. Figure 5.9(c) is a plot of the Raman signal dependence on the delay between the NIR impulse and the UV Raman pump. Because of the relatively long duration of the near-IR pulse as compared to the vibrational period of most molecules, the test experiments have

only been conducted on the rotational excitation of nitrogen. For the future experiment of selective excitation, a pulse shaper [113] or an even more complicated laser system [114] needs to be developed for the generation of pulse trains.

5.2 Highly efficient backward stimulated Raman scattering in water[7]

It has been mentioned earlier that there is large interest in generating backward stimulated Raman scattering for sensing application. It is however very hard to succeed in gases even with high intensity filaments. In liquids, the backward stimulated Raman scattering has been demonstrated short after the invention of the laser. But the conversion efficiency is often low. In this section, we report our investigation on the generation of backward stimulated Raman scattering in water with high efficiency and high energy. The new mechanism revealed here might be applied for the generation of backward stimulated Raman scattering in gases.

5.2.1 Background

Stimulated Raman scattering (SRS) was first observed in organic liquids [116,117] pumped by Q-switched pulses, and later reported from water excited by a higher intensity mode-locked subnanosecond laser [118]. It has been noticed that, using nanosecond pulses, stimulated Brillouin scattering (SBS) is the dominating process because of its larger steady-state gain coefficient as compared to the SRS process [118–120]. Recent experiments have demonstrated that the SBS efficiency could reach as high as 98% in liquid fluorocarbon [61] and 75% in water [51] provided that a single-longitudinal-mode Q-switched laser is used.

[7] Portions of this section have been published in C. Feng *et al.*, Opt. Express **23**, 17035-17045 (2015) [115]

SBS however is reduced when the pump pulse width is close or smaller than the phonon life time, due to the smaller transient SBS gain. With reduced depletion into SBS, mode-locked picosecond [121] and subnanosecond [122] pulses were employed to enhance the forward SRS. Extremely efficient forward SRS conversion up to 80% has been obtained.

Besides SBS and forward SRS, backward stimulated Raman scattering is a third process pumped simultaneously by the input laser. The early theory [123] predicts that the backward to forward SRS intensity ratio should be unity under steady-state condition. However, experiments have shown large discrepancies, i.e., the ratio is less than 10^{-2} if pumped with subnanosecond or shorter pulses [122, 124]. A ratio of more than unity has also been reported by Maier *et al.* [120], where a Q-switched nanosecond pulse (15 ns) is used to obtain a maximum backward SRS energy of 1.5 mJ from CS_2. The competition between SBS and SRS is again attributed to the suppression of backward SRS. Several factors, such as cross section difference, multimode excitation and self-focusing, appear to contribute to the backward to forward SRS ratio. Among those three, self-focusing has clearly shown its importance in changing the ratio by favoring the forward emission [125, 126]. Therefore, both SBS and self-focusing should be minimized in order to achieve better backward SRS efficiency. Based on this fact, Chevalier *et al.* [127] have demonstrated a very high backward SRS efficiency of 40% by choosing a material (i.e. acetone) with a maximum Raman gain (g) to nonlinear index (n_2) ratio, and by pumping with mode-locked picosecond pulses. It is worth noticing that the maximum backward SRS energy is obtained at the pump energy of 1 mJ. A further increase in pump intensity leads to a quick drop of the backward SRS generation, associated with an efficient build-up of filaments inside the liquid. It is concluded that the backward SRS energy is not scalable if picosecond pump pulses are used.

Other than the common competition existing between SBS and SRS, Zhang *et al.* [128] have reported the pumping effect of SBS on SRS by focusing single-mode nanosecond pulses into a liquid droplet. The droplets provide whispering gallery mode resonators for

the SBS generated from the pump laser and confine both SBS and SRS along the entire droplet circumference for maximum spatial overlap. The highly correlated spatial profiles of SBS and SRS indicates that the SRS is pumped by SBS. This is further confirmed by the temporal correlation as well as the SRS threshold measurements. Very recently, Liu *et al.* [129, 130] have extended the pumping effect of SBS on backward SRS into a more universal case of optical cell experiment. By focusing single-mode nanosecond pulses into a water cell with focused depth up to 1.8 m, the correlation on SBS and backward SRS energies is found to support the existence of pumping of SRS by SBS. A maximum backward SRS energy of 0.25 mJ, corresponding to an efficiency of 0.03%, has been achieved. It has also been shown that the backward SRS excited by the pump laser and by SBS co-exist and could not be distinguished [130].

In this section, we demonstrate backward SRS generation of high energy (4.5 mJ) and high conversion efficiency (9%) from a water cell. For the first time, a special ring-shaped backward SRS profile, which is associated with the spatial dependent pulse width distribution of pre-compressed pump pulse, is reported. We present evidence that the backward SRS results from forward pumping by backward SBS, based on different correlations between SBS and backward SRS generated from Raman cell. Our study on the evolution of filament generation in water under different pump inputs leads to an understanding of our measurements on SRS, as well as the results [120, 127] obtained earlier with pump pulses of different duration.

5.2.2 Pump source for the Raman cell

In most prior experiments of stimulated Raman scattering, the pump is produced by a standard inversion laser. The source used in the present investigation is based on backward SBS, which has been detailed in Chapter 3. The pump source for Raman generation is only a single 2.5 m long oscillator, and does not include the amplifier cell. It has been demon-

strated in Section 3.5 that the pulse width of the SBS compressed pulses is radial position dependent, as demonstrated in Fig. 5.10(a) again for the primary pump energies of 10 and 50 mJ. The energy of this SBS compressed pulse is plotted as a function of primary pump pulse energy in Fig. 5.10(b). The beam profile of the SBS generated in this cell ranges from 25 mm at 50 mJ output, to 30 mm at maximum output energy (400 mJ).

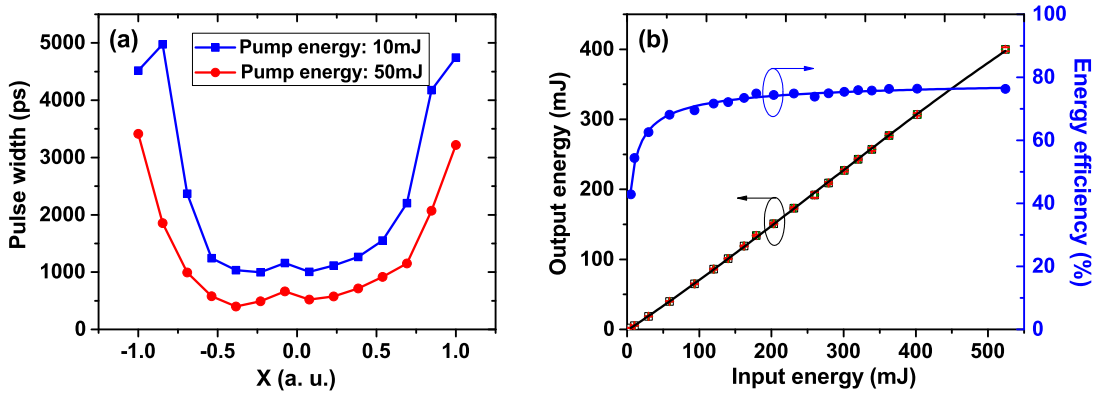

Figure 5.10: (a) Spatial pulse width distributions of the pump generated in the first cell, at the energies of 10 and 50 mJ; (b) Energy and efficiency of the SBS cell generating the pump pulse, as a function of the primary Nd:YAG pulse energy

5.2.3 Experimental setup

The experimental setup sketched in Fig. 5.11(a) includes the SBS generator described in the previous section, followed by a 54 cm long water cell (SRS cell). The pump beam is coupled out through TP2 [Fig. 5.11(a)], focused by the lens L_2 and directed by two mirrors into the SRS water cell. The latter is slightly tilted to spatially separate the backward signal and surface reflections. The polarization of the SRS pump can be manipulated with the quarter-wave plate QW2. The position of the lens L_2 is adjusted to have the focal spot at 27 cm from the entrance window, a depth chosen to match half of the spatial length of the 2 to 3 ns pulses.The coupling optics between the two cells implies a reduction factor of 2.8, hence an input diameter ranging from 9 mm at 50 mJ to 11 mm at 400 mJ. The dichroic

mirror (DM) with >99% reflectivity at 532 nm and ∼95% of transmittance around 650 nm allows the backward SRS to be coupled out and characterized. We measure the output energy, the spatial and temporal profiles for both SBS and SRS as well as the filament generated by the pump beam.

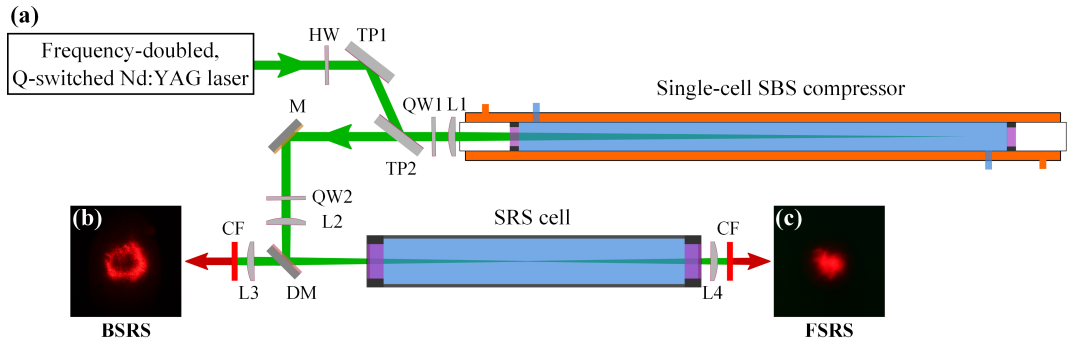

Figure 5.11: (a) Schematic of experimental setup for SRS generation. The combination of a half-wave plate HW and a thin film polarizer TP1 is used to control the energy of the pulse (the pulse radial profile is $I(r) = \exp(-2r^4/w^4)$ with w = 15 mm) focused by the lens L_1 (effective focal length of 2.2 m in water) into a first SBS cell. The quarter-wave plate QW1 makes the SBS p-polarized to transmit through the thin film polarizer TP2, to provide a pump for the second (SRS) cell. This pump is focused (lens L_2 of 50 cm focal length) onto the 54 cm Raman cell via the dichroic mirror DM. Its polarization is controlled by the quarter-wave plate QW2. Different color filters (CF) are used to block the unwanted beams after both backward SRS and forward SRS are collected by lens L_3 and L_4, respectively. Throughout the whole section, "backward SRS" refers to the propagation of the Raman radiation towards the left of the second cell. (b) Ring-shaped backward SRS profile at the pump energy of 50 mJ. (c) Typical forward SRS profile with the pump energy of more than 50 mJ.

5.2.4 Experimental results

Stimulated Brillouin scattering: energy and efficiency

The energy characteristic of the SBS generated by the compressed source differs significantly to those of nanosecond pumped SBS shown in Fig. 5.10(b). In the latter, the energy

efficiency increases monotonically to approach 76% at 500 mJ, in agreement with previous reports [47,61]. The backward SRS is observed to appear randomly at an input energy around 400 mJ (SBS output energy of ∼300 mJ) and becomes stable when the input energy exceeds 500 mJ. A similar behavior has been reported by Liu *et al.* [129]. This energy behavior of SBS generator is characteristic of steady state generation [131]. By contrast, the energy characteristic of the SBS generated in the second cell [Fig. 5.12] shows a transition from steady state at low energy to transient. Because of the compression in the first cell, the pump in the second cell is of higher power (up to 1 GW) but less energy. As a result, the energy efficiency curve shown in Fig. 5.12 saturates at a relatively low energy, to peak at 45 mJ, and subsequently drops with increasing energy. The maximum SBS efficiency obtained is only about 20%, which can be explained by the shorter pump pulse duration (closer to the phonon lifetime of 295 ns in water at 532 nm) implying a smaller backward gain and SBS energy conversion to backward SRS.

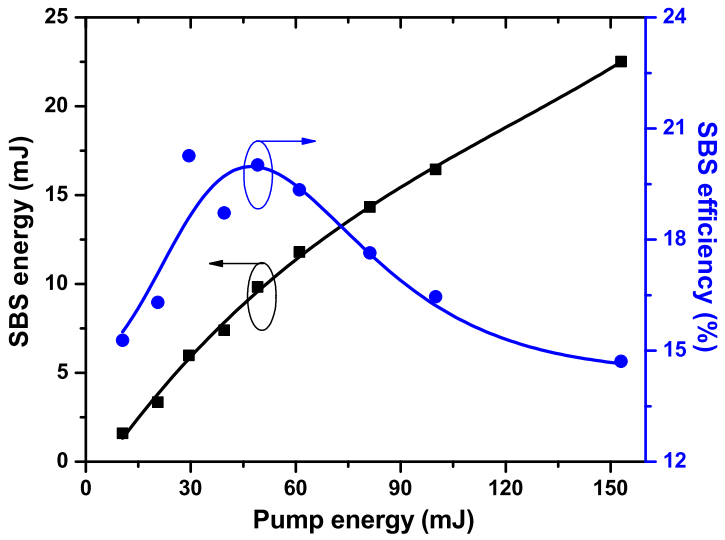

Figure 5.12: SBS output energy (left scale) and the corresponding efficiency (right scale) from the short SRS generating cell

Stimulated Raman generation: energy and stability

The pump radiation into the second cell results not only in generation of backward SBS, but also both backward SRS (with respect to the pump) and forward SRS (in the direction of the pump). Chevalier *et al.* [127] have reported that the backward SRS conversion efficiency in some materials could be enhanced by choosing circular pump polarization. Therefore, the backward SRS generations with both linearly and circularly polarized pump are compared. Figure 5.13(a) shows the SRS output energies at two different pump polarizations.

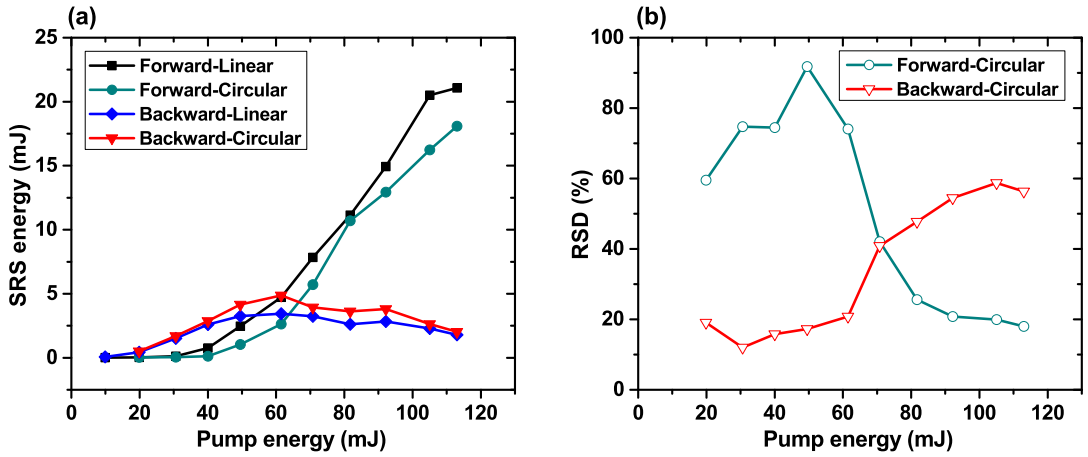

Figure 5.13: (a) SRS output energies at both linear and circular pump polarization; (b) Relative Standard Deviation (RSD) of SRS energy at circular pump polarization. Forward and backward denote the SRS propagation direction with respect to the pump; Linear and circular refer to the pump polarization.

The energy dependence of the SRS does not follow the exponential dependence shown in [132], except at the lowest pump energies. In the case of forward generation, the energy dependence of the Stokes signal turns to linear, typical of saturation. Consistent with Chevalier *et al.* [127], a larger conversion for circular polarization than for linear polarization is observed at low energies. With increasing energy, the pump pulse duration reduces, resulting in (i) a decrease in backward conversion, and (ii) filamentation, as the peak intensity of the pump pulse increases.

The SRS energy fluctuation is also measured, as illustrated in Fig. 5.13(b), for the case of circular pump polarization. Similar behavior is observed for the pump with linear polarization (not shown here). It should be noted that the maximum 532 nm pump energy used in the first cell for SBS is below the threshold (400 mJ) for backward SRS generation. Therefore, no SRS signal from the first cell is seeded into the second cell. Several observations regarding the SRS generation are worth emphasizing. First, the generation of backward SRS is more efficient and more stable than that of forward SRS when the pump energy is below a certain threshold. The same observation indicating that the backward SRS to forward SRS ratio could even be larger than 1, has also been reported in the early work of Maier *et al.* [120] where a nanosecond pump pulse is used. Next, both backward SRS and forward SRS generation are pump polarization dependent. Backward SRS generation with a circularly polarized pump is more efficient, while forward SRS shows the opposite trend. The maximum backward SRS energy and conversion efficiency achieved are 4.5 mJ and 9%, respectively, when circularly polarized pump is employed. Last, the backward SRS generation saturates around a pump threshold and drops at higher pump energy. By contrast, forward SRS generation shows a sharp increase once the pump energy exceeds the same threshold as mentioned above. Since the circularly polarized pump excites backward SRS more efficiently, further experimental measurements presented below are based on the circularly polarized pump.

Spatial profiles and their corresponding intensities

The evolution of the spatial profiles of backward SRS presented in Fig. 5.14 shows some correlation with the energy plots of Fig. 5.13. Not shown in the figure are the profiles at the lowest pump energies, between 2 mJ (threshold for backward SRS) and 10 mJ, where the backward SRS profile evolves from a single spot (2 to 5 mJ) to 2 spots (8 mJ). This evolution continues from 5 spots (10 mJ) to a increasingly large number, as seen in Fig. 5.14(a). The same observation has been reported by Chevalier *et al.* [127]. As the pump energy increases

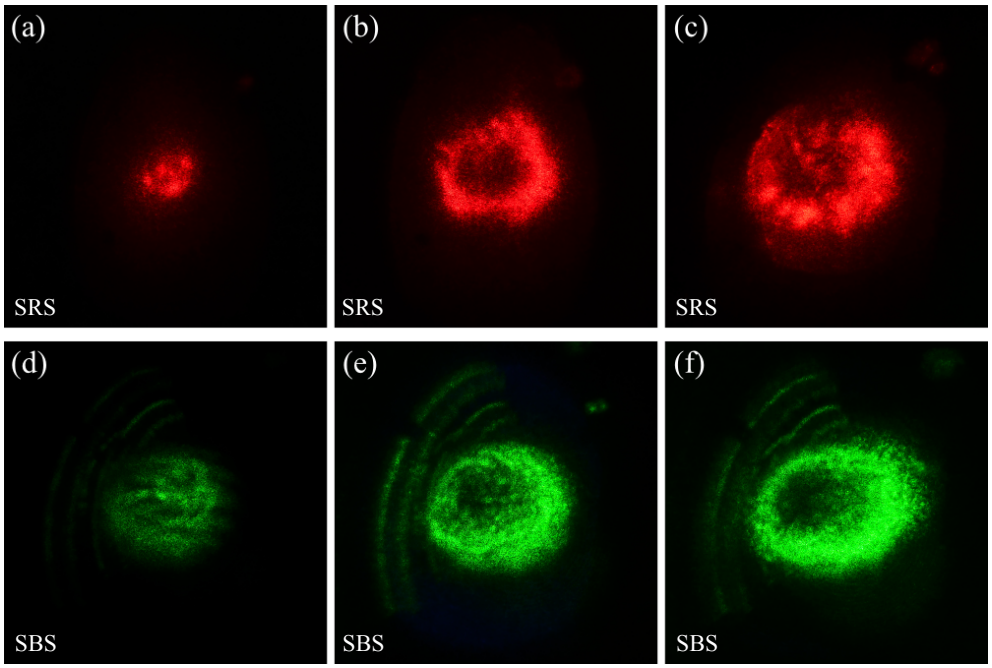

Figure 5.14: Spatial profiles of backward SRS and SBS taken with a digital camera at different pump energies; (a) and (d), 10 mJ; (b) and (e), 50 mJ; (c) and (f), 100 mJ; Fringes next to SBS profile are due to the leakage of back-scattering through the edge of the dichroic mirror.

from 10 to 50 mJ, a ring-shaped pattern appears in the backward SRS profile [Fig. 5.14(b)]. The ring shape starts to break up into spots again [Fig. 5.14(c)] with a further increase of the pump energy and the corresponding backward SRS energy also gradually drops from its maximum value. Irregular backward SRS profiles are later observed if higher pump energies ($>$100 mJ) are used.

The pump SBS itself can generate its own backward SBS signal, which then propagates in the same direction as the backward SRS shown in Figs. 5.14(a)–(c). It is interesting to compare the corresponding profiles of SBS, which are recorded in Figs. 5.14(d)–(f), with that of backward SRS. The profiles of SBS and backward SRS are highly correlated at pump energies around 50 mJ. By choosing appropriate filters to balance the contrast of green and red colors, the overlap of two rings is observed, which shows clear evidence that

the backward SRS is driven by the SBS under current experimental conditions. It is worth emphasizing that, if backward SRS were to be excited by the pump itself, the high intensity portion of the backward SRS profile should be at the beam center [see forward SRS profile in Fig. 5.11(c)], where the pump beam exhibits its highest intensity.

In addition, we have measured the ratio of the intensity of the radiation in the ring and in the center of the hole, for both SBS and backward SRS. At the pump energy of 50 mJ, this ratio in the backward SRS beam is about 3 times of the ratio measured in the SBS beam. This is to be expected, since the generation of backward SRS is nonlinearly dependent on the SBS (pump) intensity before the saturation is reached, as discussed in Section 4.2.

Spatial pulse width distributions

Measurements of the spatio-temporal profile of the pump pulse further demonstrate that the backward SBS is generating the backward SRS. A cross-section of the pulse width distribution in the pump beam at 10 mJ and 50 mJ was shown in Fig. 5.10(a). The SBS gain in the second cell is decreasing with decreasing pulse width, with the steepest dependence when the pulse duration approaches the phonon lifetime of 295 ps. The SBS reflectivity is moderate and uniform at the pump energy of 10 mJ, where the pump pulse duration remains above 1 ns across the beam. The backward generated SBS beam has a Gaussian like profile [Fig. 5.14(d)]. However, when the pump energy is increased to 50 mJ, the minimum pump pulse width reduces to be 500 ps [Fig. 5.10(a)], quite close to the phonon lifetime. The corresponding SBS reflectivity around the beam center is then dramatically lowered due to the reduced transient SBS gain. The gain remains however high on the edges of the beam, where the pulse duration exceeds 1 ns. Therefore, a ring-shaped SBS profile is formed. As a result of the increasing hole in the center of the beam, the SBS efficiency decreases [Fig. 5.12]. At increasing pump energies, the portion of the pump beam with a few hundred ps duration increases in diameter, resulting in further reduction in efficiency. This is verified by the SBS profile with a larger hole taken at the pump energy of 100 mJ

[Fig. 5.14(f)].

If the backward SRS were to be excited directly from the pump, it would have a profile with a higher intensity at the left side, corresponding to the shortest pump pulse duration seen also at the left side of the beam. However, the intensity distribution of backward SRS simply follows that of SBS beam, which exhibits less intense beam at the left side.

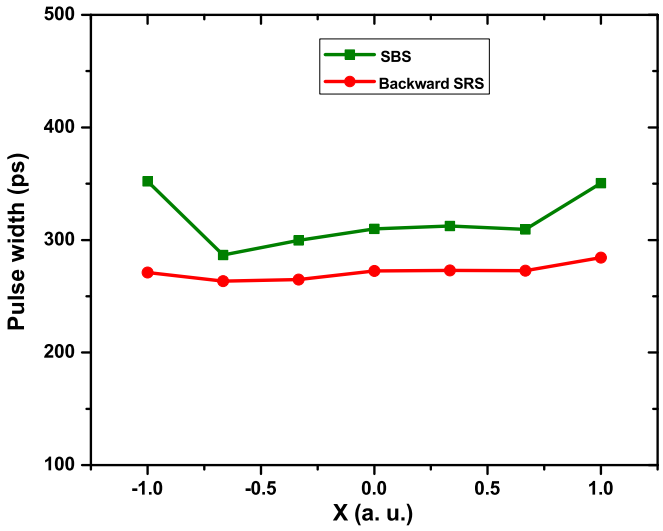

Figure 5.15: Spatial pulse width distributions: pulse width of SBS and that of backward SRS at the corresponding positions at the pump energy of 50 mJ. Due to the limited temporal resolution of the pulse detection setup (140 ps rise-time), the actual SRS pulse width could be much shorter than indicated in the figure.

The spatial pulse width distribution of SBS beam at the pump energy of 50 mJ is presented in Fig. 5.15. The horizontal axis is normalized such that the pulse width of input and output could be compared directly. Since the focused depth is chosen to match the longest pulse width at the beam edge, pulses within the whole beam area are efficiently compressed. It is worth mentioning that the shortest pulse width achieved is below the phonon lifetime, which further increases the SBS intensity. The backward SRS pulse width at the corresponding position is also measured and presented together with the SBS pulse width. The

pulse width of backward SRS is seen in Fig. 5.15 to be shorter than the SBS pulse width, which agrees to prior theoretical [130] and experimental [120] observations. The backward SRS and SBS appear to be correlated. For instance, the backward SRS shows shorter pulse width at the position where the SBS pulse width is also shorter. This provides further evidence of the pumping effect of SBS on backward SRS.

Evolution of filament generation

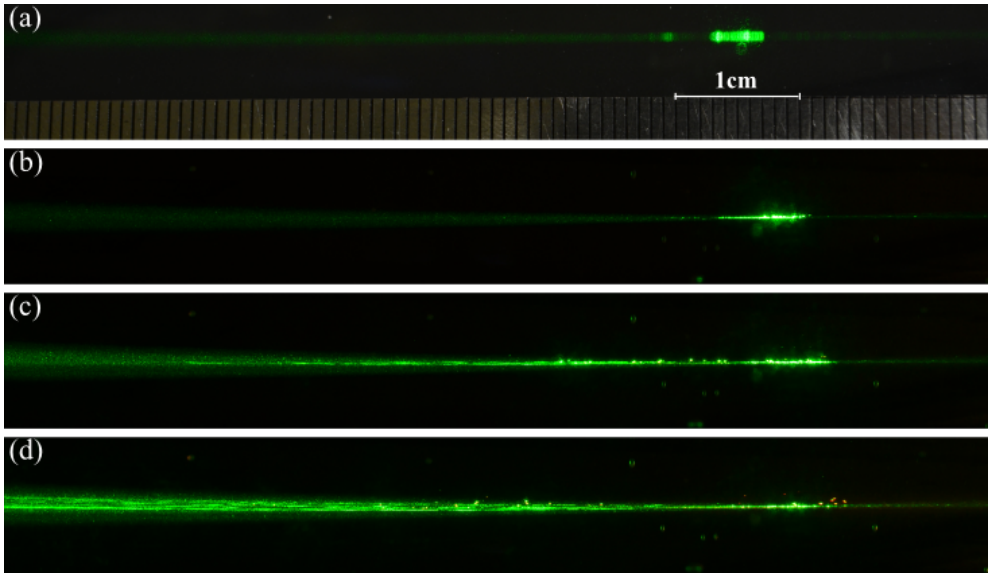

Figure 5.16: Evolution of filament generation in water under different pump energies; (a) 2 mJ; (b) 10 mJ; (c) 50 mJ; (d) 100 mJ; The pump beam propagates from left to right.

Based on the correlations existing between different parameters of SBS and SRS, we have established that backward SRS could be efficiently driven by SBS. In this section we investigate the propagation of the pump (which is the SBS from the first cell in Fig. 5.11(a)), and the evolution of the backward SRS profile. It has been shown that the backward SRS is initiated by self-focusing [120] and its evolution related to filament generation [127]. The tracks of filaments are recorded in the photographs of Fig. 5.16, for different pump energies. At low pump energy of 2 mJ, both backward SRS and forward SRS generations

are observed to appear randomly as a single small spot. As the pump energy increases, the number of backward SRS spots increases because of the generation of transversely distributed multiple filaments, which could not be resolved because of the limited spatial resolution [Fig. 5.16(b)]. At higher pump energy longer filaments are generated. As reported in [127], with increasing pump pulse energy, those backward SRS spots gradually disappear or become irregular areas. As mentioned in the previous sections, the ring-shaped SBS also starts to build up and excites the backward SRS, giving it a similar profile. At the pump energy of 50 mJ, only two main filaments [Fig. 5.16(c)] [8] are shown to co-exist inside the beam center area, which ensures the generation of a regular ring shape. However, more filaments [Fig. 5.16(d)] are at the beam edge with even higher pump energy. Spots are observed again within the ring-shaped backward SRS profile [Fig. 5.14(c)]. The backward SRS energy also drops since the forward SRS generation is enhanced by the filament generation. Because of the competition existing between backward SRS and forward SRS, the stability of their energies thus shows opposite tendency.

5.2.5 Optimization of the conversion efficiency in Raman

In this section we analyze the factors influencing the efficiency and high energy conversion into backward SRS, based on our data and those of [127, 129]. Our understanding of the mechanism of SRS generation leads to the conclusion that it is only possible to meet the conflicting requirements of high energy and high efficiency to backward SRS in a setup with multiple cells.

All observations converge to the conclusion that, in the backward direction, SBS is the primary and more efficient mechanism, and is a source of SRS in the same direction. The first element of the cascade pump SBS – backward SBS — SRS requires high efficiency and efficient compression of the pump SBS. Intensity enhancement could readily be satisfied

[8] Those two filaments might not be well distinguished due to the limited resolution.

since the SBS process is well known for its application in pulse compression [52]. In order to achieve best intensity enhancement, i.e., single compressed pulse and high energy efficiency, a focused depth (of the pump) of $\geq$1 m inside the medium is typically required to match half to full of the spatial length [$c\tau_p/n$, where τ_p is the pulse width (FWHM) and n is the index of refraction of the SBS medium] of the single-mode nanosecond input pulse. After the focused depth (f) is chosen, a small f-number (f/D) therefore a large input beam diameter (D) is also needed to keep the Rayleigh range small such that the point, where SBS starts to build up, is less dependent on the pump energy. Both larger f-number and higher pump energy tend to move the SBS build-up point towards the entrance, which equivalently reduces the focused depth and therefore lowers the efficiency of intensity enhancement. The generated backward SBS is amplified towards the cell entrance, to reach its maximum intensity near the peak of the pump, which, given the optimum design configuration for SBS, is close to the entrance window [64]. This is the region where the SRS is effectively generated, which happens — counter-intuitively — to be where the beam size is the largest. This explains the previous observation that backward SRS could barely be observed when the focused depth is short [129], and that a single-cell setup cannot drive very efficiently backward SRS generation.

A multiple-cell setup makes it possible to pre-shape the pump SBS pulse for optimum backward SRS generation. In the two-cell configuration presented here, a pre-compressed pulse ($\leq$3 ns) serves as pump in the second cell, resulting in a much faster accumulation of SBS energy than in the case of a $\sim$10 ns pump pulse (as is the case in a single-cell setup [129]). Therefore, the SBS intensity reaches backward SRS threshold much earlier. Another advantage of the two-cell setup is that small beam diameter of 9 mm, which is defined by the f-number and focused depth chosen for the second cell, requires much less energy to obtain the same intensity as achieved from single-cell setup. As a result the energy efficiency could be dramatically enhanced. Last, the compressed SBS pulse width could reach below the phonon lifetime with a two-cell setup design [53], which further enhances the SBS intensity to drive backward SRS more efficiently.

There are different configurations and liquids to be used depending on the energy to be achieved in the final process. For instance, if the initial pump energy of the first cell is highest, a liquid of small Brillouin gain, such as water, will be chosen to create a high energy SBS. This pump SBS could further be scaled up using a SBS amplifier cell, as demonstrated in [51, 52]. In the final cell for Raman generation, the efficiency can be optimized by a judicious choice of liquid with high Raman gain coefficients [121].

5.2.6 Summary

In this section, we have demonstrated efficient backward SRS generation from an optical cell driven by intense SBS, by exploiting a two-cell setup. The mechanism of backward SRS generation is interpreted as being a forward Raman process pumped by a backward SBS. Since the UV filament can excite the backward SBS, it is possible to employ the mechanism explored here to generate backward stimulated Raman scattering in air for further remote sensing application.

5.3 Application of filaments for Laser Induced Breakdown Spectroscopy (LIBS)

The application of filaments for remote sensing by employing Laser Induced Breakdown Spectroscopy (LIBS) technique has been firstly demonstrated with femtosecond NIR filaments [92, 133], and later with sub-ps UV filaments [134]. It gains continuous attentions [135–138] and has been very recently applied for the isotopic analysis of zirconium (Zr) samples [139]. As mentioned earlier, NIR filaments always exhibit continuum generation, which will add a strong background to the emission spectrum thus lower the signal to noise ratio. To overcome this issue, it has been demonstrated that a telescope system needs to be employed to create short filaments thereby less continuum generation. Even though

the proposed solution allows non-gated measurement for a sample placed 50 m away from the femtosecond laser source together with the detection system [140], it becomes less practical when the sample is located further away since the generation of filament becomes less controllable at a far distance. In this section, we demonstrate that the long pulse UV filament induced breakdown spectroscopy is almost free of the background issue. Therefore, the UV filament better suits the LIBS experiment with non-gated detection. Then, we report our investigation on the dynamics of self-absorption in LIBS, which requires gated measurements.

5.3.1 Experimental setup

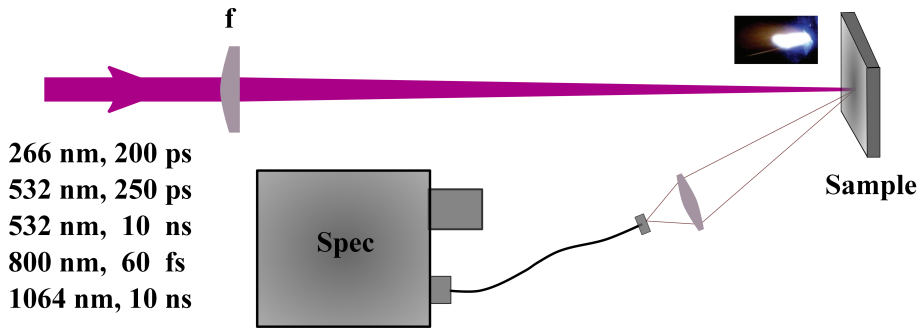

Figure 5.17: Experimental setup for the investigation of Laser Induced Breakdown Spectroscopy. The focusing lens has focal length of f=1500 mm. The inset shows a picture of the plume created by the high intensity laser ablating the solid sample.

The setup used for the LIBS experiments is sketched in Fig. 5.17. To investigate the dependence of the self-absorption dynamics on different laser parameters, we have employed nanosecond and sub-nanosecond laser pulses from the laser system described in Chapters 2 and 3, as well as femtosecond pulses from a Ti:Sapphire oscillator amplifier system. So far, we have focused on solid samples such as Copper (Cu) and Aluminum (Al). For the non-gated detection, a Czerny-Turner monochromator combined with a Hamamatsu Photomultiplier Tube (PMT: Model R212) has been employed for the spectrum analysis. Since

the spectral resolution is not so stringent in this case, the scanning step size is set to be 0.5 nm. The DEMON spectrometer as mentioned earlier has been utilized for the gated measurements.

5.3.2 Non-gated LIBS with UV and NIR filaments

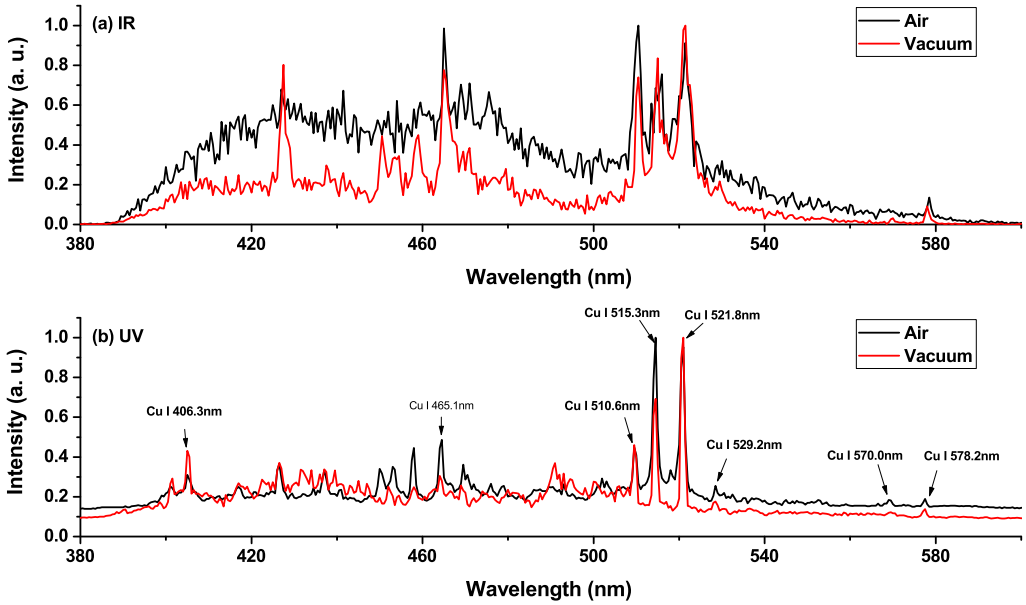

Figure 5.18: Comparison of the non-gated LIBS with Cu sample when filamented and non-filamented NIR (a) and UV (b) pulses are employed. Each spectrum is normalized to their own maximum and averaged over 4 laser shots. Cu I denotes ion Cu^{+}.

The non-gated LIBS experiments have been performed with both UV and NIR (15 mJ, 60 fs) lasers. A sealed box has been used to hold the sample (either Cu or Al) such that the LIBS experiments can be carried out under either atmospheric pressure or vacuum condition. Normally, a filament can not be formed under vacuum condition. Therefore, we are also comparing the LIBS results with and without filament formation. Figure 5.18 presents the LIBS spectra from Cu obtained with different conditions. When NIR filament is employed, a strong continuum is present in the LIBS spectrum [black curve in Fig. 5.18(a)],

which lowers the signal to noise ratio (SNR) and even obscures several emission lines. Those lines can only be observed under vacuum condition, where there is no continuum emission since there is no filament.

On the contrary, the LIBS spectrum [Fig. 5.18(b)] shows much better SNR when either UV filaments or non-filamenting UV pulses are utilized. Due to the different SNR, several weak lines (i.e., 406.3 nm, 529.2 nm and 570 nm) can only be captured with the UV filaments but not with the NIR filaments. Similar behavior has also been observed in the investigation of explosives [10]. Therefore, we conclude that it is advantageous to perform the non-gated LIBS measurement with UV filaments where no extra control is required.

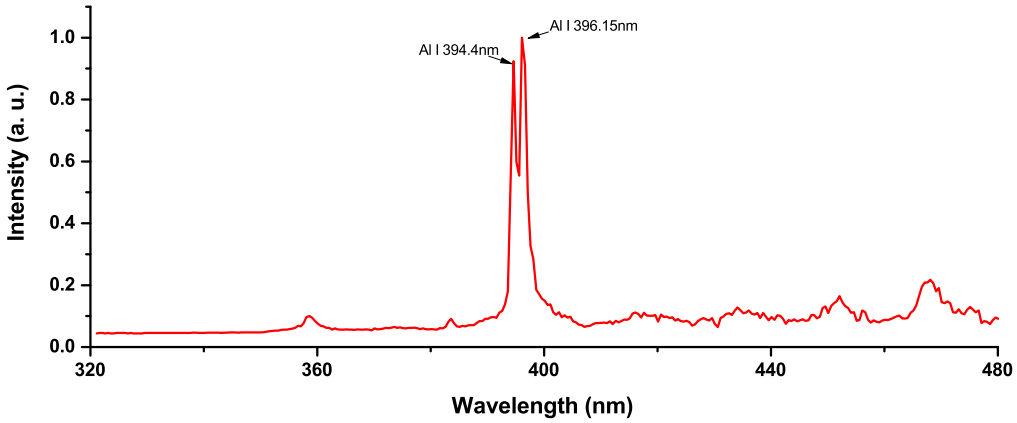

Figure 5.19: Non-gated LIBS spectrum from Al sample with UV filaments as the exciting source. The normalized spectrum is averaged over 4 laser shots. Al I denotes ion Al^{+}.

The same comparison has been made with the Al sample with similar outcome. Figure 5.19 illustrates the typical LIBS spectrum centered around 400 nm that is generated with UV filaments and taken with the Czerny-Turner monochromator. Two main peaks at 394.4 nm and 396.15 nm represent the transitions from different excited states to the ground state of neutral atoms. In the next section, we focus on the emission line at 396.15 nm and investigate the dependence of self-absorption dynamics on the plasma temperature, which is closely associated with the laser parameters.

5.3.3 Dynamics of self-absorption in Laser Induced Breakdown Spectroscopy

Self-absorption is a well-known phenomenon in LIBS and mainly observed for transitions where the lower level is the ground state of the atom, as explained in [141]. For single atoms, the wavelength of emission and absorption are identical. Atoms in the cooler outer part of the plume can therefore absorb the radiation that is emitted by atoms in the hot inner part. A broader emission line from the hot part of the plasma will therefore be superposed by a narrower absorption line as shown in Fig. 5.20. Consequently, the occurrence of self-absorption can yield information about the temperature distribution in laser-generated ablation plumes. Since the laser ablation process involves two interactions, i.e. laser-sample and laser-plasma interactions, with the latter being much dependent on the laser parameters such as wavelength, the evolution of self-absorption is expected to be excitation laser source dependent.

We investigate laser-induced spectra using five different lasers, which have been listed in Fig. 5.17, as excitation sources. Spectra were obtained with the DEMON spectrometer. Among the various target investigated, the data presented here are for the emission line at 396.152 nm of Aluminum 6061. This emission line corresponds to a transition from $3s^2 4s$ to the ground-state level $3s^2 3p$ [142], which shows self-absorption, of which we investigate the dynamic behavior.

The main behavior of the spectra observed with the first four lasers listed in Fig. 5.17 is shown using the example of the 266 nm pulses in Fig. 5.20(a). For a delay of 1000 ns, we see the typical broadband emission with the narrower self-absorption dip at exactly the resonance wavelength. Attempting to find the beginning of the self-absorption, we decreased the delay to 250 ns until we observed the remains of the plasma continuum emission. Even here, the self-absorption can be recognized.

Figure 5.20(b) shows a completely different behavior when a 10 ns laser pulse at 1064

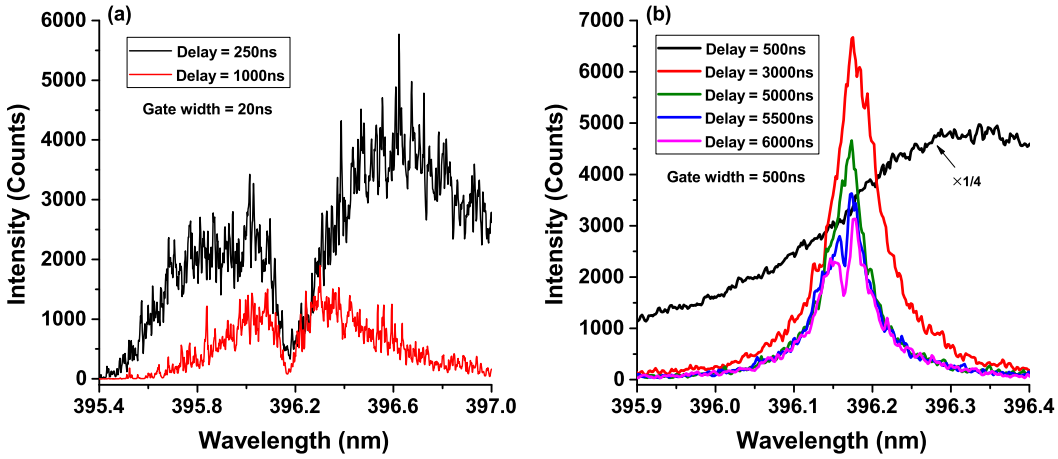

Figure 5.20: Gated LIBS spectrum of an aluminum sample excited with (a) 266 nm and (b) 1064 nm lasers with different delays between laser pulse and ICCD gate. The emission line amplitude and the dip width decrease with increasing delay.

nm is used for ablation. After the plasma emission has stopped, at lower delay times, only the emission of the hot parts of the ablation plume can be seen. For longer delays, this emission line becomes narrower (due to the plume cooling down) and at around 5 μs, the self-absorption dip appears. As compared to the previous case of using shorter wavelength excitation lasers, the self-absorption dip builds up much later. The difference in build-up time can be explained by the different structure of the laser-generated plasma, which has significantly higher initial temperature due to the larger heating by inverse bremsstrahlung at the infrared wavelength, therefore takes longer to form a cooler outside layer. It is worth mentioning that the absorption dip observed here is as narrow as 15 pm, hereby demonstrating the potential resolution of absorption dip LIBS.

Besides the laser wavelength dependence, we have also observed the evolution of the absorption dip with respect to the ablation history, as demonstrated in Fig. 5.21. When a fresh sample is ablated with the 266 nm laser pulses, the LIBS spectrum obtained at a short delay of 250 ns exhibits strong continuum at the very beginning. As the ablation continues, the continuum spectrum decreases and the self-absorption dip appears and further develops.

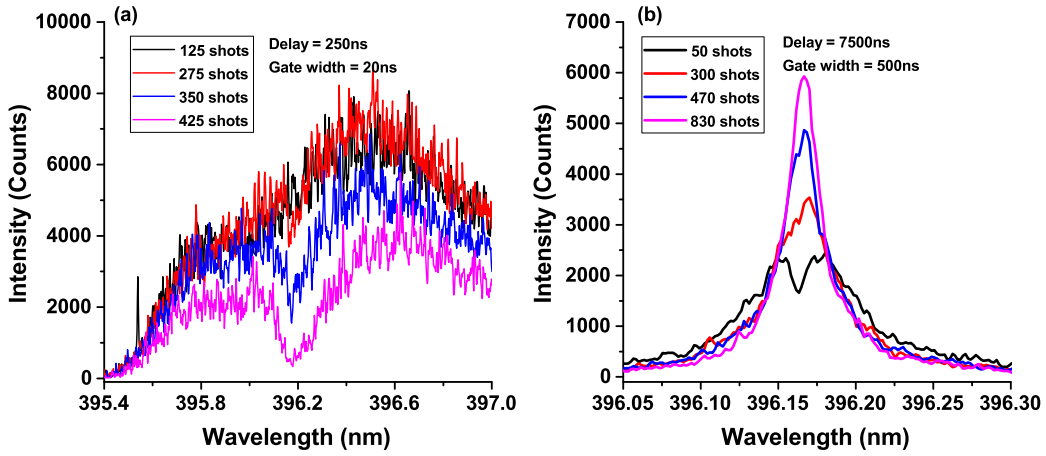

Figure 5.21: Gated LIBS spectrum of a fresh aluminum sample excited with different numbers of (a) 266 nm and (b) 1064 nm laser shots.

In the case of the fresh sample being ablated with 1064 nm laser pulses, the LIBS spectrum obtained at a long delay of 7500 ns evolves the opposite way. The self-absorption dip exists for the early laser ablations. It however disappears after some laser shots. In the meantime, the emission line also gets stronger as well as narrower, as shown in Fig. 5.21(b). The full width at half maximum of the emission spectrum after 830 shots of laser ablation is as narrow as 28 pm. A similar behavior has also been observed for longer delays of 9500 ns, in which case it takes more laser shots to erase the self-absorption dip.

More experiments are necessary to fully explain this behavior. However, a tentative explanation is the following: With 266 nm excitation source, the spectrum captured with short delay of 250 ns is dominated by the plasma emission at the beginning of laser ablation. After some laser shots, a geometric structure (e.g. a dip) is created, which leads to less efficient ablation process thereby less plasma generation and continuum emission. The decrease in continuum spectrum is also confirmed by the reduction of visible white light emitted from the plume during the ablation process. Then, the self-absorption dip becomes visible and further develops as the ablation continues. In the case of 1064 nm laser pulses being employed, the similar geometric structure created after some laser shots

would confine the hot plasma. It then needs longer time for the plasma to expand and form the cool atoms at the outside layer. Therefore, the self-absorption dip disappears at the delay of 7500 ns after a period of ablation. With the same sample, the dip will be found to appear at longer delay, which has been confirmed by our measurement.

5.3.4 Summary

Self-absorption in LIBS experiments exists immediately after the excitation when shorter wavelengths are used. These lasers generate a cooler plasma which contains a sufficient amount of atoms in the ground state that can absorb the emission of the hotter parts at all times. For hotter plasmas, as generated with an infrared laser, self-absorption is not immediately apparent. After some time, when the cloud of atoms has sufficiently expanded and cooled, the self-absorption dip appears. The evolution of self-absorption dip with respect to the ablation history, which has been observed for both short and long wavelength excitations, are all associated with the geometric structure created by the laser ablation.

Chapter 6

Long-gap DC high-voltage discharge induced by UV filaments

6.1 Introduction

The investigation on laser-induced high-voltage discharge has started since 1970s [143–145]. The idea behind is to use the powerful laser pulse to create a plasma channel via photo-ionization, which provides a preferential discharge path and also initiates the discharge with lower breakdown voltage or electric field. Such investigation can be applied for lightning control, as proposed in [146] in 1974.

In the early studies, the powerful nanosecond pulses from Q-switched Nd:glass [143, 144] or CO_2 [145, 147] lasers are often employed. Since their lasing wavelengths are above 1 μm, spatially isolated plasma beads that have been discussed in Chapter 4 are easily created, due to the strong inverse Bremstrahlung effect. It has been confirmed that only a continuous ionization channel, rather than the plasma beads, is responsible for the laser-induced discharge [144]. It is therefore necessary to search for long and continuous plasma column that can eventually be applied for the long-gap laser-induced discharge.

In 1995, short after the discovery of laser filament in air, the UNM group has proposed and experimentally demonstrated the high-voltage discharge guided by femtosecond ultraviolet laser filament [11, 148]. Since the continuous plasma channel created by laser filament is ideal for laser-induced discharge, after the pioneer work done at UNM, there have been intensive investigations on NIR filament induced high-voltage discharge (a few examples [13,14,149–151]). In the meantime, there are only a few works that have investigated the discharge induced by either nanosecond UV pulse at 248 nm [152] or femtosecond UV filament at 400 nm [153]. It has however been shown by the latter study that, with one order of magnitude less input energy, the UV filament has comparable ability to induce the high-voltage discharge as that of the NIR filament. Therefore, our long pulse UV filaments fit ideally into the application of laser-induced discharge.

Knowing that the plasma channel created by the filament is suitable for discharge application, its short lifetime however sets a limit in supporting laser/filament-induced/guided long-gap (>10s cm) discharge. The recombination and attachment processes limit the plasma lifetime to be less than 10 ns, while it typically takes microseconds to establish a discharge. In order to have the discharge guided by the conductivity of the plasma, photo-detachment is required to revive the plasma channel by pealing off the electron from O_2^-. The idea of using extra laser pulses of long duration (1 μs) has been proposed from our early works [11,12,154]. Later, many studies [155–159] have focused on prolonging the filament plasma lifetime by introducing extra laser pulses of short duration (e.g., ns or fs), which are widely available in many laboratories. Even though the plasma lifetime can be extended with extra short pulses, it is still on the order of 100 ns, much shorter than the discharge build-up time. Consequently, the effect on discharge has been shown to be very limited, when a second Q-switched nanosecond laser pulse at 532 nm is used to photo-detach the electrons [160].

In this chapter, we report our investigations on long-pulse UV filament-induced DC high-voltage discharge. We show that it is very effective to trigger a discharge with the UV

filaments. In order to further increase the length and density of the plasma column created by the UV filament, another two pulses are employed, where a 0.65 J 10 ns frequency doubled Nd:YAG laser at 532 nm is chosen to photo-detach the electrons from O_2^- and O^-, while a second 1.1 J 10 ns Nd:YAG laser at 1064 nm is utilized for plasma heating via inverse Bremstrahlung effect. As will be demonstrated below, no clear effect on the discharge has been observed by adding extra short laser pulses. It therefore suggests that our initial proposal of using long pulses with duration at the same order of the discharge build-up time is necessary, if long-gap filament-induced high-voltage discharge is desired.

6.2 Experimental arrangement

The high voltage discharge chamber is located on the roof of the CHTM building. The laser beams are combined in the laboratory and sent into the HV facility via several mirrors

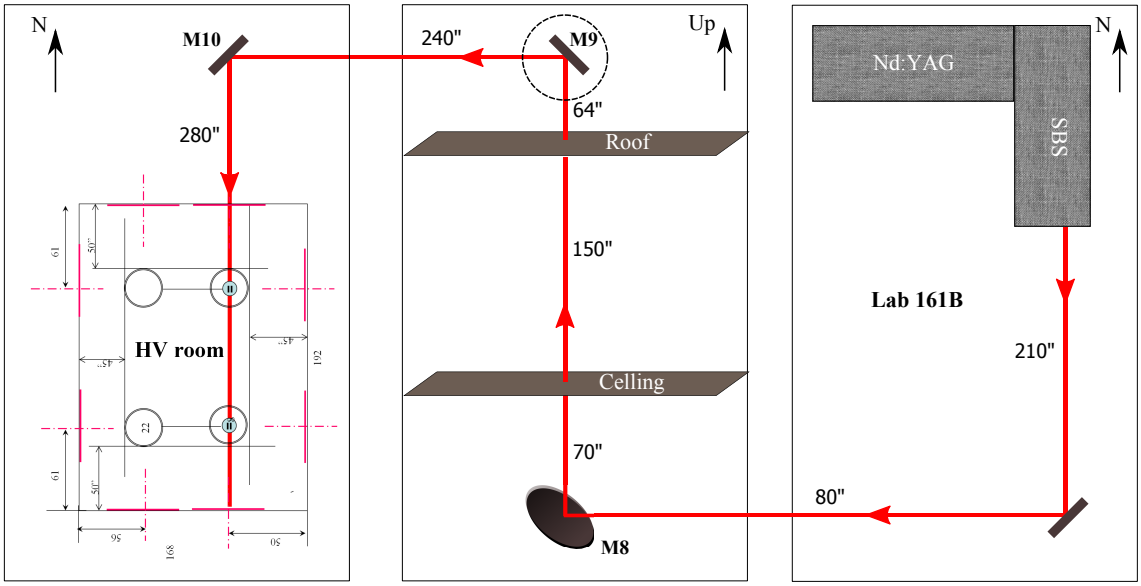

Figure 6.1: Discharge experimental arrangement for the lasers and high-voltage room; Mirrors M8-10 will be described in detail below.

that reflect all three wavelengths (266 nm, 532 nm and 1064 nm). Figure 6.1 presents the arrangement of both laser and high-voltage facilities for the discharge experiment. The distance between the UV laser and the high-voltage room is about 30 m.

6.2.1 Combination and propagation of three laser beams of different wavelength

The combination of three laser beams with different wavelengths requires both spatial and temporal alignment. The temporal alignment can be easily achieved by firing the Q-switches of the three lasers with the desired timing. The spatial alignment is however a little challenging since the transverse overlap is required even after 30 m propagation. Moreover, the longitudinal (i.e., beam focus position) overlap needs also to be fulfilled since high intensity beams are necessary for the photo-detachment and plasma heating.

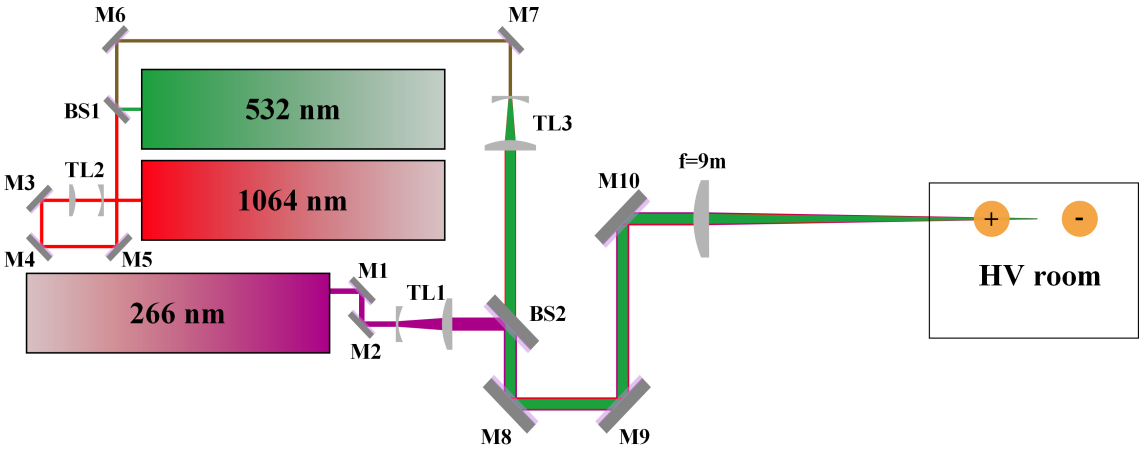

Figure 6.2: Combination and propagation of three laser beams into the HV room; M1-2: 45^o 266 nm HR mirrors; M3-5: 45^o 1064 nm HR mirrors; M6-7: 45^o 1064 and 532 nm HR mirrors; M8-10: 45^o 1064 and 532 and 266 nm HR mirrors; BS1: HR 532 nm and HT 1064 nm beam splitter; BS2: HR 266 nm and HT 1064 and 532 nm beam splitter; TL1: Telescope with magnification of 2.7; TL2: Near afocal telescope with magnification of 1.13; TL3: Telescope with magnification of 7; All the telescope lenses are uncoated fused silica.

Figure 6.2 shows the schematic for the beam combination. The 1064 nm and 532 nm beams are first combined with a beam splitter BS1 and expanded by the telescope TL3. Next, those two beams are combined with the expanded UV beam after a second beam splitter BS2. Last, all three beams with the diameter of 3" are reflected by three mirrors M8-10 and focused to the middle point of two electrodes with a 9 m focusing lens. In order to bring the geometric focus of the three beams together, telescopes TL1 and TL2 are used to adjust the divergence of the 1064 nm and 532 nm laser beams, respectively, such that the large chromatic aberration of the focusing lens can be compensated. It should be mentioned that the UV beam experiences 30% of optical losses from three uncoated lenses and three mirrors (M8-10). Therefore, the UV energy delivered into the HV room is about 210 mJ.

6.2.2 Characterization of UV filaments employed for discharge experiment

It has been mentioned in Chapter 4 that multiple filaments are created with a 9 m focusing lens in the open environment. Here, we present more details on the characterization of the filament profile and the conductivity of the plasma channel, which is essential for the laser-induced discharge.

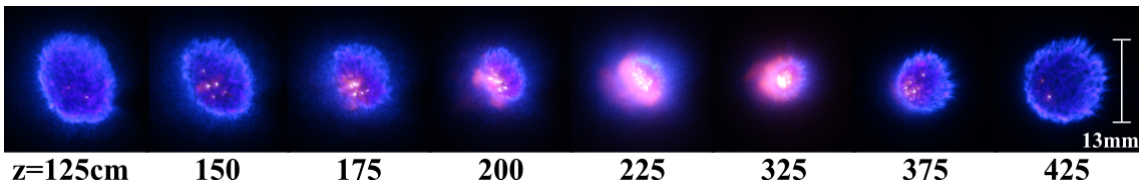

Figure 6.3: Evolution of multiple filaments with respect to the propagation distance. The filaments are generated by focusing the high power UV beam in air with a 9 m focal length lens.

A digital camera is used to take pictures of the UV laser beam profile that is presented

on a white paper. The distances under the images are with respect to the entrance point of the HV room. As illustrated in the images in Fig. 6.3, the multiple filaments last for more than 3 m.

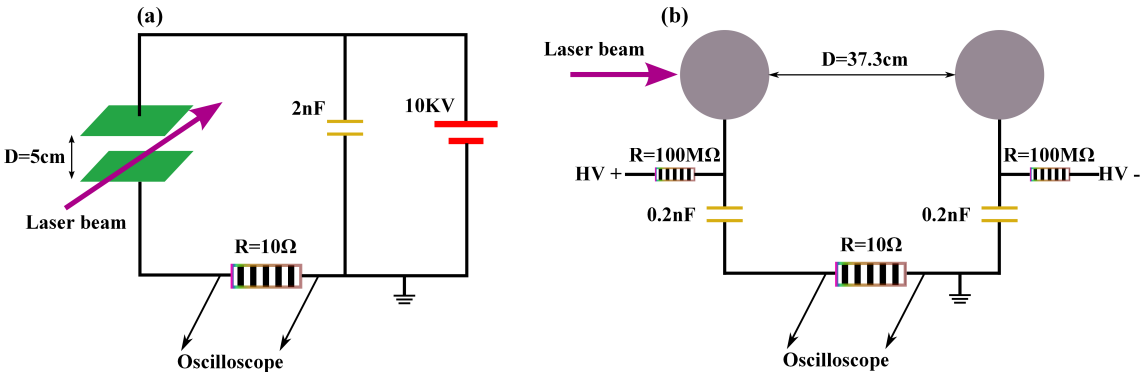

Figure 6.4: Experimental setups for measuring the resistivity of the plasma channel; (a) Setup for spatially resolved measurement; (b) Setup for spatially averaged measurement.

Two different electric circuits, as shown in Fig. 6.4, are employed for measuring the conductivity of the plasma channel that is created by either only the UV filament or UV filament plus other two laser beams. The first circuit is used to spatially (i.e., along filament propagation direction) resolve the conductivity of the plasma channel, while the second one measures the spatially averaged conductivity of the plasma channel of 37.3 cm length, which is the gap distance between the two electrodes for later discharge experiment. The current waveform is converted to a voltage waveform across the 10 Ω resistor and recorded by the oscilloscope. The peak value of the voltage waveform is used to indicate the conductivity of the plasma channel.

Figure 6.5(a) presents the conductivity measurement spatially scanned along the filament. The distance is the same as defined for the filament profile measurement. Two groups of data, i.e., one for the case of only with UV filaments and the other for case of UV filaments plus the other two lasers temporally overlapped with the UV pulse, are compared. It can been seen that no significant increase in plasma conductivity has been introduced, by adding another two laser beams. Other combination of different delays for

the two nanosecond pulses have also been tested with similar conclusion.

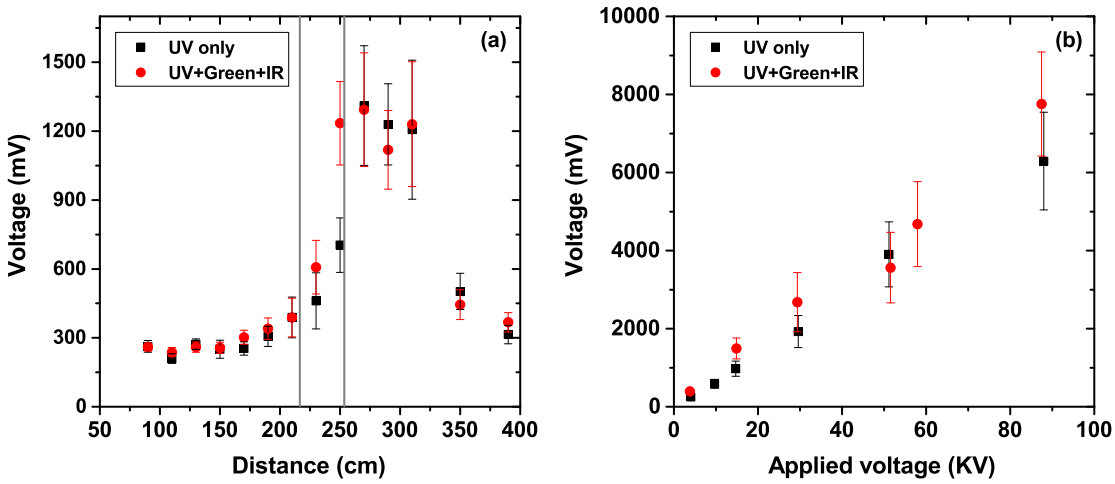

Figure 6.5: Conductivity measurements of the plasma channel created by the multiple filaments; (a) Spatially resolved measurement; (b) Spatially averaged measurement.

For the spatially averaged measurement, the two electrodes are placed at the positions labeled by the two gray lines shown in Fig. 6.5(a). The applied voltage represents the total voltage, which is twice the voltage applied on each electrode. As shown in Fig. 6.5(b), the measured signal is linearly proportional to the applied voltage. The effect of adding additional short pulse lasers on the conductivity is again shown to be very limited. The resistance per unit length of the plasma channel can be calculated to be around 5 KΩ/cm, which is remarkably lower than 1 MΩ/cm measured during a recent similar experiment with NIR Filaments [161]. Therefore, the conductivity of the plasma channel created by the UV filaments is much higher than that of the plasma channel generated with the NIR filaments. This is consistant with the result reported by Liu *et al.* [153] that the UV filament has much higher capability in inducing high-voltage discharge.

6.2.3 High-voltage facility

Both photograph and schematic diagram of the arrangement of the discharge circuit are shown in Fig. 6.6. Two steel spheres (16" diameter) are used as electrodes and the laser beams pass through holes in both positive and negative electrodes. Two capacitor banks with equal capacitance of 0.2 nF are used for charging the electrodes. The capacitor banks are designed for minimum inductance, resulting in a discharge rise time of less than 20 ns. These capacitor banks are charged by two high voltage power supplies (PTS-300 hipots from High Voltage, Inc.) up to 300 kV with opposite polarities. The power supplies are initially designed for insulation resistance testing of dielectric materials, in which case the leakage current is very small. Because of that, the controller has a safety relay that shuts down the 300 kV power supply whenever the detected current is above the rated value of 5 mA. As will be shown below, the typical discharge current in our case is hundreds of Amperes. Therefore, extra capacitor banks are needed to provide the high current, other than using the high voltage power supplies directly.

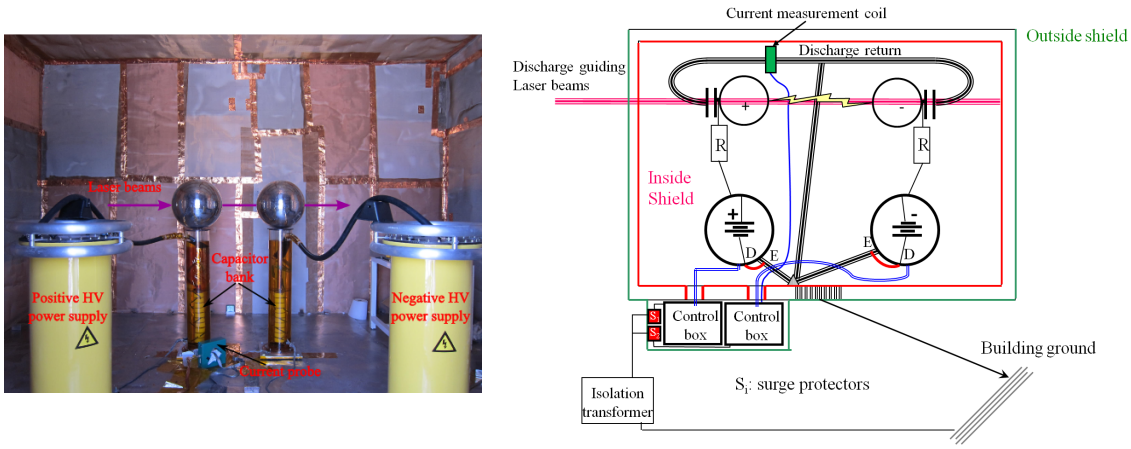

Figure 6.6: Left: photograph of the high-voltage setup; Right: schematic diagram of the circuit.

6.3 Experimental results

6.3.1 UV filament alone

We first test the high-voltage discharge induced by the UV filament itself. For the current HV setup, the self-breakdown electric field (i.e., discharge without the assistance of laser pulse) is measured to be 24 KV at an inter electrode distance of 10 cm. With the help of the UV filament, the minimum electric field needs to initiate the discharge reduces below 12 KV. The reduction of at least 50% of the breakdown electric field is more than the reported value of 20-40% in the case of NIR filament [150, 161], which confirms again that the UV filament is more suitable for the laser-induced discharge.

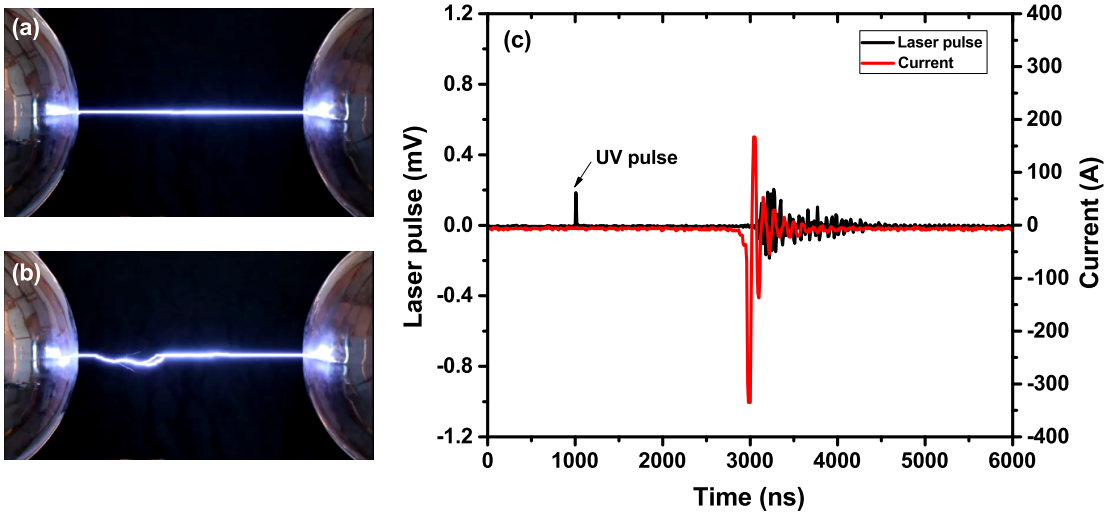

Figure 6.7: Photograph of the (a) completely guided and (b) partially guided high-voltage discharge; The gap distance between two electrodes is 37.3 cm and the applied voltage on two spheres are 170 KV and -170 KV, respectively. (c) The typical discharge current waveform recorded at 37.3 cm gap distance and 160 KV applied voltage on each sphere.

Figures. 6.7(a) and (b) show the images of either fully or partially guided discharge by the UV filament alone. For the partially guided discharge [Fig. 6.7(b)], it has been noticed

that the guided part always happens at the negative electrode side (the right side of the image). Similar phenomenon has been observed in long-gap laser guided discharge [147]. It has been explained as that the laser produced plasmas guide streamers and leaders from a negative electrode more effectively than from a positive electrode, and the discharge development from the negative electrode plays an important role in the guidance effect.

The current waveform of the discharge is monitored with a Pearson current probe. The UV pulse is also recorded before it enters into the HV room. The delay between the UV pulse and the first negative current peak, as presented in Fig. 6.7(c), is considered as the discharge delay. The delay is typically in the microsecond range. The purpose of the following experimental tests is to see if the delay can be reduced by adding extra laser pulses.

6.3.2 Combination of UV filaments with other two laser beams

As mentioned above, the objective is to reduce the discharge delay or equivalently to reduce the discharge threshold and increase the discharge probability at a specific applied voltage, by adding a 532 nm laser for photo-detachment and a 1064 nm laser for plasma heating. Different combinations of laser beams with different delays that have been investigated for the discharge of 37.3 cm are listed below.

- UV filaments alone; 532 nm laser alone; 1064 nm laser alone; combination of 532 nm and 1064 nm lasers with 0 ns delay. The total applied voltage is scanned from 250 KV to 340 KV.
- Combination of UV filaments with the delayed 532 nm pulses. The delay is scanned from 0 to 100 ns with 10 ns minimum step. At each delay, the total applied voltage is scanned from 250 KV to 340 KV.
- Combination of UV filaments with the delayed 1064 nm pulses. The delay is scanned from 0 to 100 ns with 10 ns minimum step. At each delay, the total applied voltage

is scanned from 250 KV to 340 KV.

- Combination of UV filaments with the delayed 532 nm and 1064 nm pulses. Different delayed combinations have been tested. At each delay, the total applied voltage is scanned from 250 KV to 340 KV.

During the experiments, various parameters for each set of data are recorded, such as the temperature inside the HV room, the barometric pressure, the relative humidity, the laser pulse energies, the discharge shape, the current waveform, the spectrum of the discharge plasma emission and the voltage on the electrodes. For each set of data, at least 100 data points are recorded (in other words 100 laser shots). It is worth emphasizing that the total applied voltage is always below the self-breakdown, such that the observed discharge is always being triggered by the laser beams. The probability of discharge, the average delay between the laser pulse and discharge, and the standard deviation of the delay are the main analyzed data for each set of data. All the data presented below are based on the gap distance of 37.3 cm.

First of all, we have confirmed that no discharge can be induced by the Green laser pulse alone, the IR laser pulse alone or their combination. Since there are three variables including applied voltage, combinations of three pulses and the delay between pulses, we simplify the measurements by fixing two parameters and varying the other one for each set of measurement. We start with scanning the pulse delay and fixing the applied voltage and the beam combination. Figure 6.8 presents one of the delay scan results. In this case, the total applied voltage is fixed at 340 KV and the other two nanosecond laser pulses are delayed together with respect to the UV. It can be seen that the discharge delay has very large fluctuation, which is a typical feature for all the measurements. With different optical delays, no clear improvement on reducing the discharge delay or enhancing the discharge probability has been observed. It is necessary to mention that we have closely investigated the optical delay at 80 ns, at which delay the effect might exist. However, the slightly shorter discharge delay and higher discharge probability observed in Fig. 6.8 can not be repeated

by the other measurements. The reason will be detailed below.

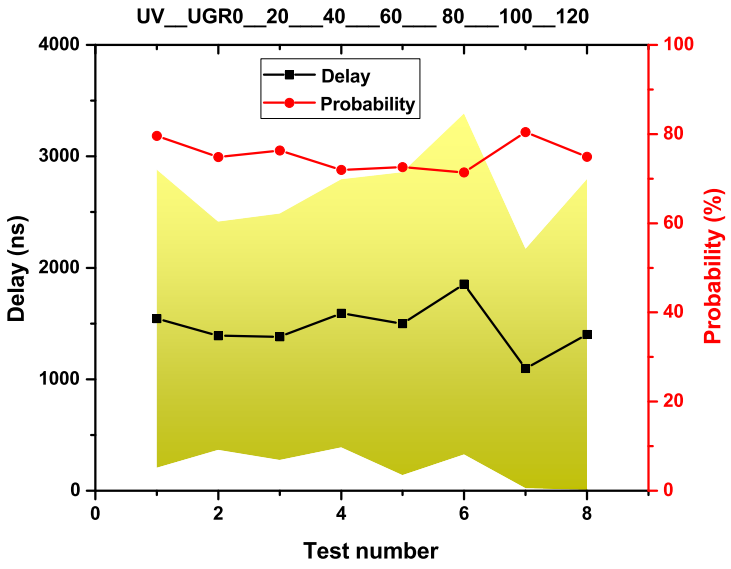

Figure 6.8: The dependence of discharge delay and probability on the laser pulse delay between the UV and the overlapped Green and IR. The optical pulse delay is labeled on the top axis, where UGR20 denotes the green and IR pulses are both delayed 20 ns from the UV. UV alone is used as a reference. The shading area represents the standard deviation of the discharge delay.

Next, we scan the applied voltage by fixing the optical delay. For each applied voltage, we also vary the combination of different beams. Figure 6.9 displays one set of the measurements taken with the optical delay fixed at 50 ns. Two expected features have been observed. On the one hand, the discharge delay decreases with the increase of the applied voltage. On the other hand, the discharge probability is increasing with the increase of the applied voltage. However, as demonstrated in Fig. 6.9, the mean discharge delay has not been clearly reduced nor the discharge probability has been increased, after adding extra laser pulses. It is therefore concluded that adding the Green and/or IR 10 ns laser pulses does not have the anticipated effect on the discharge, because of the too short plasma lifetime as compared to the discharge delay (μs). It is worth mentioning that adding extra laser pulses seems to reduce the fluctuation of the discharge delay, which is the only positive

effect we have observed so far.

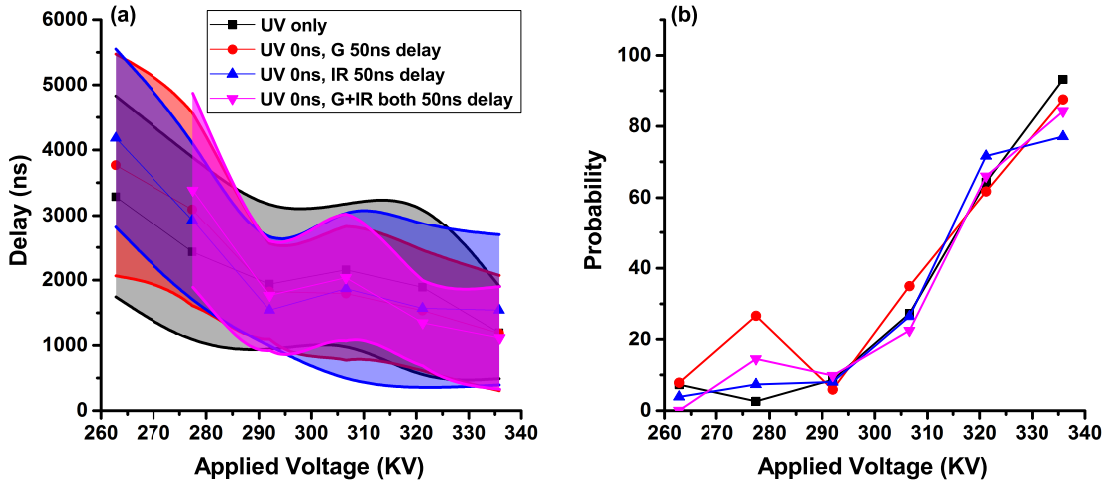

Figure 6.9: The dependence of discharge delay and probability on the applied voltage. The optical delay is fixed at 50 ns for different combination of laser pulses.

In Fig. 6.9(b), it has been noticed that the discharge probability is sometimes higher even with the lower applied voltage. Similar behavior has been often observed in other measurements. Two factors, i.e., the fluctuation of plasma conductivity and the change in absolute humidity, are found to be responsible for the mentioned phenomenon. Figure 6.10(a) presents the measurements with UV filament alone that are sorted with the same total applied voltage of 280 KV and the same absolute humidity of 0.0095 Kg/m^3. As much as 50% fluctuation in discharge delay is observed, which is attributed to the fluctuation of plasma conductivity as already demonstrated in Fig. 6.5. Data shown in Fig. 6.10(b) are obtained with the UV filament alone at the applied voltage of 340 KV and sorted with different absolute humidity. It can be concluded that the discharge delay decreases and the discharge probability increases with the increase of absolute humidity. In order to exclude the effect of humidity, one has to sort the data that are taken under the same humidity for comparison. However, same conclusion has been made that there is no significant effect on the discharge by adding other lasers, even with the data sorting [162]. So, the plasma fluc-

tuation itself already has strong effect on varying the discharge delay. The combined effects of both plasma conductivity fluctuation and humidity change are therefore responsible for the huge variation of discharge delay as demonstrated in Fig. 6.8.

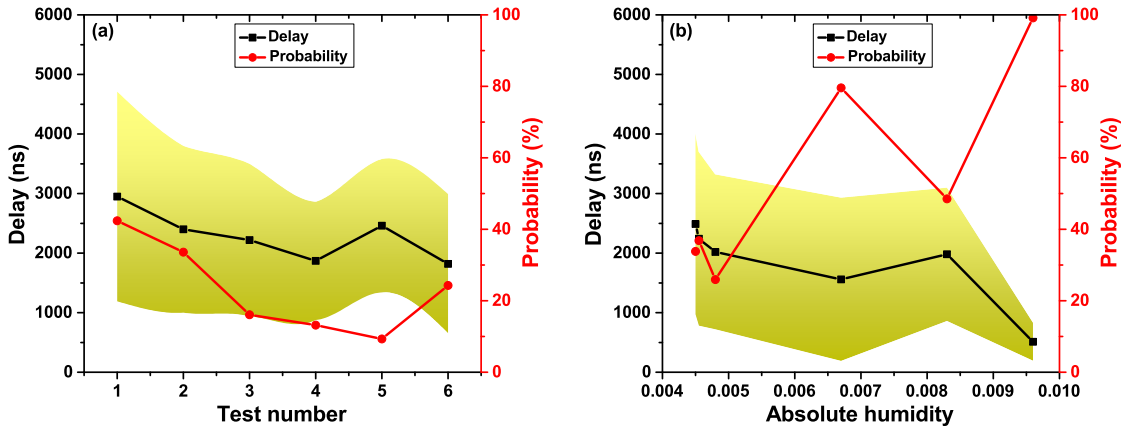

Figure 6.10: The effects of (a) plasma conductivity fluctuation and (b) absolute humidity change on the discharge delay.

In order to overcome the above mentioned issues, a long laser pulse is desired to keep the plasma created by the filament alive and stable, for a period that is comparable to the discharge delay.

6.4 Conclusion

Laser Induced discharge in air can be achieved at voltages which are less than the half voltage needed for self-breakdown. UV filaments are capable of creating transient conductivity of about 200 times larger as compared to NIR (800nm) filaments. Adding the Green (532nm) and/or IR (1064) laser pulses does not have any statistical significant effect on increasing the discharge probability or on reducing the delay. This is due to the fact that these laser pulses are not long enough to maintain the conductivity of the plasma channel.

One can conclude therefore that longer pulses are needed to keep the air ionized for the time needed to establish a discharge. Longer pulses and longer wavelength are desirable, such as could be achieved with atmospheric pressure CO_2 lasers. One last consideration is that the generation of the plasma beads should be avoided when CO_2 laser is employed for heating the plasma , since the inverse Bremstrahlung effect will be very strong with laser pulses of 10 μm wavelength.

Chapter 7

Conclusion

This dissertation has mainly focused on the investigation of long-pulse UV filaments in air. The major results and progresses can be summarized as follows.

First, we have designed and developed a high-power UV source, which satisfies the peak power requirement for the generation of UV filaments. The laser system is composed of a high-energy Nd:YAG laser with MOPA configuration and a high-energy SBS pulse compressor utilized for enhancing the peak power. Since it is not of importance to most of the studies, the spatio-temporal profile of the laser pulses from a high-energy Nd:YAG laser with unstable resonator design has been overlooked for decades. In this work, we have systematically investigated the spatio-temporal profiles of laser pulses from each stage of our high-energy, sub-nanosecond laser system. We show that the pulses generated from a Q-switched unstable oscillator exhibit a curved energy front. Interestingly, the energy front is less curved with higher optical gain. We also demonstrate that injection-seeding does not help to flatten the energy front. During laser amplification, the spatio-temporal profile of the oscillator pulse is further modified by the gain saturation effect within the amplifiers. More specifically, we find that, after amplification, the pulse from the beam center is temporally broader (up to 4 ns) and leads the pulse from the beam edge by more than

10 ns. Finally, after the SBS-based pulse compression stage, the spatio-temporal profile of the output pulse is further modified. Here, the center-to-edge delay of the energy front is shortened but still comparable to the pulse width, effectively lowering the achievable intensity as well as complicating the temporal structure of the laser pulse at the beam focus. Our measurements are accurately reproduced by numerical simulations of the underlying physical processes. To alleviate the cured energy front of pulses out of an unstable resonator, a possible solution based on the numerical simulation has also been proposed.

Stimulated Brillouin scattering pulse compression is an efficient and robust way to obtain sub-nanosecond pulses. With the optimized energy-scalable generator-amplifier setup, reliable and reproducible high-energy sub-nanosecond pulse generation in water has been demonstrated. Since shorter compressed pulse duration is always desired for achieving higher peak power, further effort has been put on resolving the long existing debate, i.e., the lower limit for the SBS compressed pulse width. We have revealed the interaction length as the key factor in determining the compressed pulse width in a single-cell setup. Conventionally, a too short interaction length has often been chosen to achieve sub-phonon lifetime pulse compression. Moreover, the mechanism that is responsible for the sub-phonon lifetime compression has also been identified as due to the energy exchange between the pump and compressed Stokes pulses. Experimentally, we have achieved the minimum compressed pulse duration of 150 ps (only half of the phonon lifetime of 295 ps) with the pulse energy of 90 mJ from a single-cell setup, or the minimum pulse duration of 170 ps with pulse energy up to 1.3 J from a two-cell setup. The maximum compressible energies in both SBS generator and amplifier are found to be limited by the competing nonlinear effect of stimulated Raman scattering, which typically ruins the stability of compressed pulse width. The experimental results have been well confirmed by the numerical simulations. Our work on SBS pulse compression paves the way to the reliable generation of sub-200 ps laser pulses at the Joule level energy.

Next, using the newly developed high-power UV source, we have investigated the UV

filament generation under different initial conditions. For the experiments carried out inside the laboratory with limited space, lenses with focal length of $\leq$3 m have been used to initiate the UV filaments. We have found that the complicated spatio-temporal profile of the UV pulses causes avalanche breakdown within the plasma channel created by the filament, when lenses with focal length of $\leq$1.5 m are used. This observation asks for further optimization of our high-power UV source. With the 3 m focusing lens, single filament has been observed. The plasma column created by the UV filaments and the spatial profile of the UV filaments have both been characterized. Using a 9 m focusing lens, multiple filaments have been generated in an open environment. The modulation in both amplitude and phase experienced by the UV beam during the 30 m propagation in the open environment is attributed to the observation of multiple filaments.

Then, the UV filaments have been applied for remote spectroscopy studies. Raman spectroscopy combined with UV filaments with their long range propagation capability is well suited for remote sensing application. We have carried out the proof of principle experiments, which have demonstrated the high efficiency (up to 10% of energy conversion efficiency) of forward Raman generation in gases excited by the UV filaments. The dependence of the generation of vibrational lines and rotational lines on the pump polarization has been experimentally studied. In order to enhance the Raman signal from low concentration species, another type of Raman scattering, i.e., impulsive stimulated scattering has also been investigated. The rotational Raman states of N_2 impulsively excited by the NIR filaments have been successfully probed by the weak UV pulses.

Backward emission is crucial for remote sensing application. We have however not observed the backward Raman emission from UV filaments in air. To explore the possibility of exciting backward Raman scattering, we have carried out a side experiment in water, which has much higher Raman gain coefficient. From this experiment, we have demonstrated that the backward Raman scattering can be efficiently driven by the intense stimulated Brillouin scattering. As high as 9% of energy conversion efficiency has been

achieved. Since SBS has already been observed from the UV filaments, it is possible to excite the backward SRS by the SBS, if the intensity of the SBS could be further enhanced.

Laser induced breakdown spectroscopy is a very versatile tool for sample identification. We have performed the LIBS experiments with all the laser pulses available inside our lab. The dynamics of self-absorption dip of the Al LIBS spectrum has been experimentally investigated. We have found that the build-up time of the self-absorption dip is strongly dependent on the plasma temperature, which is closely related to the laser wavelength. Surprisingly, the self-absorption dip is as narrow as less than 20 pm. Such narrow spectrum feature can be further utilized for high resolution spectroscopy.

Finally, the UV filaments have been employed for studying the laser-induced high-voltage discharge. We have demonstrated that the UV filaments are better suited for discharge triggering as compared to the NIR filaments, because of the higher conductivity plasma channel. A fully guided 40 cm long discharge has been demonstrated with the UV filament alone, at 1/2 the self-breakdown voltage in air. Two additional lasers are tested to improve the discharge triggering by photo-detaching oxygen negative ions and heating the plasma. The anticipated improvement in reducing the discharge delay or enhancing the discharge probability has not been observed.

Appendices

The following appendices describe part of the PhD works that have focused on the timescale of femtosecond to attosecond, much shorter than the sub-nanosecond addressed in the main body of this dissertation. The development of femtosecond laser and the associated laser technology of carrier-envelope-phase (CEP) stabilization are presented in detail, while the application of CEP stabilized femtosecond pulses for attosecond pulse generation is briefly mentioned.

Appendix A

Kerr lens mode-locked Ti:Sapphire femtosecond laser oscillator

Kerr lens mode-locked Ti:Sapphire laser was first discovered in 1991 [163] to generate 60 fs ultrashort pulses. Nowadays, pulses as short as few cycles (i.e., $< 10\ fs$ at the center wavelength of 800 nm) can be directly obtained from the Kerr lens mode-locked Ti:Sapphire oscillator, even with the carrier-envelope-phase (CEP) of the laser pulses being stabilized [164–167]. For the IR filament project, we want to build our own Ti:Sapphire oscillator, which will be combined with a commercial Ti:Sapphire laser amplifier to deliver laser pulses of 30 fs duration, 1 TW peak power at the repetition rate of 10 Hz. To achieve the above specifications, the requirements for the oscillator are as follows. The average output power should be more than 400 mW at the repetition rate of around 80 MHz. The spectral bandwidth needs to be as broad as 50 nm centered around 800 nm. In this section, we will report on the design, development and characterization of a Kerr lens mode-locked Ti:Sapphire laser oscillator.

A.1 Experimental setup

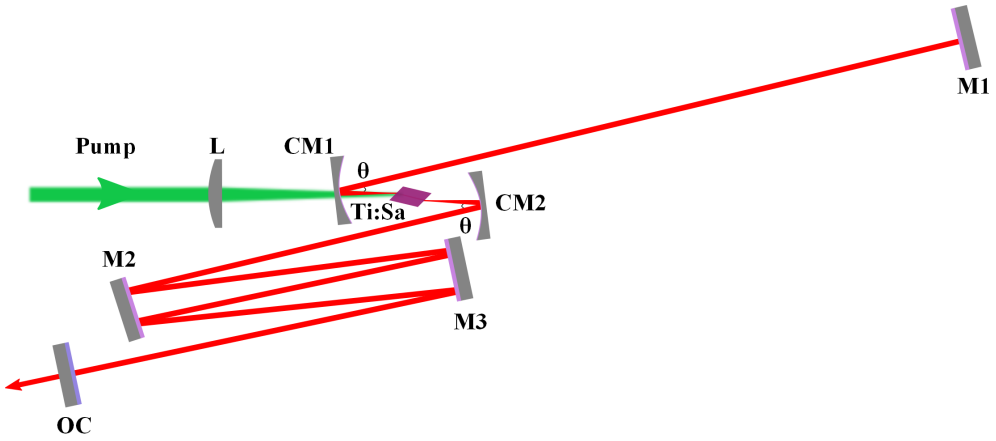

Figure A.1: Schematic design of the Kerr lens mode-locked Ti:Sapphire laser oscillator. M1-M3: Flat mirrors with GDD (720-870 nm) = -40±10 fs^2, HR>99.9% from 690-870 nm; CM: Curved mirrors with GDD (720-870 nm) = -40±10 fs^2, HR>99.9% from 720-880 nm, AR<0.2% at 532 nm; OC: Output coupler with GDD (720-870 nm) < 20 fs^2, T = 5±1%. All the above optics are from LAYERTEC.

The schematic design of our oscillator is presented in Fig. A.1. The laser cavity is formed by two flat end mirrors M1 and output coupler (OC) with 5% transmission, two curved mirrors (CM) with 5 cm radius of curvature focusing the laser beam into the the Ti:Sapphire crystal, and another two flat mirrors (M2 and M3) for extra dispersion compensation. The cavity length is 175 cm, i.e., with 58 cm for the upper arm and 117 cm for the lower arm, corresponding to the repetition rate of 85.7 MHz and pulse train period of 11.7 ns. The Ti:Sapphire crystal has dimension of $L3 \times W3 \times H0.9$ mm^3. The thickness of 0.9 mm is specially chosen for better heat conduct. Part of the output (5 W CW power) from a green laser (Verdi V10 from Coherent) is focused by a plano-convex lens (L) with 7.5 cm focal length to pump the crystal, which has absorption coefficient of 5.08 cm^{-1} at the pump wavelength. A thermoelectric cooler (TEC) is employed to stabilize the temperature of the crystal to be 18^0C. The three flat mirrors (M1, M2 and M3) and two curved mirrors (CM) with group delay dispersion (GDD) of -40 fs^2 each are used to compensate

the positive GDD introduced by the crystal, air, output coupler (OC) as well as the self phase modulation (SPM) inside the crystal. To use the least optics with limited negative GDD, multiple bounces on one mirror has been chosen. The angle θ has been designed to be 15.4^o to cancel out the astigmatism introduced by the crystal and curved mirrors.

A.2 Mode-locking procedures and results

There is a typical procedure for obtaining mode-locked laser pulses. First, one needs to maximize the CW output power, by playing with the cavity alignment, the position of the curved mirrors with respect to the crystal, and the focusing position of the pump beam inside the crystal. Two maximum CW power can typically be found when the curved mirror CM2 is translated. From the maximum CW power point where the curved mirror is further from the crystal, one starts to move the curved mirrors towards the crystal. During that process, a reduction of the output power will be observed. The spectrum also gets jumpy. During the mirror movement, the mode-locking can be initiated by taping the end mirror. To obtain stable mode-locking, the position of the crystal also needs to be finely tuned.

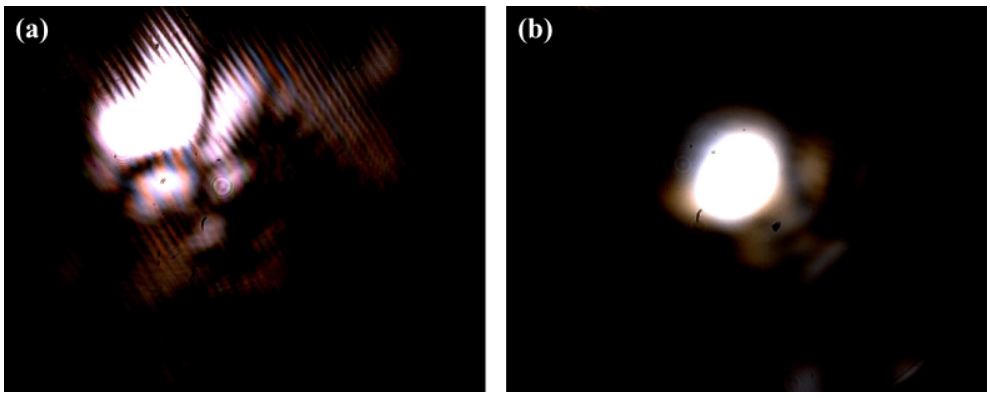

Figure A.2: Spatial profiles of (a) CW and (b) mode-locked operations of Ti:Sapphire laser oscillator.

After our oscillator gets mode-locked, the spatial, spectral and temporal profiles of the

laser pulses have all been characterized. Figure. A.2 displays the spatial profiles of the laser beam at both CW and mode-locked mode. Due to the Kerr lensing effct, the high order spatial mode from the CW operation has been filtered out in the mode-locked operation, as manifested by the clean and round profile shown in Fig. A.2(b).

Figure. A.3(a) shows the spectrum for the mode-locked laser pulses obtained from the current design. It has 36 nm FWHM spectral bandwidth, which is slightly narrower than the desired value. We have tried to increase the bandwidth through the cavity dispersion control, which is realized by varying the number of bounces on the flat mirrors M2 and M3. It however ends up with either less stable mode-locking or even narrower spectrum. It should be noticed that the change in dispersion can only be the multiple of 40 fs^2, which is too coarse to optimize the spectrum. In order to maximize the spectral bandwidth, a pair of thin wedges should be employed for very fine dispersion management.

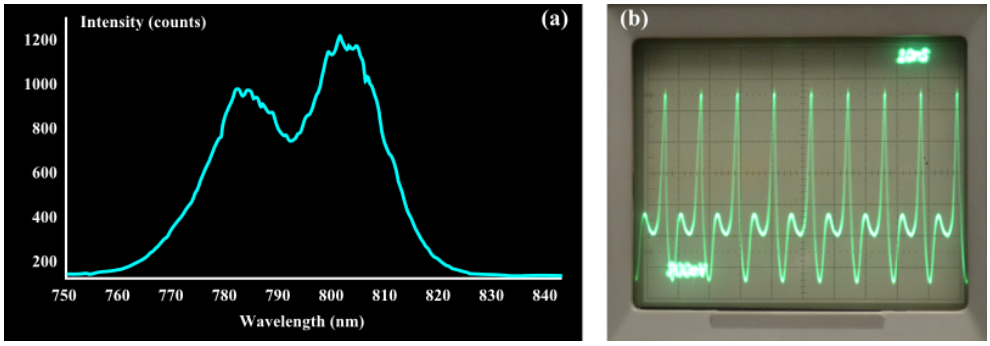

Figure A.3: (a) Spectral and (b) temporal characterizations of the mode-locked laser pulses.

In temporal characterization, the pulse train has been recorded by a photodiode and an oscilloscope, as demonstrated in Fig. A.3(b). The measured pulse period, which is slightly more than one division of 10 ns corresponds to the designed value of 11.7 ns. The pulse duration of the individual pulses has also been measured by an intensity autocorrelator to be 56 fs FWHM, which is much longer than the Fourier transform limited pulse of 26 fs if assume a Gaussian-shaped pulse with 36 nm FWHM spectral bandwidth. The discrepancy

is due to the pulse stretching introduced by the positive dispersion of different optics outside the cavity, such as the substrate of the output coupler, the filters used to attenuate the laser beam and the beam splitter inside the autocorrelator.

A.3 Summary

We have experimentally demonstrated a Kerr lens mode-locked Ti:Sapphire laser oscillator. The 36 nm FWHM spectral bandwidth obtained from the current design can support Fourier transform limited pulses of 26 fs duration. Even wider spectral bandwidth thereby shorter pulse width could be obtained with further optimization of the cavity dispersion.

Appendix B

Carrier-envelope-phase stabilization of amplified femtosecond laser pulses and their applications into attosecond science[9]

The CEP stabilized oscillator pulses typically have the energy of few nJ per pulse, which is not enough to perform most of the nonlinear studies. The oscillator pulses therefore need to be amplified through the laser amplifiers, which would introduce extra CEP noise. In the following sections, we will present our work on the CEP stabilization of the amplified femtosecond pulses, and briefly mention the application of those pulses into the attosecond science research. This work was carried out in the group of Professor Giuseppe Sansone in Politecnico di Milano and supported by a Marie-Curie Fellowship during the year of 2012.

[9]Portions of this Apendix have been published in C. Feng *et al.*, Opt. Express **21**, 25248-25256 (2013) [168]

B.1 Introduction

The control of strong-field phenomena down to the attosecond regime relies on the generation and application of ultrashort intense laser pulses characterized by a well defined and reproducible waveform, i.e. by a stable and controllable carrier-envelope-phase (CEP) [169]. Tailoring the electric field of few-cycle pulses allows one to steer the electronic motion inside atoms and molecules with unprecedented temporal resolution thus offering control over different processes such as above threshold ionization [170], non-sequential double ionization [171], and high-order harmonic generation [172]. The application of these sources for the investigation of strong field phenomena is triggering the development of high repetition rate lasers (from few kHz up to the MHz range) with high energy per pulse (from hundreds of μJ up to tens of mJ) leading to high average powers ($>$10 W) that challenge the possibility to control the CEP through the entire amplification process. The control of the CEP in amplified laser systems is usually based on the combination of two feedback loops operating on the oscillator and on the amplifier(s), respectively, that compensate for the CEP drift, i.e., the variation of CEP between two consecutive pulses. The train of pulses delivered by a mode-locked oscillator is characterized by a constant CEP drift determined by the difference between the group and the phase velocities in a round trip of the cavity. Intensity noise fluctuations induce variations of the CEP drift due to the intensity-phase coupling inside the active medium of the oscillator [173]. The CEP variation between consecutive pulses delivered by the oscillator can be fixed making use of a feedback loop based on a nonlinear interferometer, that measures the CEP drift, and either an acousto-optic modulator or a piezo-stage that modulates the power of the pump laser [174] or tilts an end mirror of the cavity [164], respectively. A full analysis of influence of cavity controls such as tilt and translation of the end mirror on the CEP can be found in [175]. Using a Fabry-Perot reference cavity, Jones and Diels [166,167] have pioneered another way to stabilize the frequency, phase and repetition rate of oscillator pulses simultaneously. Recently, a new approach based on a frequency shifter has been developed [165,176]. The amplifica-

tion process introduces additional CEP noise mainly due to mechanical instabilities in the stretcher-compressor setup, beam pointing instabilities or power fluctuations of the pump laser [177]. A second feedback loop is required for the compensation of this noise. High repetition rate, high average power lasers call for large correction bandwidth of the CEP-feedback loop that is limited either by the detection system or by the actuator. The CEP drift at the output of the amplifier can be characterized using a visible-infrared spectrometer that acquires the interference pattern generated by a spectrally broadened continuum and by its second harmonic in a nonlinear interferometer (f-2f interferometer) [178, 179] after the final compression stage. In this scheme the CEP drift is measured by applying a Fourier-based algorithm on the interference pattern. Alternatively the interference pattern can be sampled using two photomultipliers [180], a photodiodes array [181] or a single photodiode [182] replacing the visible-infrared spectrometer thus ensuring a faster acquisition rate. Strong-field effects such as ATI have also been used for single-shot CEP drift characterization of kHz-rate laser systems [183]. Several actuators acting only on the amplifiers have been proposed and experimentally demonstrated to correct the CEP noise induced by the amplification process including the adjustment of the distance between gratings in the stretcher/compressor [184], the variation of the amount of glass in the beam path by moving a glass wedge [185], or the modulation of the pump-power of the oscillator [172]. In the first two cases, as massive moving mechanical parts are included in the loop, the feedback bandwidth is limited to few Hertz; instead, in the last case, as two feedback loops (one for the oscillator and one for the amplifier) are acting on the same parameter, possible cross-talk might be unavoidable. Recently a new method, based on the use of a programmable acousto-optic dispersive filter (Dazzler) [186] inserted into the beam path, was proposed for the stabilization of the CEP of amplified pulses [187]. An electro-optic modulator was also successfully implemented in the correction of the CEP drift introduced by the amplification chain [188, 189]. The main advantage of these devices is the absence of moving parts, that could allow feedback bandwidths up to few tens of kHz. In this appendix, we demonstrate a complete analog feedback loop for correcting the CEP drift introduced by a high-average

power amplifier by combining a fast single-shot detection system and a fast actuator. We also present the application of CEP stabilized pulses in the generation of attosecond pulses, which are further employed in the investigation of eletron dynamics in atomic and molecular gases. In section B.2 we present the laser and CEP stabilization setup. In section B.3 we compare the results of CEP stablization obtained for the in-loop measurements using different approaches and the data acquired using an independent out-of-loop measurement of the CEP drift, discussing the importance of a single-shot characterization of CEP noise for high repetition rate laser systems. In section B.4, we briefly mention the application of CEP stabilized pulses into the generation of attosecond pulses. Finally, in section B.5 we present our conclusions.

B.2 Experimental setup for CEP stabilization

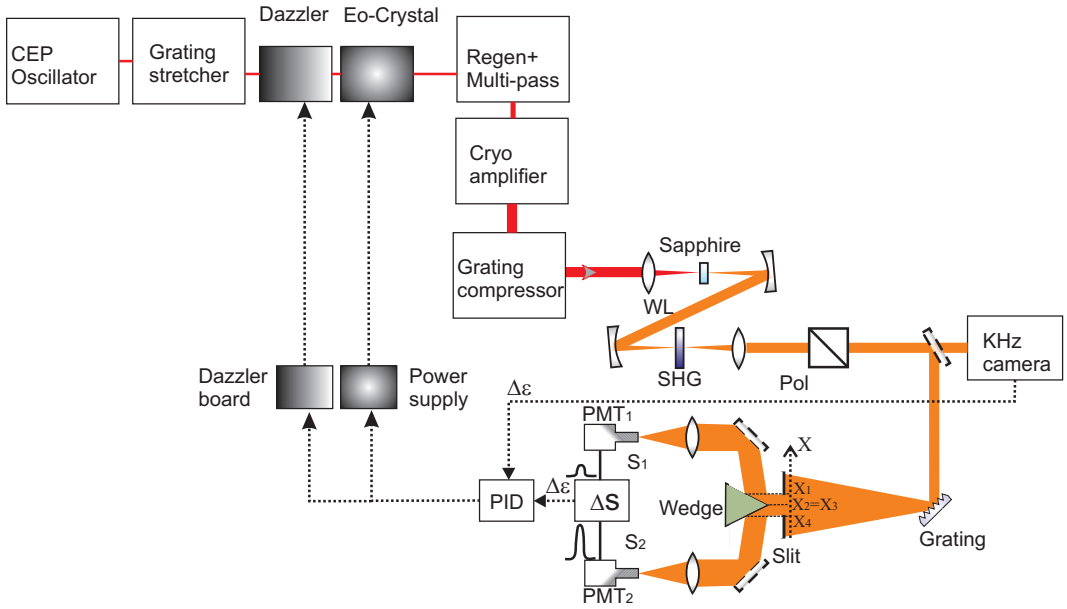

Figure B.1: Experimental setup. WL: white light; SHG : second harmonic generation crystal; Pol: polarizer; PMT: photomultiplier; PID: proportional-integrative-derivative.

The amplified laser system delivers ultrashort pulses (FWHM=25-30 fs) at 10 kHz rep-

etition rate with a pulse energy of 2 mJ after compression. The system is based on a commercially available CEP-stabilized oscillator (Rainbow-Femtolasers) with a residual CEP standard deviation σ= 90 mrad. The pulses are strechted by an $\ddot{O}$ffner triplet up to 360 ps; a programmable acousto-optic modulator (Dazzler) is placed after the stretcher to control the high-order phase dispersion terms. The pulses are then injected into a regenerative amplifier with an output power of about 1.2 W. A second acousto-optic modulator (Mazzler) [190] is inserted in the cavity for shaping and broadening of the amplified spectrum. At the output of the regenerative amplifier, a first water-cooled 4-pass pre-amplifier and a second 4-pass amplifier boost the energy up to 4.5 W and 29 W, respectively. The latter amplification stage is based on a cryo-cooled (-180^0C) crystal mounted in a vacuum chamber; at this low temperature the thermal lens introduced by the pump-laser is on the order of few meters and can be easily corrected. The pulses are finally injected in a grating-compressor with a throughput of about 70% for an output power of 20 W. The pulse duration was characterized using the second harmonic frequency-resolved optical gating technique. For the experiment, a small fraction (few μJ) of the compressed pulses is directed to a f-2f nonlinear interferometer [Fig. B.1], similar to the setups shown in refs. [178–180]. The pulses are focused in a 2-mm-thick sapphire plate for the generation of white-light (WL), corresponding to the signal at frequency f, which is collimated and then focused by two 100-mm focal length spherical mirrors in a 500-μm-thick BBO crystal cut for second harmonic generation at 1064 nm. The infrared part of the WL is frequency doubled leading to a new component (2f signal) around 500 nm with perpendicular polarization with respect to the initial WL. The lens placed after the second harmonic crystal focuses the diverging beam in correspondence of the slit position. A polarizer projects the polarization of the two pulses along the same direction and a 50% broadband beamsplitter separates the signals in two parts: the first one is focused in a spectrometer coupled with a line scan kHz camera that measures the spectral interference pattern between the f and the 2f components. The position of the fringes is directly related to the CEP of the laser pulse at the input of the f-2f interferometer. The line scan camera and acquisition software allows single-shot ac-

quisition up to a sampling rate (i.e. the maximum frequency at which single-shot data can be acquired) of 180 Hz. It is important to point out that a single laser pulse is sufficient to determine the CEP, avoiding average over consecutive pulses that might wash out fast CEP variations. The sampling rate of the system drops to 100 Hz when the acquisition software is also used to feedback the laser system to stabilize the CEP; it is mainly limited by the time required by the algorithm to retrieve the CEP drift $\Delta\varphi$ that determines the error signal $\Delta\varepsilon$, and by the communication with the control card which sends the correction voltage to the proportional-integrative-derivative (PID) device. The second part of the radiation is diffracted by a grating, that spatially resolves the spectral fringes along the direction indicated with x in Fig. B.1. We have verified that the fact that a non-collimated beam is diffracted by the grating does not appreciably deteriorate the spatial dispersion of the different spectral components at the slit position. A single fringe is selected by a slit, separated in two parts by the apex of a prism, and sent to two photomultipliers (PMTs) that integrate the signal over two ranges ($x1$,$x2$) and ($x3$,$x4$). Then, on a single-shot basis, the outputs of the PMTs are analogically integrated and subtracted, providing ΔS = S2–S1 and the signal error $\Delta\varepsilon$. For a symmetric alignment of the prism with respect to the slit (i.e. $x4$–$x3$ = $x2$–$x1$ = Δx and $x2$ = $x3$), it is possible to demonstrate analytically that the difference signal depends on the CEP, φ , according to the relation:

$$\Delta S\left(\varphi\right) \propto \frac{1}{\alpha}\sin^2\left(\alpha\Delta x/2\right)\sin\left(\alpha x_1+\varphi\right) \tag{B.1}$$

where α is determined by the grating dispersion and by the distance between the grating and the detectors. Calculations simulating this detection scheme show that a misalignment up to 20% of the slit from the symmetric configuration introduces a negligible error in the estimation of the CEP. Experimentally, we took care that the slit misalignment from symmetric configuration was less than 10%.

The error signals $\Delta\varepsilon$, delivered either by the kHz camera or by the PMTs detection system, is sent to a PID controller whose output drives either the Dazzler or an electro-optic (EO) crystal (LiNbO3) [188] introduced between the stretcher and the regenerative

amplifier. In the first case, the voltage applied to the analog input of the board driving the Dazzler selects a suitable acoustic wave that is sent to the acousto-optics for the correction of the CEP variation. In the second case, the signal drives a voltage amplifier connected to the EO crystal modulating the refraction index experienced by the laser pulses. The two systems allow to pre-compensate for the CEP drift measured at the output of the system. It is important to point out that in the case of the PMTs-based feedback the complete analog manipulation of the signal and the absence of any Fourier-based algorithm for the retrieval of the CEP drift make the scheme scalable to laser repetition rates up to a few hundreds of kHz. As stated in the introduction, the combination of a fast CEP detector (already exploited in refs. [180,182]) with fast actuators, like the Dazzler and the EO crystal, should allow for a larger correction bandwidth of CEP noise, while avoiding cross-talk issues that might occur when the feedback loops compensating for the noise introduced by the amplifier and by the oscillator operate on the same actuator [180, 182]. The combination of the two detection and analysis systems allows one to compare the performances of the feedbacks based on the kHz camera and on the PMTs acquisition devices. Great care was paid in minimizing air vibrations and mechanical instabilities occurring between the two detection systems.

B.3 Experimental results of CEP stabilization

The single-shot CEP drift measured by the kHz camera using the feedback loops based on the PMTs and kHz camera acquisition systems are shown in Fig. B.2. The CEP noise introduced by the amplification process is controlled using either the Dazzler [Figs. B.2(a) and (b)] or the EO crystal [Figs. B.2(c) and (d)]. When using the kHz camera to feedback the Dazzler or the EO crystal [Figs. B.2(b) and (d)], the sampling rate is reduced to 100 Hz, due to the software processing time; a higher sampling rate (180 Hz) can be achieved when the kHz camera only detects the single-shot CEP variations [Figs. B.2(a) and (c)].

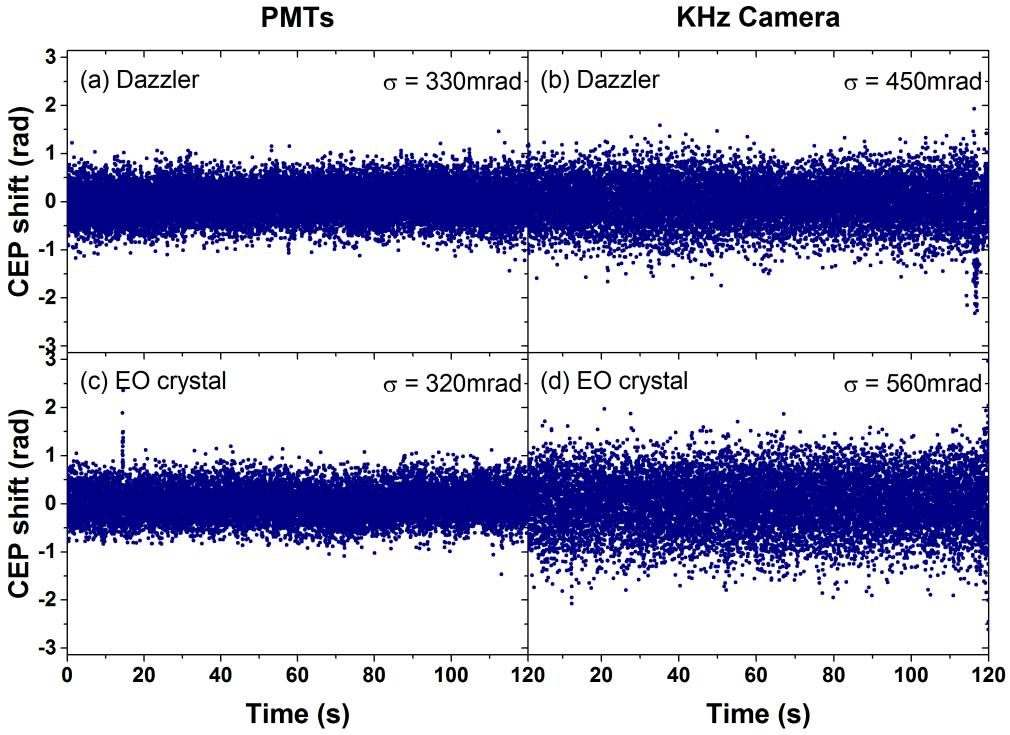

Figure B.2: Single-shot CEP variation measured by the kHz camera at an acquisition rate of 180 Hz (a,c) and 100 Hz(b,d). The feedback signal correcting the noise introduced by the amplifier system was provided by the PMTs (a,c) or the kHz camera (b,d) detection systems acting on the Dazzler (a,b) and on the EO crystal(c,d).

The measured CEP standard deviations σ using the PMTs-based feedback are 330 mrad for the Dazzler and 320 mrad for the EO crystal, indicating an improvement of 26% and 42% with respect to values of 450 mrad (Dazzler) and 560 mrad (EO crystal), respectively, measured using the kHz camera-based feedback. It is worth to remark that these values are based on single-shot measurements, thus ensuring a meaningful comparison between data acquired with different detection systems and actuators.

The improvement can be understood by comparing the power spectral densities (PSDs) of the CEP noise shown in Figs. B.3(a) and (b) (see black curves of Figs. B.3(a) and (b)). The PSDs without feedback on the amplifier (but with the fast feedback loop operating on

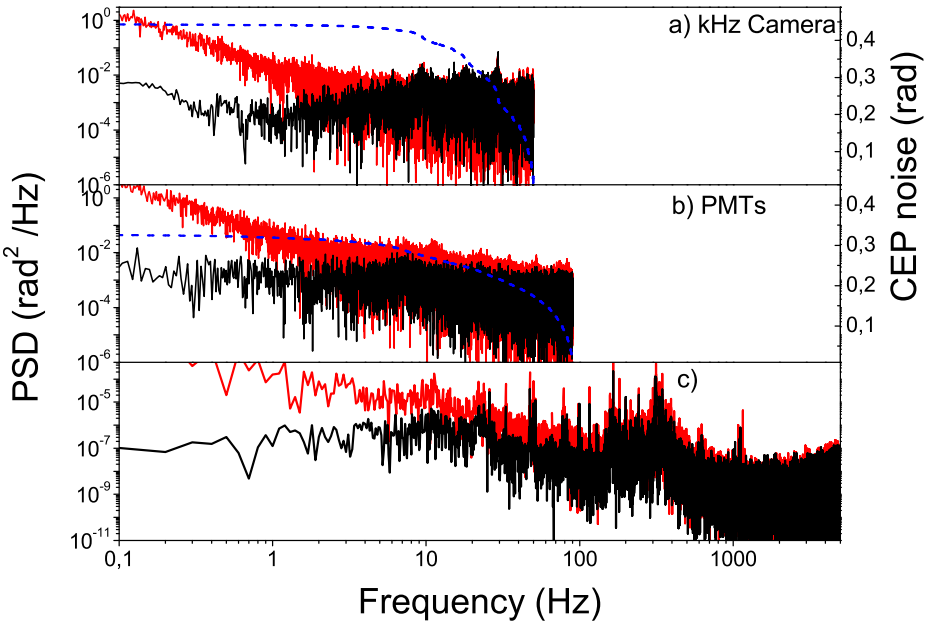

Figure B.3: Power spectral density (left axis) measured by the kHz camera with (black curves) and without (red curves) feedback loop operating on the amplifier. The error signal was provided to the Dazzler by the kHz camera (a) or by the PMTs detection system (b). The integrated phase noise (dashed blue curve ; right axis) as a function of frequency. (c) Power spectral density measured by an oscilloscope sampling the error signal $\Delta\varepsilon$ with (black curve) without (red curve) feedback on the amplifier. The feedback loop was provided to the Dazzler by the PMTs detection system.

the oscillator) are also shown for comparison (red curves). The kHz camera feedback allows one to efficiently reduce CEP noise up to a frequency of about 10 Hz, confirming the results presented in ref. [189]. Higher frequency components are not affected by the feedback loop due to the limited sampling rate of the error signal $\Delta\varepsilon$. The PMTs feedback, on the other hand, shows a clear reduction of the CEP noise up to the limit of 90 Hz, imposed by the sampling rate of 180 Hz of the digital measurement. The phase noise integrated over the frequency range (blue-dashed curves) confirm that the PMTs based feedback allows for a better control of the CEP with respect to the kHz camera system. The PSDs for the EO

crystal-based feedback loop present a similar behavior (not shown). The analog feedback loop allows one to achieve comparable final CEP stability using either the Dazzler or the EO crystal.

In order to verify that the PMTs feedback loop allows for correction of even higher frequency components, we recorded the PMTs error signal during the stabilization feedback based on the PMTs and the Dazzler. The oscilloscope resolution allows for a single-shot acquisition at the full repetition rate of the laser. In Fig. B.3(c) the PSD of the analog signal with (black curve) and without feedback loop (red curve) is presented. We show the PSDs in the frequency range between 0.1 Hz up and 5 kHz, evidencing that the correction of the analog loop is effective over a large frequency range up to frequencies as high as 1 kHz.

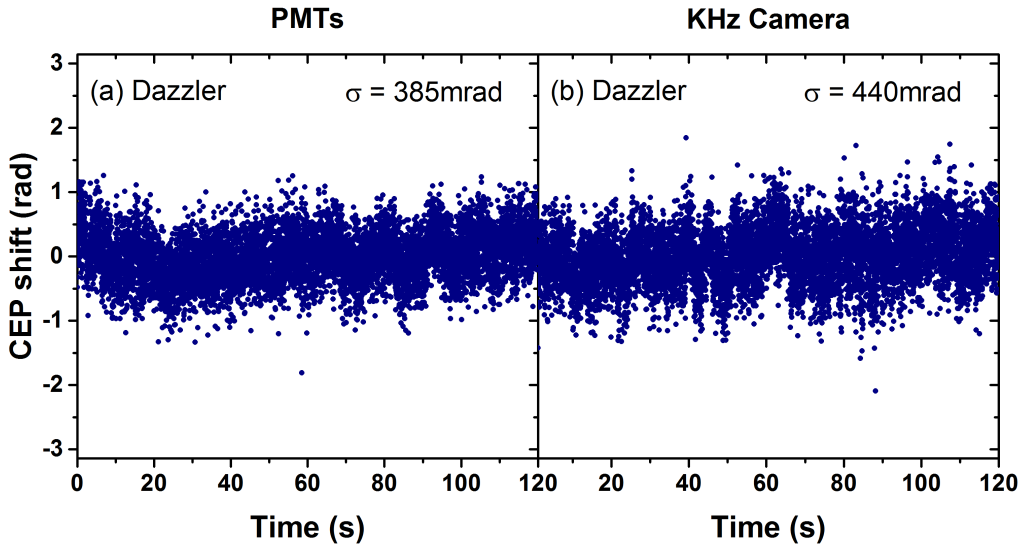

Figure B.4: CEP variation measured by an out-of-loop nonlinear f-2f interferometer. The feedback signal correcting the noise introduced by the amplifier system was provided by the PMTs (a) or the kHz camera (b) detection systems acting on the Dazzler.

We also performed an out-of-loop measurement of the CEP drift using a second independent nonlinear interferometer, as shown in Fig. B.4. A small fraction of the compressed pulse was used to generate the f-2f interference pattern that was measured by a visible-

infrared spectrometer connected to a software for the retrieval of the CEP. The CEP was stabilized using the PMTs and the kHz camera connected to the Dazzler. In this case the CEP standard deviation measured by the spectrometer integrating over 10 pulses were 385 mrad and 440 mrad, respectively. The improved stability by the fast analog feedback reduces to about 14%, due to additional noises that we attribute to the different conditions for the WL generation in the two independent interferometers. In spite of this, the out-of-loop measurements definitely confirm the improved CEP stability using the PMTs feedback.

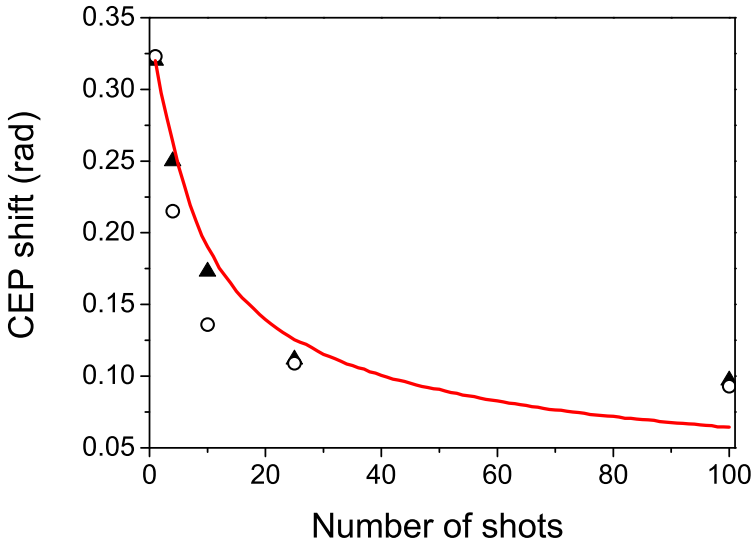

Figure B.5: Effect of the integration time on the shot-to-shot CEP standard deviation for the Dazzler analog feedback (open circle) and EO crystal analog feedback (full triangle). The solid curve indicates the expected standard deviation evolution as a function of the number of shots N, assuming a single-shot standard deviation of 320 mrad.

The importance of a fast feedback loop based on a single-shot CEP detection can be fully understood by analyzing the CEP variations for different integration times of the acquisition system as reported in Fig. B.5. The CEP was stabilized using the PMTs-based feedback and the data were acquired using the kHz camera for increasing integration times corresponding to an average over N laser shots. It is evident that even integration over few shots determines a remarkable reduction of the measured CEP drift with respect to the

single-shot value. In particular, averaging over a large number of shots (>20 in our experimental conditions) leads to a CEP standard deviation that is independent on the number of laser pulses. In these conditions it is not possible to draw any conclusion about the residual CEP noise drift, indicating that a single-shot high repetition rate acquisition system is of primary importance for a reliable characterization of the CEP noise. We also numerically evaluated the expected CEP standard deviation after averaging over N shots. We considered a train of pulses characterized by CEP values with zero average and standard deviation of 320 mrad, corresponding to the single-shot CEP fluctuation measured experimentally. To account for the long-term fluctuation of the laser, the CEPs of the closest consecutive pulses are also weakly correlated. For all choices of N, the average CEP has zero mean; the standard deviation, on the contrary, strongly depends on N, as evidenced by the red curve of Fig. B.5. This simple model is in well agreement with the experimental data, and confirms that for large numbers of N the fluctuations of the averaged CEP are well below its jitter recorded with single-shot detection.

B.4 Application of CEP stabilized pulses for the generation of isolated single attosecond pulses

The above CEP stabilized pulses have been employed for the generation isolated single attosecond pulses. To do so, the 30 fs CEP stabilized pulses have been first compressed to a few femtosecond via the hollow-core fiber compression [191, 192]. The compressed few-cycle pulses are then used in the generation of isolated single attosecond pulses in Kr, by employing the polarization gating technique [193]. The remaining IR beam has bee blocked by the Aluminium filter, which also shapes the XUV continuum to be centered around 25 eV. To characterize the attosecond pulses, the streaking measurement [194, 195] has been carried out in Ar, with the result presented in Fig. B.6(a). Finally, the amplitude and phase information of the isolated single attosecond pulse have been retrieved by the

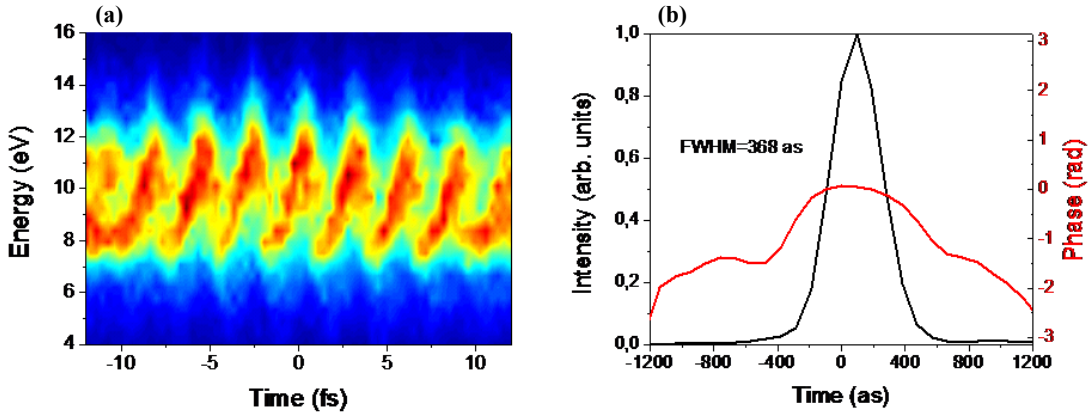

Figure B.6: (a) Streaking measurement of the isolated attosecond pulses; Detection gas: Ar. (b) Retrieved attosecond pulse amplitude and phase distributions.

FROG-CRAB algorithm [196] and demonstrated in Fig. B.6(b). Isolated single attosecond pulse with 368 as duration has been successfully obtained. The generated attosecond pulse have been further applied for the investigation of electron dynamics in molecular gas such as N_2. The results can be found in a recent publication [197].

B.5 Conclusions

We have demonstrated a novel, complete analog feedback loop for CEP drift stabilization of a high average power amplifier operating on a single-shot basis at the full repetition rate the laser system (10 kHz). The feedback is based on a fast acquisition detection setup in combination with either an acousto-optic or an electro-optic crystal. The absence of moving parts allows one to correct frequency noise up to 1 kHz leading to CEP residual noise of 320 mrad. The demonstrated method should be scalable to systems operating at repetition rates up to few hundreds of kHz. Out-of-loop measurements confirm the improvement of the CEP stability. The CEP stabilized pulses have been compressed to few-cycle pulses via the hollow-core fiber compression technique and employed in the generation of isolated

single attosecond pulses, which have been further applied for the investigation of electron dynamics in N_2.

References

[1] M. Hercher, "Laser-Induced Damage in Transparent Media," J. Opt. Soc. Am **54**, 563 (1964).

[2] R. Y. Chiao, E. Garmire, and C. H. Townes, "Self-Trapping of Optical Beams," Phys. Rev. Lett. **13**, 479–482 (1964).

[3] E. Garmire, R. Y. Chiao, and C. H. Townes, "Dynamics and characteristics of the self-trapping of intense light beams," Phys. Rev. Lett. **16**, 347–349 (1966).

[4] R. Chiao, M. Johnson, S. Krinsky, H. Smith, C. Townes, and E. Garmire, "A new class of trapped light filaments," IEEE J. Quantum Electron. **2**, 467–469 (1966).

[5] R. Y. Chiao, E. Garmire, and C. H. Townes, "Filamentary structure of light beams in nonlinear liquids," Phys. Rev. Lett. **13**, 479–482 (1964).

[6] A. Braun, G. Korn, X. Liu, D. Du, J. Squier, and G. Mourou, "Self-channeling of high-peak-power femtosecond laser pulses in air," Opt. Lett. **20**, 73–75 (1995).

[7] X. M. Zhao, P. Rambo, and J.-C. Diels, "Filamentation of femtosecond UV pulses in air," in "QELS, 1995," , vol. 16 (Optical Society of America, Baltimore, MA, 1995), vol. 16, p. 178 (QThD2).

[8] A. Couairon and A. Mysyrowicz, "Femtosecond filamentation in transparent media," Phys. Rep. **441**, 47–189 (2007).

[9] J. Kasparian, M. Rodriguez, G. Méjean, J. Yu, E. Salmon, H. Wille, R. Bourayou, S. Frey, Y.-B. André, A. Mysyrowicz, R. Sauerbrey, J.-P. Wolf, and L. Wöste, "White-Light Filaments for Atmospheric Analysis," Science **301**, 61–64 (2003).

[10] D. Mirell, O. Chalus, K. Peterson, and J.-C. Diels, "Remote sensing of explosives using infrared and ultraviolet filaments," J. Opt. Soc. Am. B **25**, B108–B111 (2008).

[11] X. M. Zhao, J.-C. Diels, C. Y. Wang, and J. Elizondo, "Femtosecond ultraviolet laser pulse induced electrical discharges in gases," IEEE J. Quantum Electron. **31**, 599–612 (1995).

[12] P. K. Rambo, J. Schwarz, and J. C. Diels, "High voltage electrical discharges induced by an ultrashort pulse UV laser system," J. Opt. A **3**, 146–158 (2001).

[13] J. Kasparian, R. Ackermann, Y.-B. André, G. Méchain, G. Méjean, B. Prade, P. Rohwetter, E. Salmon, K. Stelmaszczyk, J. Yu, A. Mysyrowicz, R. Sauerbrey, L. Wöste, and J.-P. Wolf, "Electric events synchronized with laser filaments in thunderclouds," Opt. Express **16**, 5757–5763 (2008).

[14] K. Sugiyama, T. Fujii, M. Miki, M. Yamaguchi, A. Zhidkov, E. Hotta, and K. Nemoto, "Laser-filament-induced corona discharges and remote measurements of electric fields," Opt. Lett. **34**, 2964–2966 (2009).

[15] P. Rohwetter, J. Kasparian, K. Stelmaszczyk, Z. Hao, S. Henin, N. Lascoux, W. M. Nakaema, Y. Petit, M. Queiszer, R. Salame, E. Salmon, L. Woste, and J.-P. Wolf, "Laser-induced water condensation in air," Nat. Photon. **4**, 451–456 (2010).

[16] J. Ju, J. Liu, C. Wang, H. Sun, W. Wang, X. Ge, C. Li, S. L. Chin, R. Li, and Z. Xu, "Laser-filamentation-induced condensation and snow formation in a cloud chamber," Opt. Lett. **37**, 1214–1216 (2012).

[17] M. Chateauneuf, S. Payeur, J. Dubois, and J.-C. Kieffer, "Microwave guiding in air by a cylindrical filament array waveguide," Appl. Phys. Lett. **92**, 091104 (2008).

[18] D. S. Steingrube, E. Schulz, T. Binhammer, M. B. Gaarde, A. Couairon, U. Morgner, and M. Kovacev, "High-order harmonic generation directly from a filament," New J. Phys. **13**, 043022 (2011).

[19] O. Chalus, "Study of nonlinear effects of intense UV beams in atmosphere," UNM Dissertation (2007).

[20] X. Xu, "High power pulse UV source development and its applications," UNM Dissertation (2014).

[21] X. Xu and J.-C. Diels, "Stable single axial mode operation of injection-seeded Q-switched Nd:YAG laser by real-time resonance tracking method," Appl. Phys. B **114**, 579–584 (2014).

[22] C. Feng, X. Xu, and J.-C. Diels, "Spatio–temporal characterization of pulses obtained from a high-energy sub-nanosecond laser system," Appl. Opt. **55**, 1603–1612 (2016).

[23] A. E. Siegman, "Unstable optical resonators for laser applications," Proc. IEEE **53**, 277–287 (1965).

[24] A. E. Siegman, "Unstable optical resonators," Appl. Opt. **13**, 353–367 (1974).

[25] W. Koechner, *Solid-State Laser Engineering* (Springer, New York, 2006), 6th ed.

[26] S. De Silvestri, V. Magni, O. Svelto, and G. Valentini, "Lasers with super-Gaussian mirrors," IEEE J. Quantum Electron. **26**, 1500–1509 (1990).

[27] S. D. Silvestri, V. Magni, S. Taccheo, and G. Valentini, "Q-switched Nd:YAG laser with super-Gaussian resonators," Opt. Lett. **16**, 642–644 (1991).

[28] A. Caprara and G. C. Reali, "Time-resolved M^2 of nanosecond pulses from a Q-switched variable-reflectivity-mirror Nd:YAG laser," Opt. Lett. **17**, 414–416 (1992).

[29] A. Caprara and G. C. Reali, "Time varying M^2 in Q-switched lasers," Opt. Quantum Electron. **24**, S1001–S1009 (1992).

[30] G. Anstett, M. Nittmann, A. Borsutzky, and R. Wallenstein, "Experimental investigation and numerical simulation of the spatio-temporal dynamics of nanosecond pulses in Q-switched Nd:YAG lasers," Appl. Phys. B **76**, 833–838 (2003).

[31] M. A. Dansson, M. Boisselle, M. A. Linne, and H. A. Michelsen, "Complications to optical measurements using a laser with an unstable resonator: a case study on laser-induced incandescence of soot," Appl. Opt. **46**, 8095–8103 (2007).

[32] A. E. Siegman, *Lasers* (University Science Books, California, 1986).

[33] N. Basov, R. Ambartsumyan, V. Zuev, P. Kryukov, and V. Letokhov, "Nonlinear amplification of light pulses," Sov. Phys. -JETP **50**, 23–34 (1966).

[34] P. G. Kryukov and V. S. Letokhov, "Propagation of a light pulse in a resonantly amplifying (absorbing) medium," Sov. Phys. Usp. **12**, 641 (1970).

[35] L. M. Frantz and J. S. Nodvik, "Theory of pulse propagation in a laser amplifier," J. Appl. Phys. **34**, 2346–2349 (1963).

[36] Y. Park, G. Giuliani, and R. Byer, "Single axial mode operation of a Q-switched Nd:YAG oscillator by injection seeding," IEEE J. Quantum Electron. **20**, 117–125 (1984).

[37] D. N. Schimpf, C. Ruchert, D. Nodop, J. Limpert, A. Tünnermann, and F. Salin, "Compensation of pulse-distortion in saturated laser amplifiers," Opt. Express **16**, 17637–17646 (2008).

[38] P. A. Franken, A. E. Hill, C. W. Peters, and G. Weinreich, "Generation of optical harmonics," Phys. Rev. Lett. **7**, 118–119 (1961).

[39] A. V. Smith, "SNLO nonlinear optics code available from A. V. Smith, AS-Photonics, Albuquerque, NM," .

[40] Y. R. Shen, *The Principles of Nonlinear Optics* (John Wiley & Sons, New York, 1984).

[41] J. J. Zayhowski and C. Dill, "Diode-pumped microchip lasers electro-optically Q-switched at high pulse repetition rates," Opt. Lett. **17**, 1201–1203 (1992).

[42] D. T. Hon, "Pulse compression by stimulated Brillouin scattering," Opt. Lett. **5**, 516–518 (1980).

[43] M. Damzen and H. Hutchinson, "Laser pulse compression by stimulated brillouin scattering in tapered waveguides," IEEE J. Quantum Electron. **19**, 7–14 (1983).

[44] R. Fedosejevs and A. Offenberger, "Subnanosecond pulses from a KrF laser pumped SF6 Brillouin amplifier," IEEE J. Quantum Electron. **21**, 1558–1562 (1985).

[45] R. R. Buzyalis, A. S. Dementjev, and E. K. Kosenko, "Formation of subnanosecond pulses by stimulated Brillouin scattering of radiation from a pulse-periodic Nd:YAG laser," Sov. J. Quantum Electron. **15**, 1335 (1985).

[46] S. Schiemann, W. Ubachs, and W. Hogervorst, "Efficient temporal compression of coherent nanosecond pulses in a compact SBS generator-amplifier setup," IEEE J. Quantum Electron. **33**, 358 –366 (1997).

[47] V. Kmetik, H. Fiedorowicz, A. A. Andreev, K. J. Witte, H. Daido, H. Fujita, M. Nakatsuka, and T. Yamanaka, "Reliable stimulated Brillouin scattering compression of Nd:YAG laser pulses with liquid fluorocarbon for long-time operation at 10 Hz," Appl. Opt. **37**, 7085–7090 (1998).

[48] D. Neshev, I. Velchev, W. Majewski, W. Hogervorst, and W. Ubachs, "SBS pulse compression to 200Âăps in a compact single-cell setup," Appl. Phys. B **68**, 671–675 (1999).

[49] H. Yoshida, T. Hatae, H. Fujita, M. Nakatsuka, and S. Kitamura, "A high-energy 160-ps pulse generation by stimulated brillouin scattering from heavy fluorocarbon liquid at 1064 nm wavelength," Opt. Express **17**, 13654–13662 (2009).

[50] Y. Wang, X. Zhu, Z. Lu, and H. Zhang, "Generation of 360 ps laser pulse with 3 J energy by stimulated Brillouin scattering with a nonfocusing scheme," Opt. Express **23**, 23318–23328 (2015).

[51] C. Feng, X. Xu, and J.-C. Diels, "Generation of 300 ps laser pulse with 1.2 J energy by stimulated Brillouin scattering in water at 532 nm," Opt. Lett. **39**, 3367–3370 (2014).

[52] X. Xu, C. Feng, and J.-C. Diels, "Optimizing sub-ns pulse compression for high energy application," Opt. Express **22**, 13904–13915 (2014).

[53] I. Velchev, D. Neshev, W. Hogervorst, and W. Ubachs, "Pulse compression to the subphonon lifetime region by half-cycle gain in transient stimulated Brillouin scattering," IEEE J. Quantum Electron. **35**, 1812–1816 (1999).

[54] C. Dane, W. Neuman, and L. Hackel, "High-energy SBS pulse compression," IEEE J. Quantum Electron. **30**, 1907–1915 (1994).

[55] M. J. Damzen and M. H. R. Hutchinson, "High-efficiency laser-pulse compression by stimulated brillouin scattering," Opt. Lett. **8**, 313–315 (1983).

[56] A. Mitra, H. Yoshida, H. Fujita, and M. Nakatsuka, "Sub nanosecond pulse generation by stimulated brillouin scattering using fc-75 in an integrated setup with laser energy up to 1.5 j," Jpn. J. Appl. Phys. **45**, 1607 (2006).

[57] V. A. Gorbunov, S. B. PapernyÄŋ, V. F. Petrov, and V. R. Startsev, "Time compression of pulses in the course of stimulated brillouin scattering in gases," Sov. J. Quantum Electron. **13**, 900 (1983).

[58] Y. Nizienko, A. Mamin, P. Nielsen, and B. Brown, "300 ps ruby laser using stimulated brillouin scattering pulse compression," Rev. Sci. Instrum. **65**, 2460–2463 (1994).

[59] H. Yoshida, H. Fujita, M. Nakatsuka, T. Ueda, and A. Fujinoki, "Temporal compression by stimulated brillouin scattering of q-switched pulse with fused-quartz and fused-silica glass from 1064 nm to 266 nm wavelength," Laser and Particle Beams **25**, 481–488 (2007).

[60] M. A. Davydov, K. F. Shipilov, and T. A. Shmaonov, "Formation of highly compressed stimulated Brillouin scattering pulses in liquids," Sov. J. Quantum Electron. **16**, 1402 (1986).

[61] H. Yoshida, V. Kmetik, H. Fujita, M. Nakatsuka, T. Yamanaka, and K. Yoshida, "Heavy fluorocarbon liquids for a phase-conjugated stimulatedbrillouin scattering mirror," Appl. Opt. **36**, 3739–3744 (1997).

[62] O. Chalus and J.-C. Diels, "Lifetime of fluorocarbon for high-energy stimulated brillouin scattering," J. Opt. Soc. Am. B **24**, 606–608 (2007).

[63] V. Kmetik, H. Yoshida, H. Fujita, M. Nakatsuka, and T. Yamanaka, "Very high energy sbs phase conjugation and pulse compression in fluorocarbon liquids," Proc. SPIE **3889**, 818–826 (2000).

[64] R. W. Boyd, *Nonlinear optics* (Academic Press, 2008), 3rd ed.

[65] G. Abbate, U. Bernini, E. Ragozzino, and F. Somma, "The temperature dependence of the refractive index of water," J. Phys. D: Appl. Phys. **11**, 1167 (1978).

[66] R. W. Boyd, K. Rzązewski, and P. Narum, "Noise initiation of stimulated Brillouin scattering," Phys. Rev. A **42**, 5514–5521 (1990).

[67] I. Velchev and W. Ubachs, "Statistical properties of the Stokes signal in stimulated Brillouin scattering pulse compressors," Phys. Rev. A **71**, 043810 (2005).

[68] C. Feng and J.-C. Diels, "High-energy sub-phonon lifetime pulse compression based on stimulated brillouin scattering in liquids," (To be submitted).

[69] S. Afshaarvahid, V. Devrelis, and J. Munch, "Nature of intensity and phase modulations in stimulated brillouin scattering," Phys. Rev. A **57**, 3961–3971 (1998).

[70] S. Chin, T.-J. Wang, C. Marceau, J. Wu, J. Liu, O. Kosareva, N. Panov, Y. Chen, J.-F. Daigle, S. Yuan, A. Azarm, W. Liu, T. Seideman, H. Zeng, M. Richardson, R. Li, and Z. Xu, "Advances in intense femtosecond laser filamentation in air," Laser Phys. **22**, 1–53 (2012).

[71] A. Brodeur, C. Y. Chien, F. A. Ilkov, S. L. Chin, O. G. Kosareva, and V. P. Kandidov, "Moving focus in the propagation of ultrashort laser pulses in air," Opt. Lett. **22**, 304–306 (1997).

[72] A. Dubietis, E. Gaižauskas, G. Tamošauskas, and P. Di Trapani, "Light filaments without self-channeling," Phys. Rev. Lett. **92**, 253903 (2004).

[73] J.-C. Diels, J. Yeak, D. Mirell, R. Fuentes, S. Rostami, D. Faccio, and P. di Trapani, "Air filaments and vacuum," Laser Phys. **20**, 1101–1106 (2010).

[74] G. Fibich and A. L. Gaeta, "Critical power for self-focusing in bulk media and in hollow waveguides," Opt. Lett. **25**, 335–337 (2000).

[75] P. Polynkin and M. Kolesik, "Critical power for self-focusing in the case of ultrashort laser pulses," Phys. Rev. A **87**, 053829 (2013).

[76] S. I. Mitryukovskiy, Y. Liu, A. Houard, and A. Mysyrowicz, "Re-evaluation of the peak intensity inside a femtosecond laser filament in air," Journal of Physics B: Atomic, Molecular and Optical Physics **48**, 094003 (2015).

[77] J. Schwarz, P. Rambo, J.-C. Diels, M. Kolesik, E. M. Wright, and J. V. Moloney, "Ultraviolet filamentation in air," Optics Communications **180**, 383 – 390 (2000).

[78] J. Schwarz, "High Intensity Laser Pulse Propagation through the Atmosphere, Lightning Protection and Filamentation," UNM Dissertation (2003).

[79] O. Chalus, A. Sukhinin, A. Aceves, and J.-C. Diels, "Propagation of non-diffracting intense ultraviolet beams," Opt. Commun. **281**, 3356–3360 (2008).

[80] K. Lim, M. Durand, M. Baudelet, and M. Richardson, "Transition from linear- to nonlinear-focusing regime in filamentation," Scientific Reports **4**, 07217 (2014).

[81] F. Théberge, W. Liu, P. T. Simard, A. Becker, and S. L. Chin, "Plasma density inside a femtosecond laser filament in air: Strong dependence on external focusing," Phys. Rev. E **74**, 036406 (2006).

[82] L. Arissian, D. Mirell, S. Rostami, A. Bernstein, D. Faccio, and J.-C. Diels, "The effect of propagation in air on the filament spectrum," Opt. Express **20**, 8337–8343 (2012).

[83] T. Fujii, M. Miki, N. Goto, A. Zhidkov, T. Fukuchi, Y. Oishi, and K. Nemoto, "Leader effects on femtosecond-laser-filament-triggered discharges," Phys. Plasmas **15**, 013107 (2008).

[84] E. W. Rosenthal, N. Jhajj, J. K. Wahlstrand, and H. M. Milchberg, "Collection of remote optical signals by air waveguides," Optica **1**, 5–9 (2014).

[85] A. Sukhinin, A. Aceves, J.-C. Diels, and L. Arissian, "On the co-existence of ir and uv optical filaments," J. Phys. B **48**, 094021 (2015).

[86] Z. Hosseinimakarem, M. K. Poutous, and E. G. Johnson, "Meta Optics for Filaments," First annual review of ARO MURI program on "Light Filamentation Science" (Santa Fe, 2012).

[87] Y. P. Raĭzer, "Breakdown and heating of gases under the influence of a laser beam," Soviet Physics Uspekhi **8**, 650 (1966).

[88] P. Polynkin, B. Pasenhow, N. Driscoll, M. Scheller, E. M. Wright, and J. V. Moloney, "Seeded optically driven avalanche ionization in molecular and noble gases," Phys. Rev. A **86**, 043410 (2012).

[89] L. Woeste, S. Wedeking, J. Wille, P. Rairouis, B. Stein, S. Nikolov, C. Werner, S. Niedermeier, F. Ronneberger, H. Schillinger, and R. Sauerbrey, "Femtosecond atmospheric lamp," Laser und Optoelektronic **29**, 51–53 (1997).

[90] P. Rairoux, H. Schillinger, S. Niedermeier, M. Rodriguez, F. Ronneberger, R. Sauerbrey, B. Stein, D. Waite, C. Wedeking, H. Wille, L. Woeste, and C. Ziener, "Remote sensing of the atmosphere using ultrashort laser pulses," Appl. Phys. B **71**, 573–580 (2000).

[91] J. Yu, D. Mondelain, G. Ange, R. Volk, S. Niedermeier, J. P. Wolf, J. Kasparian, and R. Sauerbrey, "Backward supercontinuum emission from a filament generated by ultrashort laser pulses in air," Opt. Lett. **26**, 533–535 (2001).

[92] P. Rohwetter, K. Stelmaszczyk, L. Wöste, R. Ackermann, G. Méjean, E. Salmon, J. Kasparian, J. Yu, and J.-P. Wolf, "Filament-induced remote surface ablation for long range laser-induced breakdown spectroscopy operation," Spectrochim. Acta B **60**, 1025–1033 (2005). Laser Induced Plasma Spectroscopy and Applications (LIBS 2004) Third International ConferenceLIBS MalagaLaser Induced Plasma Spectroscopy and Applications (LIBS 2004) Third International Conference.

[93] J. Yao, B. Zeng, H. Xu, G. Li, W. Chu, J. Ni, H. Zhang, S. L. Chin, Y. Cheng, and Z. Xu, "High-brightness switchable multiwavelength remote laser in air," Phys. Rev. A **84**, 051802 (2011).

[94] D. Kartashov, S. Ališauskas, G. Andriukaitis, A. Pugžlys, M. Shneider, A. Zheltikov, S. L. Chin, and A. Baltuška, "Free-space nitrogen gas laser driven by a femtosecond filament," Phys. Rev. A **86**, 033831 (2012).

[95] D. Kartashov, S. Ališauskas, A. Baltuška, A. Schmitt-Sody, W. Roach, and P. Polynkin, "Remotely pumped stimulated emission at 337 nm in atmospheric nitrogen," Phys. Rev. A **88**, 041805 (2013).

[96] J. Yao, G. Li, C. Jing, B. Zeng, W. Chu, J. Ni, H. Zhang, H. Xie, C. Zhang, H. Li, H. Xu, S. L. Chin, Y. Cheng, and Z. Xu, "Remote creation of coherent emissions in air with two-color ultrafast laser pulses," New J. Phys. **15**, 023046 (2013).

[97] J. Ni, W. Chu, C. Jing, H. Zhang, B. Zeng, J. Yao, G. Li, H. Xie, C. Zhang, H. Xu, S.-L. Chin, Y. Cheng, and Z. Xu, "Identification of the physical mechanism of generation of coherent N_2^+ emissions in air by femtosecond laser excitation," Opt. Express **21**, 8746–8752 (2013).

[98] Y. Liu, Y. Brelet, G. Point, A. Houard, and A. Mysyrowicz, "Self-seeded lasing in ionized air pumped by 800 nm femtosecond laser pulses," Opt. Express **21**, 22791–22798 (2013).

[99] H. Zhang, C. Jing, J. Yao, G. Li, B. Zeng, W. Chu, J. Ni, H. Xie, H. Xu, S. L. Chin, K. Yamanouchi, Y. Cheng, and Z. Xu, "Rotational Coherence Encoded in an "Air-Laser" Spectrum of Nitrogen Molecular Ions in an Intense Laser Field," Phys. Rev. X **3**, 041009 (2013).

[100] J. Yao, H. Xie, B. Zeng, W. Chu, G. Li, J. Ni, H. Zhang, C. Jing, C. Zhang, H. Xu, Y. Cheng, and Z. Xu, "Gain dynamics of a free-space nitrogen laser pumped by circularly polarized femtosecond laser pulses," Opt. Express **22**, 19005–19013 (2014).

[101] C. Jing, H. Zhang, W. Chu, H. Xie, J. Ni, B. Zeng, G. Li, J. Yao, H. Xu, Y. Cheng, and Z. Xu, "Generation of an air laser at extended distances by femtosecond laser filamentation with telescope optics," Opt. Express **22**, 3151–3156 (2014).

[102] J. Ni, W. Chu, H. Zhang, B. Zeng, J. Yao, L. Qiao, G. Li, C. Jing, H. Xie, H. Xu, Y. Cheng, and Z. Xu, "Impulsive rotational Raman scattering of N_2 by a remote "air laser" in femtosecond laser filament," Opt. Lett. **39**, 2250–2253 (2014).

[103] W. Chu, G. Li, H. Xie, J. Ni, J. Yao, B. Zeng, H. Zhang, C. Jing, H. Xu, Y. Cheng, and Z. Xu, "A self-induced white light seeding laser in a femtosecond laser filament," Laser Phys. Lett. **11**, 015301 (2014).

[104] S. Mitryukovskiy, Y. Liu, P. Ding, A. Houard, and A. Mysyrowicz, "Backward stimulated radiation from filaments in nitrogen gas and air pumped by circularly polarized 800 nm femtosecond laser pulses," Opt. Express **22**, 12750–12759 (2014).

[105] P. Ding, S. Mitryukovskiy, A. Houard, E. Oliva, A. Couairon, A. Mysyrowicz, and Y. Liu, "Backward lasing of air plasma pumped by circularly polarized femtosecond pulses for the sake of remote sensing (BLACK)," Opt. Express **22**, 29964–29977 (2014).

[106] G. Point, Y. Liu, Y. Brelet, S. Mitryukovskiy, P. Ding, A. Houard, and A. Mysyrowicz, "Lasing of ambient air with microjoule pulse energy pumped by a multi-terawatt infrared femtosecond laser," Opt. Lett. **39**, 1725–1728 (2014).

[107] Y. Liu, P. Ding, G. Lambert, A. Houard, V. Tikhonchuk, and A. Mysyrowicz, "Recollision-Induced Superradiance of Ionized Nitrogen Molecules," Phys. Rev. Lett. **115**, 133203 (2015).

[108] P. N. Malevich, R. Maurer, D. Kartashov, S. Ališauskas, A. A. Lanin, A. M. Zheltikov, M. Marangoni, G. Cerullo, A. Baltuška, and A. Pugžlys, "Stimulated raman gas sensing by backward uv lasing from a femtosecond filament," Opt. Lett. **40**, 2469–2472 (2015).

[109] L. Arissian, "Private conversation, University of New Mexico," (2016).

[110] C. T. L. Smeenk, L. Arissian, A. V. Sokolov, M. Spanner, K. F. Lee, A. Staudte, D. M. Villeneuve, and P. B. Corkum, "Alignment dependent enhancement of the photoelectron cutoff for multiphoton ionization of molecules," Phys. Rev. Lett. **112**, 253001 (2014).

[111] A. Compaan, A. Wagoner, and A. Aydinli, "Rotational raman scattering in the instructional laboratory," American Journal of Physics **62**, 639–645 (1994).

[112] K. P. Huber and G. Herzberg, *Molecular Spectra and Molecular Structure, Vol. 4, Constants of Diatomic molecules* (Van Nostrand Reinhold, New York, 1979).

[113] A. M. Weiner, "Femtosecond pulse shaping using spatial light modulators," Rev. Sci. Instrum. **71**, 1929–1960 (2000).

[114] M. Bitter and V. Milner, "Generating long sequences of high-intensity femtosecond pulses," Appl. Opt. **55**, 830–833 (2016).

[115] C. Feng, J.-C. Diels, X. Xu, and L. Arissian, "Ring-shaped backward stimulated raman scattering driven by stimulated brillouin scattering," Opt. Express **23**, 17035–17045 (2015).

[116] E. J. Woodbury and W. K. Ng, "Ruby laser operation in the near IR," Proc. IRE **50**, 2367 (1962).

[117] G. Eckhardt, R. W. Hellwarth, F. J. McClung, S. E. Schwarz, D. Weiner, and E. J. Woodbury, "Stimulated Raman scattering from organic liquids," Phys. Rev. Lett. **9**, 455–457 (1962).

[118] O. Rahn, M. Maier, and W. Kaiser, "Stimulated Raman, librational, and Brillouins scattering in water," Opt. Commun. **1**, 109–110 (1969).

[119] M. Maier, W. Kaiser, and J. A. Giordmaine, "Intense light bursts in the stimulated Raman effect," Phys. Rev. Lett. **17**, 1275–1277 (1966).

[120] M. Maier, W. Kaiser, and J. A. Giordmaine, "Backward stimulated Raman scattering," Phys. Rev. **177**, 580–599 (1969).

[121] M. J. Colles, "Efficient stimulated Raman scattering from picosecond pulses," Opt. Commun. **1**, 169–172 (1969).

[122] D. von der Linde, M. Maier, and W. Kaiser, "Quantitative investigations of the stimulated Raman effect using subnanosecond light pulses," Phys. Rev. **178**, 11–17 (1969).

[123] Y. R. Shen and N. Bloembergen, "Theory of stimulated Brillouin and Raman scattering," Phys. Rev. **137**, A1787–A1805 (1965).

[124] R. R. Alfano and G. A. Zawadzkas, "Observation of backward-stimulated Raman scattering generated by picosecond laser pulses in liquids," Phys. Rev. A **9**, 822–824 (1974).

[125] G. G. Bret and M. M. Denariez, "Stimulated Raman effect in acetone and acetone-carbon-disulfide mixtures," Appl. Phys. Lett. **8**, 151–154 (1966).

[126] R. G. Brewer, J. R. Lifsitz, E. Garmire, R. Y. Chiao, and C. H. Townes, "Small-scale trapped filaments in intense laser beams," Phys. Rev. **166**, 326–331 (1968).

[127] R. Chevalier, A. Sokolovskaia, N. Tcherniega, and G. Rivoire, "Stimulated backward Raman scattering excited in the picosecond range: high efficiency conversions," Opt. Commun. **82**, 117–122 (1991).

[128] J.-Z. Zhang, G. Chen, and R. K. Chang, "Pumping of stimulated Raman scattering by stimulated Brillouin scattering within a single liquid droplet: input laser linewidth effects," J. Opt. Soc. Am. B **7**, 108–115 (1990).

[129] D. Liu, J. Shi, M. Ouyang, X. Chen, J. Liu, and X. He, "Pumping effect of stimulated Brillouin scattering on stimulated Raman scattering in water," Phys. Rev. A **80**, 033808 (2009).

[130] J. Shi, X. Chen, M. Ouyang, W. Gong, Y. Su, and D. Liu, "Theoretical investigation on the pumping effect of stimulated Brillouin scattering on stimulated Raman scattering in water," Appl. Phys. B **106**, 445–451 (2012).

[131] D. Pohl and W. Kaiser, "Time-resolved investigations of stimulated brillouin scattering in transparent and absorbing media: Determination of phonon lifetimes," Phys. Rev. B **1**, 31–43 (1970).

[132] I. A. Walmsley and M. G. Raymer, "Experimental study of the macroscopic quantum fluctuations of partially coherent stimulated raman scattering," Phys. Rev. A **33**, 382–390 (1986).

[133] K. Stelmaszczyk, P. Rohwetter, G. Méjean, J. Yu, E. Salmon, J. Kasparian, R. Ackermann, J.-P. Wolf, and L. Wöste, "Long-distance remote laser-induced breakdown spectroscopy using filamentation in air," Appl. Phys. Lett. **85**, 3977–3979 (2004).

[134] S. Tzortzakis, D. Anglos, and D. Gray, "Ultraviolet laser filaments for remote laser-induced breakdown spectroscopy (libs) analysis: applications in cultural heritage monitoring," Opt. Lett. **31**, 1139–1141 (2006).

[135] J.-F. Daigle, G. Méjean, W. Liu, F. Théberge, H. Xu, Y. Kamali, J. Bernhardt, A. Azarm, Q. Sun, P. Mathieu, G. Roy, J.-R. Simard, and S. Chin, "Long range trace detection in aqueous aerosol using remote filament-induced breakdown spectroscopy," Appl. Phys. B **87**, 749–754 (2007).

[136] H. L. Xu, J. Bernhardt, P. Mathieu, G. Roy, and S. L. Chin, "Understanding the advantage of remote femtosecond laser-induced breakdown spectroscopy of metallic targets," Journal of Applied Physics **101**, 033124 (2007).

[137] S. L. Chin, H. L. Xu, Q. Luo, F. Théberge, W. Liu, J. F. Daigle, Y. Kamali, P. T. Simard, J. Bernhardt, S. A. Hosseini, M. Sharifi, G. Méjean, A. Azarm, C. Marceau, O. Kosareva, V. P. Kandidov, N. Aközbek, A. Becker, G. Roy, P. Mathieu, J. R. Simard, M. Châteauneuf, and J. Dubois, "Filamentation "remote" sensing of chemical and biological agents/pollutants using only one femtosecond laser source," Appl. Phys. B **95**, 1–12 (2009).

[138] H. L. Xu and S. L. Chin, "Femtosecond laser filamentation for atmospheric sensing," Sensors **11**, 32 (2011).

[139] H. Hou, G. C.-Y. Chan, X. Mao, R. Zheng, V. Zorba, and R. E. Russo, "Femtosecond filament-laser ablation molecular isotopic spectrometry," Spectrochim. Acta B **113**, 113–118 (2015).

[140] W. Liu, H. Xu, G. Méjean, Y. Kamali, J.-F. Daigle, A. Azarm, P. Simard, P. Mathieu, G. Roy, and S. Chin, "Efficient non-gated remote filament-induced breakdown spectroscopy of metallic sample," Spectrochim. Acta B **62**, 76–81 (2007).

[141] D. A. Cremers and L. J. Radziemski, *Handbook of Laser-Induced Breakdown Spectroscopy* (Wiley, 2013), 2nd ed.

[142] A. Kramida, Yu. Ralchenko, J. Reader, and NIST ASD Team, NIST Atomic Spectra Database (ver. 5.3), [Online]. Available: `http://physics.nist.gov/asd` [2016, February 29]. National Institute of Standards and Technology, Gaithersburg, MD. (2015).

[143] D. W. Koopman and T. D. Wilkerson, "Channeling of an ionizing electrical streamer by a laser beam," J. Appl. Phys. **42**, 1883–1886 (1971).

[144] D. W. Koopman and K. A. Saum, "Formation and guiding of high-velocity electrical streamers by laser-induced ionization," J. Appl. Phys. **44**, 5328–5336 (1973).

[145] J. R. Greig, D. W. Koopman, R. F. Fernsler, R. E. Pechacek, I. M. Vitkovitsky, and A. W. Ali, "Electrical discharges guided by pulsed co_2 laser radiation," Phys. Rev. Lett. **41**, 174–177 (1978).

[146] L. M. Ball, "The laser lightning rod system: Thunderstorm domestication," Appl. Opt. **13**, 2292–2295 (1974).

[147] M. Miki, Y. Aihara, and T. Shindo, "Development of long gap discharges guided by a pulsed CO_2 laser," J. Phys. D: Appl. Phys. **26**, 1244–1252 (1993).

[148] X. M. Zhao, J.-C. Diels, A. Braun, X. Liu, D. Du, G. Korn, G. Mourou, and J. Elizondo, "Use of self-trapped filaments in air to trigger lightning," in "Ultrafast Phenomena IX," , P. F. Barbara, W. H. Knox, G. A. Mourou, and A. H. Zewail, eds. (Springer Verlag, Berlin, Dana Point, CA, 1994), pp. 233–235.

[149] B. La Fontaine, D. Comtois, C.-Y. Chien, A. Desparois, F. GÃľnin, G. Jarry, T. Johnston, J.-C. Kieffer, F. Martin, R. Mawassi, H. PÃľpin, F. A. M. Rizk, F. Vidal, C. Potvin, P. Couture, and H. P. Mercure, "Guiding large-scale spark discharges with ultrashort pulse laser filaments," J. Appl. Phys. **88**, 610–615 (2000).

[150] M. Rodriguez, R. Sauerbrey, H. Wille, L. Woeste, T. Fujii, Y. B. Andre, A. Mysyrowicz, L. Klingbeil, K. Rethmeier, and W. K. et al, "Triggering and guiding megavolt discharges by use of laser-induced ionized filaments," Optics Lett. **27**, 772–774 (2002).

[151] B. Forestier, A. Houard, I. Revel, M. Durand, Y. B. AndrÃľ, B. Prade, A. Jarnac, J. Carbonnel, M. Le NevÃľ, J. C. de Miscault, B. Esmiller, D. Chapuis, and A. Mysyrowicz, "Triggering, guiding and deviation of long air spark discharges with femtosecond laser filament," AIP Advances **2**, 012151 (2012).

[152] M. Miki and A. Wada, "Guiding of electrical discharges under atmospheric air by ultravioled laser-produced plasma channel," J. Appl. Phys. **80**, 3208–3214 (1996).

[153] X. Liu, X. Lu, Z. Zhang, X.-L. Liu, J.-L. Ma, and J. Zhang, "Triggering of high voltage discharge by femtosecond laser filaments on different wavelengths," Optics Communications **284**, 5372 – 5375 (2011).

[154] P. K. Rambo, J. Biegert, V. Kubecek, J. Schwarz, A. Bernstein, J. C. Diels, R. Bernstein, and K. Stahlkopf, "Laboratory tests of laser induced lightning discharge," Journal of Optical Technology **66**, 194–198 (1999).

[155] Z. Q. Hao, J. Zhang, Y. T. Li, X. Lu, X. H. Yuan, Z. Y. Zheng, Z. H. Wang, W. J. Ling, and Z. Y. Wei, "Prolongation of the fluorescence lifetime of plasma channels in air induced by femtosecond laser pulses," Appl. Phys. B **80**, 627–630 (2005).

[156] J. Zhu, Z. Ji, Y. Deng, J. Liu, R. Li, and Z. Xu, "Long lifetime plasma channel in air generated by multiple femtosecond laser pulses and an external electrical field," Opt. Express **14**, 4915–4922 (2006).

[157] B. Zhou, S. Akturk, B. Prade, Y.-B. André, A. Houard, Y. Liu, M. Franco, C. D'Amico, E. Salmon, Z.-Q. Hao, N. Lascoux, and A. Mysyrowicz, "Revival of femtosecond laser plasma filaments in air by a nanosecond laser," Opt. Express **17**, 11450–11456 (2009).

[158] X.-L. Liu, X. Liu, J.-L. Ma, L.-B. Feng, X. lei Ge, Y. Zheng, Y.-T. Li, L.-M. Chen, Q.-L. Dong, Wei-MinWang, Zhao-HuaWang, H. Teng, Z.-Y. Wei, and J. Zhang, "Long lifetime air plasma channel generated by femtosecond laser pulse sequence," Opt. Express **20**, 5968–5973 (2012).

[159] J. Papeer, M. Botton, D. Gordon, P. Sprangle, A. Zigler, and Z. Henis, "Extended lifetime of high density plasma filament generated by a dual femtosecond-nanosecond laser pulse in air," New J. Phys. **16**, 123046 (2014).

[160] G. Méjean, R. Ackermann, J. Kasparian, E. Salmon, J. Yu, J.-P. Wolf, K. Rethmeier, W. Kalkner, P. Rohwetter, K. Stelmaszczyk, and L. Wöste, "Improved laser triggering and guiding of meqavolt discharges with dual fs-ns pulses," Appl. Phys. Lett. **88**, 021101 (2006).

[161] G. Point, L. Arantchouk, A. Mysyrowicz, and A. Houard, "Interferometric study of low density channels and guided electric discharges induced in air by laser filament," Conference on Laser, Weather, and Climate (2015).

[162] A. Rastegari, E. Schubert, C. Feng, D. Mongin, B. Kamer, J. Kasparian, J.-P. Wolf, L. Arissian, and J.-C. Diels, "Beam control through nonlinear propagation in air and laser induced discharges," Proc. SPIE **9727**, 97271H–97271H–12 (2016).

[163] D. E. Spence, P. N. Kean, and W. Sibbett, "60-fsec pulse generation from a self-mode-locked ti:sapphire laser," Opt. Lett. **16**, 42–44 (1991).

[164] D. J. Jones, S. A. Diddams, J. K. Ranka, A. Stentz, R. S. Windeler, J. L. Hall, and S. T. Cundiff, "Carrier-envelope phase control of femtosecond mode-locked lasers and direct optical frequency synthesis," Science **288**, 635–639 (2000).

[165] S. Koke, C. Grebing, H. Frei, A. Anderson, A. Assion, and G. Steinmeyer, "Direct frequency comb synthesis with arbitrary offset and shot-noise-limited phase noise," Nat Photon **4**, 462–465 (2010).

[166] R. J. Jones, J. C. Diels, J. Jasapara, and W. Rudolph, "Stabilization of the frequency, phase, and repetition rate of an ultra-short pulse train to a Fabry-Perot reference cavity," Opt. Commun. **175**, 409–418 (2000).

[167] R. J. Jones and J. C. Diels, "Stabilization of femtosecond lasers for optical frequency metrology and direct optical to radio frequency synthesis," Phys. Rev. Lett. **86**, 3288–3291 (2001).

[168] C. Feng, J.-F. Hergott, P.-M. Paul, X. Chen, O. Tcherbakoff, M. Comte, O. Gobert, M. Reduzzi, F. Calegari, C. Manzoni, M. Nisoli, and G. Sansone, "Complete analog control of the carrier-envelope-phase of a high-power laser amplifier," Opt. Express **21**, 25248–25256 (2013).

[169] F. Krausz and M. Ivanov, "Attosecond physics," Rev. Mod. Phys. **81**, 163–234 (2009).

[170] G. G. Paulus, F. Lindner, H. Walther, A. Baltuška, E. Goulielmakis, M. Lezius, and F. Krausz, "Measurement of the phase of few-cycle laser pulses," Phys. Rev. Lett. **91**, 253004 (2003).

[171] X. Liu, H. Rottke, E. Eremina, W. Sandner, E. Goulielmakis, K. O. Keeffe, M. Lezius, F. Krausz, F. Lindner, M. G. Schätzel, G. G. Paulus, and H. Walther, "Non-sequential double ionization at the single-optical-cycle limit," Phys. Rev. Lett. **93**, 263001 (2004).

[172] A. Baltuška, T. Udem, M. Uiberacker, M. Hentschel, E. Goulielmakis, C. Gohle, R. Holzwarth, V. S. Yakovlev, A. Scrinzi, T. W. Hansch, and F. Krausz, "Attosecond control of electronic processes by intense light fields," Nature **421**, 611–615 (2003).

[173] L. Xu, T. W. Hänsch, C. Spielmann, A. Poppe, T. Brabec, and F. Krausz, "Route to phase control of ultrashort light pulses," Opt. Lett. **21**, 2008–2010 (1996).

[174] R. Holzwarth, T. Udem, T. W. Hänsch, J. C. Knight, W. J. Wadsworth, and P. S. J. Russell, "Optical frequency synthesizer for precision spectroscopy," Phys. Rev. Lett. **85**, 2264–2267 (2000).

[175] L. Arissian and J.-C. Diels, "Carrier to envelope and dispersion control in a cavity with prism pairs," Phys. Rev. A **75**, 013814 (2007).

[176] B. Borchers, S. Koke, A. Husakou, J. Herrmann, and G. Steinmeyer, "Carrier-envelope phase stabilization with sub-10 as residual timing jitter," Opt. Lett. **36**, 4146–4148 (2011).

[177] A. Baltuška, M. Uiberacker, E. Goulielmakis, R. Kienberger, V. Yakovlev, T. Udem, T. Hansch, and F. Krausz, "Phase-controlled amplification of few-cycle laser pulses," IEEE J. Sel. Top. Quant. **9**, 972–989 (2003).

[178] M. Mehendale, S. A. Mitchell, J.-P. Likforman, D. M. Villeneuve, and P. B. Corkum, "Method for single-shot measurement of the carrier envelope phase of a few-cycle laser pulse," Opt. Lett. **25**, 1672–1674 (2000).

[179] M. Kakehata, H. Takada, Y. Kobayashi, K. Torizuka, Y. Fujihira, T. Homma, and H. Takahashi, "Single-shot measurement of carrier-envelope phase changes by spectral interferometry," Opt. Lett. **26**, 1436–1438 (2001).

[180] S. Koke, C. Grebing, B. Manschwetus, and G. Steinmeyer, "Fast f-to-2f interferometer for a direct measurement of the carrier-envelope phase drift of ultrashort amplified laser pulses," Opt. Lett. **33**, 2545–2547 (2008).

[181] T. Fordell, M. Miranda, C. L. Arnold, and A. L'Huillier, "High-speed carrier-envelope phase drift detection of amplified laser pulses," Opt. Express **19**, 23652–23657 (2011).

[182] C. Li, A. Schill, F. Emaury, J. Chu, P. Féru, J.-M. Héritier, and W. Tulloch, *Multiphoton Processes and Attosecond Physics: Proceedings of the 12th International Conference on Multiphoton Processes (ICOMP12) and the 3rd International Conference on Attosecond Physics (ATTO3)* (Springer Berlin Heidelberg, Berlin, Heidelberg, 2012), chap. Single Shot Carrier Envelope Phase Stabilization of a 10 kHz, 10 W RegenerativeAmplifier, pp. 9–13.

[183] A. M. Sayler, T. Rathje, W. Müller, K. Rühle, R. Kienberger, and G. G. Paulus, "Precise, real-time, every-single-shot, carrier-envelope phase measurement of ultrashort laser pulses," Opt. Lett. **36**, 1–3 (2011).

[184] C. Li, E. Moon, and Z. Chang, "Carrier-envelope phase shift caused by variation of grating separation," Opt. Lett. **31**, 3113–3115 (2006).

[185] M. Schätzel, F. Lindner, G. Paulus, H. Walther, E. Goulielmakis, A. Baltuška, M. Lezius, and F. Krausz, "Long-term stabilization of the carrier-envelope phase of few-cycle laser pulses," Appl. Phys. B **79**, 1021–1025 (2004).

[186] F. Verluise, V. Laude, Z. Cheng, C. Spielmann, and P. Tournois, "Amplitude and phase control of ultrashort pulses by use of an acousto-optic programmable dispersive filter:âĂČpulse compression and shaping," Opt. Lett. **25**, 575–577 (2000).

[187] N. Forget, L. Canova, X. Chen, A. Jullien, and R. Lopez-Martens, "Closed-loop carrier-envelope phase stabilization with an acousto-optic programmable dispersive filter," Opt. Lett. **34**, 3647–3649 (2009).

[188] O. Gobert, P. Paul, J. Hergott, O. Tcherbakoff, F. Lepetit, P. D. 'Oliveira, F. Viala, and M. Comte, "Carrier-envelope phase control using linear electro-optic effect," Opt. Express **19**, 5410–5418 (2011).

[189] J.-F. Hergott, O. Tcherbakoff, P.-M. Paul, P. Demengeot, M. Perdrix, F. Lepetit, D. Garzella, D. Guillaumet, M. Comte, P. D. Oliveira, and O. Gobert, "Carrier-envelope phase stabilization of a 20 w, grating based, chirped-pulse amplified laser, using electro-optic effect in a linbo3 crystal," Opt. Express **19**, 19935–19941 (2011).

[190] T. Oksenhendler, D. Kaplan, P. Tournois, G. Greetham, and F. Estable, "Intracavity acousto-optic programmable gain control for ultra-wide-band regenerative amplifiers," Appl. Phys. B **83**, 491–494 (2006).

[191] M. Nisoli, S. De Silvestri, and O. Svelto, "Generation of high energy 10 fs pulses by a new pulse compression technique," Appl. Phys. Lett. **68**, 2793–2795 (1996).

[192] M. Nisoli, S. D. Silvestri, O. Svelto, R. Szipöcs, K. Ferencz, C. Spielmann, S. Sartania, and F. Krausz, "Compression of high-energy laser pulses below 5 fs," Opt. Lett. **22**, 522–524 (1997).

[193] G. Sansone, E. Benedetti, F. Calegari, C. Vozzi, L. Avaldi, R. Flammini, L. Poletto, P. Villoresi, C. Altucci, R. Velotta, S. Stagira, S. De Silvestri, and M. Nisoli, "Isolated single-cycle attosecond pulses," Science **314**, 443–446 (2006).

[194] J. Itatani, F. Quéré, G. L. Yudin, M. Y. Ivanov, F. Krausz, and P. B. Corkum, "Attosecond streak camera," Phys. Rev. Lett. **88**, 173903 (2002).

[195] M. Kitzler, N. Milosevic, A. Scrinzi, F. Krausz, and T. Brabec, "Quantum theory of attosecond xuv pulse measurement by laser dressed photoionization," Phys. Rev. Lett. **88**, 173904 (2002).

[196] Y. Mairesse and F. Quéré, "Frequency-resolved optical gating for complete reconstruction of attosecond bursts," Phys. Rev. A **71**, 011401 (2005).

[197] M. Reduzzi, W.-C. Chu, C. Feng, A. Dubrouil, J. Hummert, F. Calegari, F. Frassetto, L. Poletto, O. Kornilov, M. Nisoli, C.-D. Lin, and G. Sansone, "Observation of autoionization dynamics and sub-cycle quantum beating in electronic molecular wave packets," Journal of Physics B: Atomic, Molecular and Optical Physics **49**, 065102 (2016).